

**Integrated Non-Planar Ferroelectric
Nanostructures**

A Thesis

Submitted to the Faculty

of

Drexel University

by

Stephen Sommers Nonnenmann

in partial fulfillment of the

requirements for the degree

of

Doctor of Philosophy

April 2010

© Copyright 2010
Stephen S. Nonnenmann. All Rights Reserved.

Dedicated to Pop Pop.

Acknowledgements

I would first like to thank my advisor, Dr. Jonathan Spanier, for providing the support and means without which my research would have never been completed. It has been an honor and privilege to serve as the first graduate student in a laboratory with such an intense interest in science. I would like to think that I still could not be confused with a physicist, but my time spent here has proven otherwise. I also must thank my committee members, Drs. Caroline Schauer, Michel Barsoum, Wei-Heng Shih, Steven May, and Andrew Rappe for additional guidance and mentoring along this process. I gained much valuable insight not only within the context of science, but professionally as well.

I have worked with many amazing people during my tenure in the MesoMaterials Laboratory. In particular, I'd like to thank postdocs Greg Soja and Archie Peters, fellow grad students Linyou Cao, Oren Leaffer, Terrence McGuckin, and Guannan Chen, visiting PhD student Bora Garipcan, and undergraduates Lee Laim, Ron Martin, Rahul Joseph, Mike Coster, and Brian Beatty. Eric Gallo and Stephanie Johnson definitely deserve special recognition for putting up with an ungodly amount of nonsense and ranting monologues from me, in addition to the vast amounts of scientific discussions and inquiries we shared together. I'd also like to thank fellow students in the MSE department for help over the years, namely Jessica Schiffman and Kishore Tenneti.

My deepest love and thanks is extended to my girlfriend Julia. I have received support from you which completely transcends my experience here and I'm so grateful for this. And to my parents and my siblings Heather and Michael. I am so happy to have had additional support through good and bad times, thank you so much.

I have been blessed to have been supported by a number of fellowships. I am sincerely grateful for funding received from the NSF-Integrative Graduate Education and Research Traineeship (NSF-IGERT) (DGE-0221664), NSF-GK12 Fellowship, and Dean's Fellowship. I also must express my sincerest gratitude toward the family of George Hill for additional funding. I apologize to all those who I may have forgotten or missed, I thank you for helping me make it this far.

Contents

Acknowledgements	iii
List of Figures	vii
Abbreviations	xi
Abstract	xiii
1 Introduction	1
2 Fundamentals of Ferroelectricity	4
2.1 General	4
2.2 Piezoelectricity	5
2.3 Thermodynamics	7
2.4 Ferroelectricity at the Nanoscale	9
2.5 Strain/Stress Effects	11
2.6 Surface Chemical Environment	11
2.7 Ferroelectric Domains	13
3 Synthesis and Fabrication of Ferroelectric Test Nanostructures	15
3.1 Bottom Up Synthesis	15
3.2 Chemical solution methods	16
3.3 Anodic Aluminum Oxide - AAO	17
3.4 Sol-Gel Processing	19
3.5 AAO-assisted Electrodeposition	20
3.6 AAO-assisted Silicon Nanowire Growth	23
3.7 Structural Characterization	29
3.8 Electron beam lithography	30
4 Piezoresponse through a Ferroelectric Nanotube Wall	34

4.1	Scanning Probe Microscopy - Basics	34
4.2	Piezoresponse Force Microscopy	35
5	Finite Curvature-Mediated Ferroelectricity	42
6	Integrated Nanowire Ferroelectric Field Effect Transistor (Fe-FET)	51
7	Redox-Based Resistive Switching of Ferroelectric Nanotubes	60
	Bibliography	67
A	Matlab Coding for Numerical Calculations	81
A.1	ODE Solver	81
A.2	SSNODE Solver	82
A.3	SSN Script	84
A.4	LK solver	86
A.5	Simple Solver	86
A.6	SigmaC	87
A.7	Solve for V	88
A.8	cylinder stress	90
A.9	Temperature profile P	90
A.10	plots	91
A.11	P oft	93
A.12	P int	94
Vita		95
A.13	Publications and Patents	95

List of Figures

2.1	Energy vs. Polarization profile for a ferroelectric system.	4
2.2	Example of ferroelectric hysteresis. Shown around the loop are varying tilts of the energy landscape under the application of an external electric field \mathbf{E}	5
2.3	Illustration of a FE thin film between two metallic electrodes. Shown are incomplete screening at the FE/electrode interface, resulting in a depolarizing field E_d forming opposite the spontaneous polarization P_s	10
2.4	Schematic of a - 180° and b - 90° domains within an tetragonal ferroelectric perovskite lattice.	13
3.1	a Top view SEM image of AAO prepared using oxalic acid (scalebar = 1 μ m), b Higher mag top view SEM image of AAO (scalebar = 100 nm), c side view SEM image of AAO template (scalebar = 1 μ m). 18	18
3.2	a - a cross section of the AAO template embedded with PZT nanotubes PZTNT, b - an array of exposed PZTNT after a partial etch of the templates in 6 M NaOH, c - higher mag SEM image of exposed PZTNT arrays, d - a cross section of an AAO template embedded with PZTNT, e - an array of PZTNT (top view) after a partial etch, and f - freestanding PZTNT dispersed on a silicon substrate after a full etch of the AAO template	21
3.3	Illustration of the electrochemical setup for cathodic reduction within AAO. Shown are the backcoated AAO template serving as a cathode with a noble metal platinum mesh serving as the anode. The enlarged image shows the plating mechanism.	22
3.4	<i>left</i> secondary electron SEM image of AuNW-embedded AAO templates; <i>right</i> backscattered electron SEM image of the same area.	22
3.5	a Au catalyst segments grown with a high current density J , b Au catalyst segments grown with a proper current density, leading to higher uniformity	23

3.6	a Au catalyst segments within AAO, b SEM cross section image of AAO template after growth in CVD, showing wires extending from template surface, c cross section SEM image of SiNW grown in PZTNT-embedded AAO, d SEM image of SiNW grown out of the AAO surface, showing distinct Au-catalyst ends <i>bright contrast</i> , e cross section SEM image of SiNW grown in PZTNT-embedded AAO	25
3.7	a EDS of Si-PZT nanowires embedded in AAO, b-c SE and BSE SEM images of partially etched Si-PZT nanowire arrays in AAO (<i>top view</i>), d-e SE and BSE SEM images of partially etched Si-PZT nanowire arrays in AAO (<i>side view</i>)	27
3.8	SEM image of freestanding a hollow PZTNT and b Si-PZT nanowires dispersed on a silicon-SiO ₂ substrate, d-e SEM images dispersed Si-PZT nanowire species	28
3.9	(a), X-ray diffraction of nanotubes within the AAO template. Indexed peaks are of tetragonal perovskite; all remaining indices are assigned to the AAO. (b), Raman spectrum of an individual 100 nm PZT nanotube in which the observed modes of tetragonal perovskite are denoted.	30
3.10	(a), TEM image of two 50 nm diameter Au-PZT core-shell nanowires, scalebar = 50 nm. Upper inset, electron diffraction of a bundle of Au-PZT nanowires. Lower inset, empty 200 nm PZT nanotube, scalebar = 50 nm. (b), (false color) SEM image of a single nanowire, scalebar = 1 μ m.	31
3.11	typical alignment pattern used in the EBL patterning of nanowires, prior to nanowire dispersion; scalebar = 10 μ m.	32
3.12	a a SiNW-PZT core-shell nanowire contacted using EBL, b a two-step EBL contact process resulting in a third (gate) electrode; both scalebars = 1 μ m.	33
4.1	a Illustration of the operating principle of SPM; the deflection of the cantilever δ is read by a 4-quadrant photodiode Δd creating a feedback which yields topographic information, b The forces associated with the tip-sample interactions during use of SPM.	35
4.2	Schematics of the converse piezoelectric effect on FE particles on a surface, with a and b representing positively and negatively poled normal FE polarizations and c and d positively and negatively poled lateral polarizations, respectively. legend shows a typical experimental configuration.	36

4.3	(a) (false color) height map of a 100 nm Au-PZT coaxial nanowire. (b) experimental scheme for collecting (c) ferroelectric piezoelectric hysteresis and (d-f) plane-normal piezoresponse phase contrast maps. (d) represents the “as found” state with (e) and (f) revealing written negative and positive ferroelectric domains, respectively (dashed circles).	38
4.4	FTIR spectrum of 100 nm PZT nanotubes. Inset shows an enlarged view of the 3650 cm^{-1} peak, resulting from surface terminated hydroxyl species. The large peak at 2925 cm^{-1} corresponds to C-H stretching modes.	39
5.1	a Illustration of the electrically interfaced nanoshell and measurement, along with an the electron micrograph of a representative nanowire (inset scale bar = $1\ \mu\text{m}$). b-e Measured FE piezoelectric hysteresis loops collected from the oxide perovskite nanoshells, for shell thicknesses ζ and corresponding inner radii a as denoted in the legend. The inset in the upper left of a is a plot of the measured phase response of a shell as a function of voltage bias applied across its wall, indicating ferroelectric switching of the shell polarization.	44
5.2	a Measured variation of the FE piezoelectric response with curvature, compared with those for planar thin films of identical composition (NagyAPLcompare), and a scatter plot of the calculated volume-averaged polarization (right axis). b Coercive electric field E_C plotted as a function of shell thickness $\zeta = b - a$. c Measured vertical center-of-switching (COS) offset values of the FE hysteresis for each nanoshell. d Horizontal (voltage) COS offsets (solid squares connected by solid lines), plotted as a function of nanoshell outer radius b . Also shown in c and d , respectively, are the corresponding calculated polarization and voltage offsets.	46
5.3	a Calculated (300 K) radial polarization profile for selected values of shell inner and outer radii a and b , respectively (solid lines), and for planar, stress-free thin films of corresponding thicknesses (dashed lines). b Calculated volume-averaged P_r as a function of temperature for the nanoshells of selected diameters and thicknesses (solid lines), and for planar, stress-free thin films of corresponding thicknesses (dashed lines) plotted in a ; the inset illustrates the model geometry. In a and b the bulk polarization value is denoted by horizontal dashed black lines, and in b the bulk T_C value is denoted by a vertical dashed line.	48
6.1	Schematic of the nMOS architecture	52
6.2	Band diagrams of a-b nMOS and c-f FeFET memory platforms	53
6.3	Electrically contacted SiNW core, PZT-shell nanowires using combined FIB ion milling and EBAD Pt deposition	53

6.4	Illustration of the experimental setup used for gated measurements of I-V through the nanowire core. A sourcemeter is attached to the gate while a picoammeter is attached to the source-drain of the nanowire channel. A gate voltage (V_G) is applied directly to the wrap gate electrode, then removed to collect current, as shown in Figure 6.6	54
6.5	Collected I_{sd} -V traces of an individual Si-PZT NW FeFET	56
6.6	a Collected I_{sd} -V traces of an individual Si-PZT NW FeFET, measured after gate voltages V_G were applied and withdrawn. b Log-scale plot of the traces shown in a	57
6.7	a SEM image of a gated Si-PZT integrated FeFET nanowire with HfO_2 buffer layer. b Drain-source current (@ $2V_{SD}$) versus gate voltage taken of the contacted nanostructure shown in a	58
7.1	a - schematic of simultaneous IV-hysteresis collection where an arbitrary waveform consisting of two frequency components is applied directly to the Au-core inner electrode, as described in the main text. b Topographic AFM height image of a contacted 50 nm core-shell nanostructure (scan size $5 \times 5 \mu\text{m}$). c - ferroelectric piezoelectric hysteresis (<i>grey markers</i> , left axis) and resistive current-voltage (<i>black line</i> , right axis) simultaneously collected by a grounded conductive cantilever connected to a transimpedance amplifier. The bias $V_{core-tip}$ is applied from the nanowire core through the FE nanotube wall and collected at the tip, hence the reverse x-axis.	62
7.2	a - (<i>false color</i>) SEM image of top-electroded core-shell nanostructure, showing measurement path between Pt-top electrode (shell ; <i>red</i>) and left nanowire-core electrode (core ; <i>blue</i>) (scalebar = $1 \mu\text{m}$). b - representative resistive current-voltage character of a shell-electroded Au-core, PZT-shell nanostructure. c - log-based plot of current-voltage showing an order of magnitude difference in current across the finite-thickness direction of the core-shell nanostructure.	64
7.3	Current - voltage sweeps of a Au-PZT core-shell nanowires after a a - O_2 -rich/ b - O_2 -deficient/ c - O_2 -rich annealing cycle.	65

Abbreviations

AAO	Anodic Aluminum Oxide
AFM	Atomic Force Microscopy
BSE	Backscattered Electron
BTO	Barium Titanate (BaTiO_3)
COS	Center of Switching
CVD	Chemical Vapor Deposition
DFT	Density Functional Theory
DI	Deionized Water
EBAD	Electron Beam Assisted Deposition
EBL	Electron Beam Lithography
EDEP	Electrodeposition
EDS	Energy Dispersive Spectroscopy
FE	Ferroelectric
FeRAM	Ferroelectric Random Access Memory
FeFET	Ferroelectric Field Effect Transistor
FIB	Focused Ion Beam
FTIR	Fourier Transform Infrared Spectroscopy
IV	Current-Voltage
NP	Nanoparticle
NT	Nanotube
NW	Nanowire
PFM	Piezoresponse Force Microscopy

PMMA	Poly(Methyl Methacrylate)
PZT	Lead Zirconate Titanate [Pb(Zr,Ti)O ₃]
RS	Resistive Switching
SAED	Selected Area Electron Diffraction
SE	Secondary Electron
SEM	Scanning Electron Microscopy
SPM	Scanning Probe Microscopy
TEM	Transmission Electron Microscopy
VLS	Vapor Liquid Solid
XRD	X-ray Diffraction

Abstract

Integrated Non-Planar Ferroelectric Nanostructures

Stephen S. Nonnenmann

Jonathan E. Spanier, Ph.D.

Ferroelectrics (FEs) exhibit stable spontaneous polarization states in the absence of an applied electric field, analogous to other ferroic systems such as ferromagnetics and ferroelastics. Incomplete screening of surface charges along the FE-electrode interface creates a potential gradient across the FE layer. This yields a depolarizing field which greatly suppresses polarization, particularly in systems approaching finite sizes, where surface and interface effects exhibit far more influence than in the bulk. Identifying mechanisms for reducing the detrimental effects of the depolarizing field and maintaining FE stability in finite dimensions remains the largest obstacle in FEs realizing their potential as next generation devices such as electrocaloric coolers, actuators, sensors, photovoltaics, and non-volatile memory elements.

This thesis aims to develop a reproducible, versatile synthetic approach towards conductive core-ferroelectric perovskite oxide shell nanostructures. A test structure fabrication approach will then be developed, yielding working conductive inner nanowire core electrodes for interrogation of FE properties across the finite (radial) dimension. Here, mapping of the normal ferroelectric polar components within low dimensional FE, with consideration of surface chemical environment effects will be explored. The effects of finite-curvature and its resulting stress gradients in stabilizing ferroelectricity at the nanoscale will also be identified and explored. The nonvolatile gating effects of the FE layer on the transport properties of a low-dimensional semiconductor channel will be investigated. Finally, FE switching will be correlated with system leakage currents, and the effects of oxygen partial pressure, as basis for potential resistive switching memories.

question



Chapter 1

Introduction

Ferroelectric (FE) materials exhibit a spontaneous polarization which may be manipulated using an external applied electric field. A positively or negatively oriented polarization can represent “1” and “0” Boolean logic states in storing information. This is the basis for FE-based nonvolatile memory platforms such as Ferroelectric Random Access Memory (FeRAM). These materials also offer piezoelectric properties, which are useful in applications involving pressure sensors, actuators, and microelectromechanical systems (MEMS). FEs also are used in electro-optic applications such as modulators, holographic data storage, and frequency converters. The fundamental physics behind the operation of these applications will be introduced in Chapter 2.

The basis for operation of any application involving FEs is the ability to carefully control the orientation of its polar state. The total free energy within a FE system is dominated by a balance of electrostatic and elastic contributions. As a result, it is energetically more favorable in nanostructured FE materials for multiple domains to evolve, which assist in lowering the energy associated with large depolarizing fields. Through selective patterning the film or material polarization may form either a monodomain or multidomain configuration, which may provide optimal performance depending on the desired application.

Increasing bit density within nonvolatile memory elements necessarily involves the miniaturization of devices, with a natural size reduction of FE materials implemented within the device architecture. Size scaling of FEs introduces detrimental effects caused by the depolarizing field, which arises from incomplete screening of surface charges along the FE/electrode interface. These fields effectively destabilize the FE polarization by forming in the opposite direction across the material thickness. As such, understanding the underlying physics of these size-limited phenomena requires careful experimental observation of the local response of FE materials, specifically of the conservation of FE polar character as it deviates from its bulk state.

The motivation for this research then has been to identify an integrated, coaxial system consisting of a functional (semiconducting, conductive) core and a thin, nanoscale FE oxide shell for potential use as an individual nonvolatile memory element. The selection of a cylindrical topology additionally serves as a test platform to propose and provide evidence for a new design principle incorporating finite-curvature as a stabilizing mechanism for nanoscale FE. This study has explored nonvolatile operation mechanisms including FE field effect transistors (FeFET) and resistive switching (RS).

Chapter 2 will review the fundamental physics of nanoscale FE systems necessary to understand the experimental background and discussion of results found throughout the study. This includes but is not limited to ferroelectricity, piezoelectricity, depolarizing effects, surface environment, strain effects, and shape effects.

Developing a versatile synthetic approach robust enough to produce nanoscale arrays consisting of FE shells with varying core materials has been a central part of this study. The details of the template-assisted growth processes used are found in Chapter 3. Here the fabrication steps necessary to create electrically viable test structures using electron beam lithography may also be found.

Piezoresponse force microscopy (PFM) is a modified scan probe technique utilizing a lock-in amplifier to apply a bias to a conductive cantilever tip in contact with the material surface, inducing a piezoelectric deflection via the converse piezoelectric effect. This technique can be used to image FE domain states or manipulation of the FE state in scanning mode, or collect localized FE piezoelectric

hysteresis in a static probe setup. Chapter 4 concentrates on the experimental setup and discussion of PFM scan mode operation in identifying the FE state of an individual test nanostructure.

Developments in the production of high quality oxide substrates have allowed researchers to engineer specified strain states with ultrathin FE films. The concepts of nonlinear electromechanical coupling through the electrostrictive properties of dielectric FE materials will be introduced in Chapter 5. This section will also review and discuss experimental evidence for finite-curvature, surface-tension based stabilization of FE properties along the finite-thickness direction of individual nanostructures. The findings presented in this section will be corroborated with numerical calculations incorporating a modified Landau stiffness into the free energy expansion, with comparisons given between nonlinearly coupled surface tension-induced stresses and planar, stress-free thin films.

Chapter 6 will explore the merits of these integrated test structures in terms of nonvolatile field effect gating, as interrogated via electrical transport measurements. Here the experimental design and execution for measuring individual semi-conducting silicon-core, FE oxide-shell nanostructures will be discussed. Experimental evidence for transconductance in nanowire channels is presented, with comparison to recent literature of thin film FeFET and non-integrated semiconductor nanowire, FE thin film transistor test structures.

Leakage currents present a major problem in the integration of FE and other dielectrics within silicon-based memory architectures. As such, a major goal of studying these nanostructures was to electrically characterize the current across the finite, radial dimension of individual FE nanotubes. In Chapter 7 the resistive switching character of the leakage response of fabricated test structures are shown. The experimental scan probe technique enabling simultaneous collection of FE hysteresis and resistive current response is presented. Additional test structures consisting of lithography-based electrodes further clarify the resistive switching character, with a focus on the effects of oxygen environment in mediating transport. These studies provide evidence for an oxygen-vacancy transport mechanism, which will be discussed in terms of nonstoichiometric perovskite lattice chemistry.

Chapter 2

Fundamentals of Ferroelectricity

2.1 General

Ferroc systems generally exhibit two non-zero, equilibrium spontaneous polar states in the absence of an applied field, i.e. magnetic fields, electric fields, or mechanical stress. As a note, more polar states may be allowed due to crystal symmetry, as is the case for lead zirconate titanate, exhibiting six. Figure 2.1 represents a simple energy vs. polarization profile for normal ferroelectric (FE) systems, consisting of two wells at zero energy, or a spontaneous polarization at zero applied bias. There also exists an energetic barrier between these states which requires an external field to overcome.

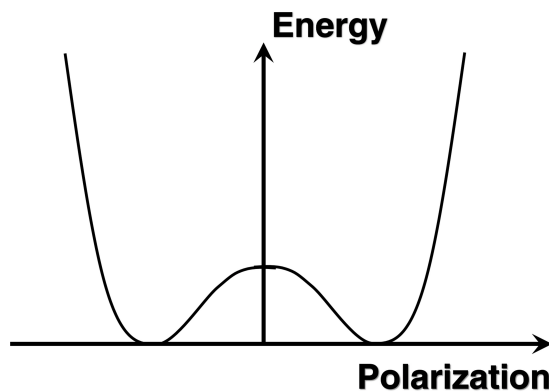


FIGURE 2.1: Energy vs. Polarization profile for a ferroelectric system.

Ferroelectric hysteresis describes the history of the material response to the application of an external applied electric field E . This is shown pictorially in Figure 2.2. Hysteretic behavior takes the form of a loop, where the *spontaneous polarization* is found at equal, non-zero points at zero applied bias. This is represented as the energy wells found in Figure 2.1. The materials maintains its polar state as the field is cycled until a critical field called the *coercive field* E_C is reached. In terms of the energy vs. polarization profile found in Figure 1, the application of the E field effectively tilts the energy well, until a sufficient field is applied as to surpass the energetic barrier, and thus switch the polarization orientation.

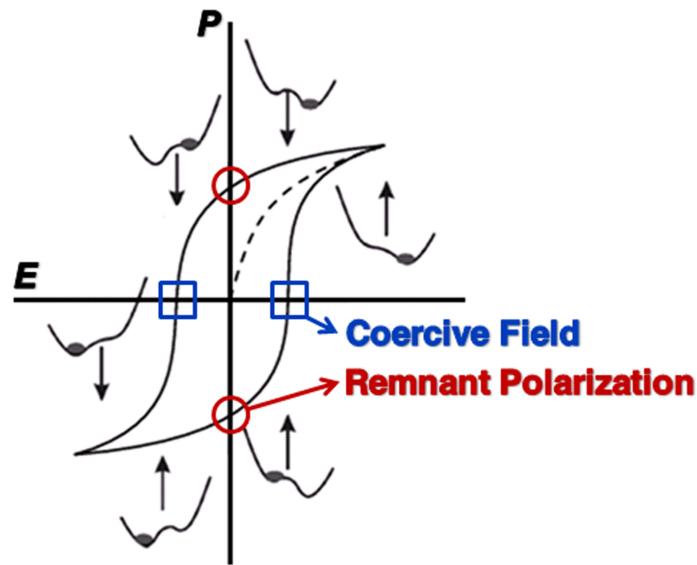


FIGURE 2.2: Example of ferroelectric hysteresis. Shown around the loop are varying tilts of the energy landscape under the application of an external electric field E .

2.2 Piezoelectricity

The word *piezoelectric* originates from the Greek word *piezein*, meaning to squeeze or press, and *piezo*, Greek for "push". The *direct piezoelectric effect* describes the phenomenon by which a material produces an electrical charge density D under the application of stress X along specified crystallographic orientation:

$$D_i = d_{ijk}X_{jk}$$

where d_{ijk} represents the piezoelectric tensor elements. Convention is to compact the notation of this 3rd rank to the 2nd rank tensor, due to the symmetry with respect to the commutability of the k and j suffixes, which lead to substitution of the pair jk by one, resulting in an overall reduction in tensor components from 27. The work presented in this thesis will assume summation over equal indices.

The *converse piezoelectric effect* describes the phenomenon by which a material physically displays a strain x under the application of an electric field \mathbf{E} along a specific crystallographic orientation. The total strain of a system, including quadratic electrostrictive terms, takes the form [1]:

$$x_{ij} = x_{s_j} + s_{ij}X_j + d_{ij}E_j + M_{ijkl}E_kE_l$$

where x_{s_j} is spontaneous strain, s_{ij} elastic compliance, and M_{ijkl} the electrostrictive coefficient. A piezoelectric coefficient d_{ij} measured along the direction of the applied \mathbf{E} field is called the *longitudinal* coefficient; those measured along a direction perpendicular to the \mathbf{E} field is termed the *transverse* coefficient. The ferroelectric system used throughout this thesis is lead zirconate titanate (PZT); the tetragonal ferroelectric phase has $4mm$ symmetry where there only exists a non-zero polarization state along the $\langle 111 \rangle$ direction. There also exists 7 non-zero piezoelectric coefficients. This study primarily discusses the d_{33} coefficient, though reference to d_{31} may also be made throughout the document. The electrostrictive effect may also be expressed as a vector of induced polarization [1]:

$$x_{ij} = Q_{ijkl}P_kP_l \quad (2.1)$$

where M_{ijkl} and Q_{ijkl} , the field- and polarization-related electrostrictive coefficients, are related through the dielectric susceptibility:

$$M_{ijkl} = \chi_{km}\chi_{ln}Q_{ijkl}$$

Materials exhibiting piezoelectricity and spontaneous polarization are referred to as *pyroelectric*. If the polarization orientation may be manipulated with an

applied electric field it is considered a ferroelectric. This means that all ferroelectrics are necessarily piezoelectric materials, but not all piezoelectrics can be ferroelectrics.

2.3 Thermodynamics

In the last section ferroelectrics were described as a subset of a larger class of materials called pyroelectrics. The ability for ferroelectrics to switch their polar orientation under an applied electric field results from very small atomic displacements within the crystal lattice that result in a non-centrosymmetric phase, and hence a net dipole moment. Commonly a half-shift in the atom positions is created by a temperature change which results in a centrosymmetric, non-polar phase. This means that ferroelectrics exhibit a phase transition temperature above which they are centrosymmetric and non-polar. Analogous to ferromagnetic theory for susceptibility, the dielectric constant obeys the Curie-Weiss law above the transition temperature [2]:

$$\epsilon = \frac{A}{T - T_C} \quad (2.2)$$

where T_C is the *Curie temperature* or *ferroelectric phase transition temperature*. As a note, dielectric constants for ferroelectrics range on the order of hundreds to thousands. Thermodynamic principles may then predict that a transition from a polar, non-centrosymmetric phase to a non-polar, centrosymmetric phase can result in other significant changes to material properties. For example, any polarization will necessarily be accompanied by a strain within the lattice.

The reversible change in internal energy U for an elastic dielectric material under a change of strain dx , electric displacement dD , and entropy dS can be described by the first and second laws of thermodynamics:

$$dU = TdS + X_{ij}dx_{ij} + E_idD_i$$

with T representing the temperature of the material. Considering isothermal conditions, and \mathbf{E} field and stress \mathbf{X} as independent variables, a Legendre transformation of the U term may be used to switch the set of independent variables from (S, x, D) to (T, X, E) by adding the terms $-Ts - Xx - ED$ to the U term. This results in a free energy term, or *Gibbs free energy* G [3, 4]:

$$G = U - TS - X_{ij}x_{ij} - E_i D_i \quad (2.3)$$

or the differential:

$$dG = -SdT - x_{ij}dX_{ij} - D_i dE_i \quad (2.4)$$

The Gibbs free energy may be expressed as a Taylor series expanded in terms of the new independent variable set (T, X, E) [5]:

$$\begin{aligned} \Delta G &= \frac{\partial G}{\partial T} \Delta T + \frac{\partial G}{\partial D_i} D_i + \frac{\partial G}{\partial X_{ij}} X_{ij} + \frac{1}{2} \frac{\partial^2 G}{\partial T^2} \Delta T^2 \\ &+ \frac{1}{2} \frac{\partial^2 G}{\partial D_i \partial D_j} D_i D_j + \frac{1}{2} \frac{\partial^2 G}{\partial X_i \partial X_j} X_i X_j + \frac{\partial^2 G}{\partial T \partial D_i} \Delta T D_i \\ &+ \frac{\partial^2 G}{\partial D_i \partial X_{kl}} D_i X_{kl} + \frac{\partial^2 G}{\partial T \partial X_{kl}} \Delta T X_{kl} + \dots \end{aligned}$$

Here we see how thermodynamics describes the relationship between thermal, electrical, and mechanical properties within a given material system. In this expansion of the elastic Gibbs free energy each partial derivative represents a physical phenomenon. This includes electrocaloric, piezocaloric, pyroelectric effects, as of heat capacity and thermal expansion, amongst others. This study concentrates on piezoelectric effects, described as [5]:

$$\begin{array}{ll} dX_{ij} + \left(\frac{\partial x_{ij}}{\partial E_k}\right)_{T,X} dE_k & dT + \left(\frac{\partial D_{ij}}{\partial X_{jk}}\right)_{T,E} \\ \text{converse piezoelectricity} & \text{direct piezoelectricity} \end{array}$$

or in terms of the converse or direct piezoelectric effect, with coefficients d_{ijk} :

$$d_{ijk}^{T,X} = \left(\frac{\partial x_{ij}}{\partial E_k}\right)_{T,X} = -\left(\frac{\partial^2 G}{\partial E_k \partial X_{ij}}\right) \quad d_{ijk}^{T,E} = -\left(\frac{\partial^2 G}{\partial X_{ij} \partial E_k}\right) = \left(\frac{\partial D_k}{\partial X_{ij}}\right)_{T,E} \quad (2.5)$$

converse piezoelectric effect *direct piezoelectric effect*

The thermodynamic equivalence shown above can be shown for all other physical properties described by the partial differentials in the Gibbs free energy expansion. Taking the Legendre transformations of the internal energy using all the other thermodynamic equivalences lead to the Maxwell relationships. In the case of most ferroelectric oxides, the paraelectric phase is centrosymmetric, meaning any coefficients associated with odd-rank tensors are null. For this reason one will find the expansion of G up to either fourth-order or sixth-order terms. Considering a system under fixed T , X , and E a stable system may be observed with G at its minimum:

$$G = G_o - \vec{E} \cdot \vec{D} \quad (2.6)$$

Taking the first derivative of 2.6 results in equations for the polarizations and strains developed by ferroelectrics under specified electric and mechanical boundaries. This is the thermodynamic basis in understanding ferroelectric properties.

2.4 Ferroelectricity at the Nanoscale

The thermodynamic approach to ferroelectrics thus far has assumed a bulk-like form. As the size or thickness of ferroelectric materials approach finite size scales on the order of < 100 nm, there exist changes to the local spontaneous polarization due to interactions with the free surface. Similar to surface effects in other ferroic systems, a depolarizing field forms opposite the polarization direction due to uncompensated surface charges [6]. In many cases metallic or metallic-like

electrodes are placed on either side of the ferroelectric layer to assist screening these charges. Unfortunately most often the electrodes possess structural defects [7, 8] which lead to incomplete screening of the surface charges, and hence the development of a destabilizing depolarizing field across the thickness, as shown pictorially in Figure 2.3 below.

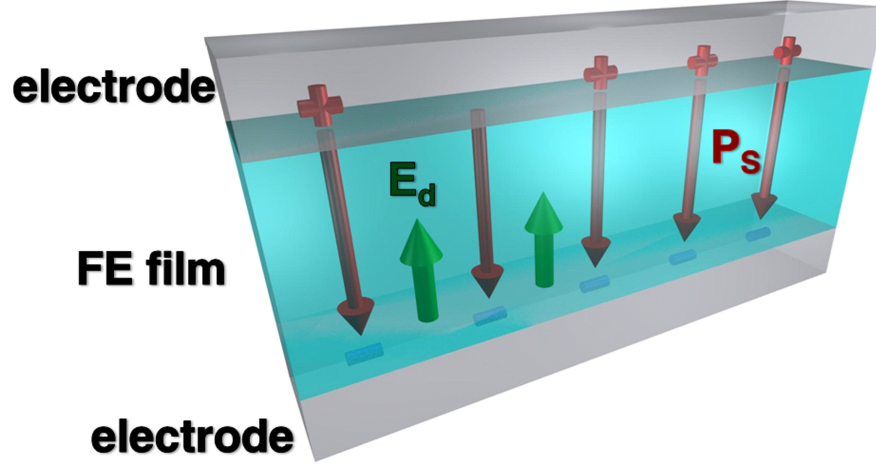


FIGURE 2.3: Illustration of a FE thin film between two metallic electrodes. Shown are incomplete screening at the FE/electrode interface, resulting in a depolarizing field E_d forming opposite the spontaneous polarization P_s

Landau and Ginzburg first developed the boundary conditions by which to best describe a ferromagnetic thin film 60 years ago [9]. Their mean field theory was later adapted by Devonshire [2] using a different order parameter. Here, the Gibbs free energy is shown as an expansion out to the sixth-order terms:

$$G = \int_a^b \left[\frac{A}{2} P_r(r)^2 + \frac{B}{4} P_r(r)^4 + \frac{C}{6} P_r(r)^6 + \frac{1}{2} g (\nabla P_r)^2 - E_d(r) P_r(r) \right] r dr + \frac{D}{2\delta} \int_S P_r^2 dS. \quad (2.7)$$

where P represents polarization, $A = A_o(T - T_C)$, T is absolute temperature, T_C the Curie temperature, with A_o , B , C , and D all material parameters. Other parameters include, g , the energetic cost associated with variation of P_r near the surface, and δ , the extrapolation length, a correction term proportional to the surface area. This effectively serves to help measure the strength of all the

surface effects, represented as the second integral term found in 5.2. For more details about this equation or how it is derived please refer to these classic articles [10, 11, 12]. The expansion of the Gibbs free energy will be revisited in Chapter 5 when discussing the effects of curvature on stabilizing nanoscale ferroelectricity.

2.5 Strain/Stress Effects

The observation of depolarizing effects in nanoscale ferroelectric thin films and nanostructures due to depolarizing fields placed intense interest in combating these effects with various stabilizing mechanisms. In recent years a number of strategies, including, e.g. strain engineering for enhancing stability and polar properties [13], and for inducing a ferroelectric phase in an otherwise paraelectric material [14], and the use of artificial superlattices [15, 16, 17] have been implemented to mitigate the reduction or loss in P in the limit of finite size, and the decrease in T_C , or to otherwise manipulate the character of the ferroelectric polarization and/or hysteresis.

Developments in oxide growth techniques such as oxide molecular beam epitaxy and pulsed laser deposition have created an array of extremely high quality, exotic oxide substrates used to generate specified, engineered strain states within the ferroelectric perovskite oxide films grown directly on them. Ferroelectric films have also been grown directly onto silicon using this method [18], thus avoiding widespread usage of these expensive substrates. These systems requires the benefit of nonlinear electrostrictive coupling described by equation 2.1. Curvature-driven stress gradients have also been theoretically and experimentally verified to enhance ferroelectric stability in nanostructures such as nanowires and nanotubes. This will be covered in detail in Chapter 5.

2.6 Surface Chemical Environment

The preceding section outlined the importance of compensation of polarization-induced surface charges as a stabilizing factor for nanoscale ferroelectricity, where

incomplete screening of these charges results in a depolarization field that opposes the bulk polarization, thereby suppressing the polar state. Recent experimental evidence of room-temperature ferroelectric stability in several-monolayer and single-phase ultra-thin films [19, 20, 21] and freely-standing nanostructures [22, 23] in the absence of metallic electrodes (an increasingly common and important experimental configuration) has opened a line of inquiry into another potential strategy for engineering ferroelectric stability and increased functionality by harnessing the influence of molecular adsorbates on ferroelectric stability. More recently, combined experimental and theoretical investigations involving nanoscale ferroelectricity [22] resulted in the first demonstration of a new mechanism for the screening of surface charge on ferroelectric nanostructures by atomic and molecular adsorbates.

question

What causes this mechanism? Previous studies had shown that surface hydroxylation is prevalent in oxides, including BaTiO₃, especially when these oxides are prepared by wet chemical methods, and that chemisorbed OH is stable in an ultrahigh-vacuum environment at elevated temperatures (> 670 K) [24]. These molecular adsorbates can compensate the surface polarization charges, providing a mechanism for reducing the depolarizing field.

Molecular adsorption-mediated ferroelectricity was observed and reported in a separate series of theoretical and experimental investigations carried out on ultra-thin films in a controlled atmosphere involving probing of ferroelectric distortions using X-ray reflectivity [21, 25]. In a separate series of experiments and calculations involving thin films Li et al. [26] proposed an interesting mechanism for molecular adsorption along ferroelectric surfaces by which molecules remain trapped in a physisorption energy well, under the influence of the surround ferroelectric domain state, site-independent. While many species quickly desorb from the surface, any molecule that finds an active site, most commonly an oxygen vacancy, chemisorption and bond formation occurs. Modified scanning probe techniques, such as scanning surface potential microscopy (SSPM) or piezoresponse force microscopy (PFM) are sensitive to adsorbed species along a ferroelectric surface, as they indicate finite differences in the domain response as a function of adsorbed species. Density Functional Theory (DFT) simulation results were used in [26] to demonstrate the remarkable effectiveness of molecular adsorbates as screening

agents. Selection of oleate ligands left the electropositive HCO fragments preferring the anion species while the electronegative species HCOO preferred the cation sites. Depending on the presence of electronegative or electropositive adsorbates, bulk like ferroelectricity was demonstrated for positive (upwards, out of plane) and negative polarizations (downwards, out of plane), respectively. These results are in stark contrast to those found for ferroelectric films [27] sandwiched between two metallic and oxide electrodes, which do not exhibit ferroelectric stability at comparable length scales (< 1 nm).

2.7 Ferroelectric Domains

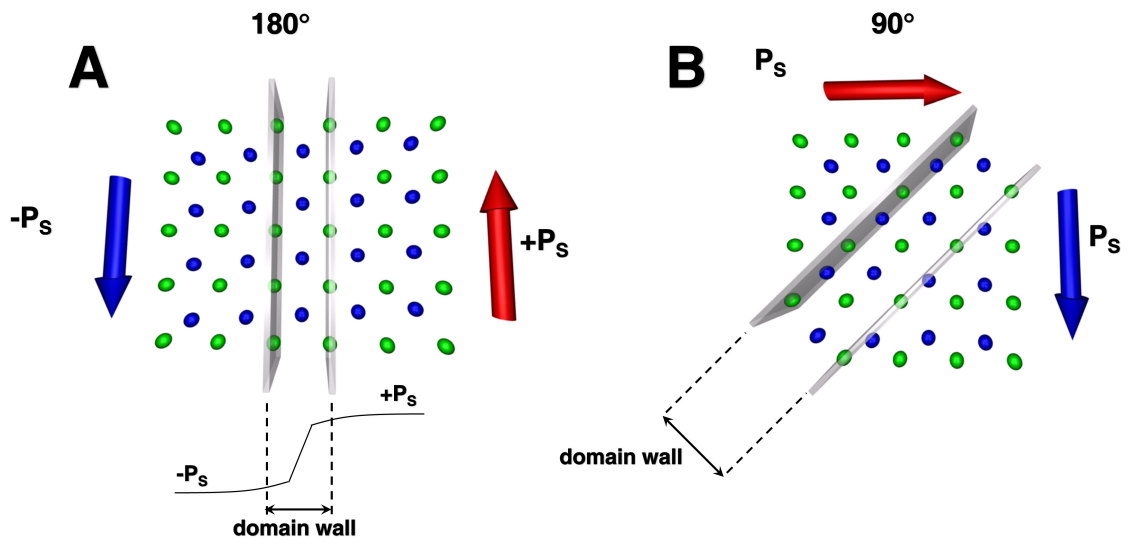


FIGURE 2.4: Schematic of **a** - 180° and **b** - 90° domains within an tetragonal ferroelectric perovskite lattice.

A *domain* describes a volume of uniform polar orientation. Energetically monodomain states are not favored, as they lead to large depolarizing fields. As such, ferroelectric systems spontaneously split into multiple domain states (Figure 2.4a-b) separated by *domain walls*. The domain size is then dictated by the energetic cost in forming domain walls, G_w [28]. Under a sufficient driving force a domain walls will move, resulting in a change of polar orientation called *switching*. Typically switching occurs under the application of an external magnetic field, electric field, mechanical stress, or some combination thereof. As this study focuses

on ferroelectric materials, there will no longer be any mention of magnetic fields, ferromagnetic behavior, or ferroelastic behavior.

To emphasize the significance here, domains form as to reduce the electrostatic energy costs of the formation of the depolarizing field. This is particularly important in nanoscale systems, where compensation for the depolarizing field takes the form in screening through metallic electrodes and the spontaneous formation of ferroelectric domains. Note, domain walls are necessarily *charge neutral*. These domains may be experimentally verified through surface sensitive techniques such as piezoresponse force microscopy (PFM), a modified scanning probe microscopy technique which implements a lock-in amplifier to induce and measure a piezoelectric deflection within a ferroelectric system via the converse piezoelectric effect. This will be covered in more detail in Chapters [4](#) and [5](#).

Chapter 3

Synthesis and Fabrication of Ferroelectric Test Nanostructures

Developing a versatile synthetic approach robust enough to produce nanostructure arrays consisting FE shells with varying core materials has been a central part of this study. The details of the template-assisted growth processes used are found in Chapter 3. Here the fabrication steps necessary to create electrically viable test structures using electron beam lithography may also be found.

3.1 Bottom Up Synthesis

The sub-micron lithographic, ion-beam and reactive ion etching procedures used in traditional so-called "top-down" fabrication yield well-defined nanostructures, however the poor adsorption capacity of high- κ ferroelectrics can lead to damaged, negatively polarized surfaces [29]. Within the last decade, the high demand for increased bit capacity in memory elements, coupled with persistent challenges in reducing the sizes of fabricated elements via so-called "top-down" methods has generated expanding interest in non-planar, so-called "bottom-up" synthetic approaches. These latter methods-involving physical or chemical vapor deposition or chemical solution means, producing ferroelectric nanostructures in a range of different shapes and sizes and while utilizing both template-free [30],

and alternately, template-assisted [31] approaches. Template-free heteroepitaxial formation of ferroelectric nanostructures, using sputtering, pulsed laser deposition, and metallorganic chemical vapor deposition, have been employed to produce a range of different shapes. The shape evolution is controlled by selection of initial growth mode conditions, namely Volmer-Weber island growth or Stranski-Krastanov layer-to-island growth, and selection of substrate material relating to heteroepitaxial strain and orientation.

3.2 Chemical solution methods

Chemical solution-based methods, such as hydrothermal synthesis, sol gel processing, and solution-phase decomposition represent an attractive and cost-effective alternative to top-down approaches producing ferroelectric nanostructures for some applications [32, 33]. Some of these routes feature outstanding synthetic control of size and shape [34], and composition [35], particularly in the size range < 100 nm. Hydrothermal growth of ferroelectric nanoparticles typically requires low-temperature, high-pressure processing step of extremely basic (pH) aqueous precursor solutions, producing high quality nanocrystalline perovskites without the necessity for a post-anneal heat treatment. Sol-gel processes begin with a stoichiometric-correct quantity of metal alkoxide precursors which then undergoes a controlled hydrolysis sequence finally yielding a stable suspension of nanoparticles. These processes, like hydrothermal growth, occur at low temperatures (< 200 C), which is solely dependent upon the stabilizing agent used during hydrolysis. Unlike hydrothermal growth however, sol-gel nanoparticle powders require calcination to induce the proper ferroelectric phase transition. A modified sol-gel technique, solution-phase decomposition, adds a moisture sensitive single bimetallic alkoxide precursor to an acid mixture primarily consisting of a stabilizing agent and an alcohol, avoiding premature hydrolysis, where then a small amount of peroxide is added to slowly promote hydrolysis over an extended time window, providing excellent control over size and stoichiometry [23, 32, 35]. The as-synthesized nanoparticles are of perovskite structure and require no post-growth thermal treatment. These methods, coupled with dielectrophoresis or other

methods of assembly, may enable controlled placement on and integration of FE nano-particles with non-traditional substrates.

3.3 Anodic Aluminum Oxide - AAO

A significant barrier to application of **bottom-up synthetic approaches relates to scalability, e.g. the need to precisely locate ferroelectric nanoparticles on a wafer scale in a manner that is compatible with CMOS** and related processes, although significant progress has been made in other inorganic nanostructures [36]. Since its discovery in 1995 by Fukuda [37], the phenomenon self-organization of local etching into hexagonal close-packed arrays of columnar pores during the formation of AAO has been widely applied to the formation of arrays of nanowires and nanotubes of a variety of inorganic materials, including oxide perovskites. One feature of template-assisted growth of oxide perovskite nanowires and nanotubes is the selectable control of nanowire and nanotube diameter and length, achieved via selecting AAO pore diameter and pore length via electrochemical overpotential and length of anodization time [38]. In template-assisted growth, a sol-gel metal alkoxide precursor wets the pore via immersion, with the immersion time dictating the desired topology, i.e. longer times resulting in nanowires, and shorter times in nanotubes [39]. Template-assisted growth of some of the most technologically important ferroelectric perovskite materials: lead titanate, barium titanate, lead zirconate titanate, strontium bismuth titanate, and multiferroic barium ferrite nanowires and nanotubes has been reported, along with their structural and functional characterizations [23, 40, 41, 42, 43, 44]. Other template materials have also been employed to produce nanowires and nanotubes, including nanoporous silicon [41, 44] and nanoporous block copolymers [45]. The combined advantages of low-temperature chemical processing and ordered templated-growth to produce high yield arrays of perovskite oxide ferroelectric nanostructures demonstrate significant promise for future miniaturization of nanoscale ferroelectric capacitors [46, 47].

Anodic aluminum oxide (AAO) templates were produced from high purity Al sheets (Alfa Aesar Puratronic 99.9995% #43777) via a two-step anodization

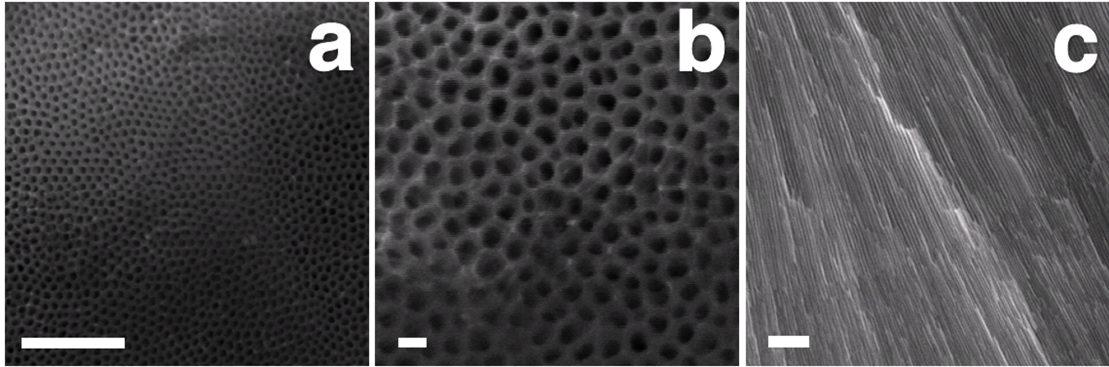


FIGURE 3.1: **a** Top view SEM image of AAO prepared using oxalic acid (scalebar = $1\mu\text{m}$), **b** Higher mag top view SEM image of AAO (scalebar = 100 nm), **c** side view SEM image of AAO template (scalebar = $1\mu\text{m}$).

process in oxalic acid (0.3 M, 1°C , 30 V) (Figure 3.1), as shown previously by Lee [48]. The motivation behind growing AAO templates was the obtainable size range; mesoporous silicon typically is on a length scale of hundreds of nm [41, 44] while AAO could be fabricated to below 10 nm. The process used in this study produced templates ranging in pore diameters from 50 - 240 nm, with thicknesses on the order of $30\mu\text{m}$. Commercially available templates (Whatman Inc. Anapore) were also used having pore diameters of 100 nm and 200 nm. The following list will highlight the entire process:

1. Degrease the as-is high purity aluminum sheet in acetone for 10 min
2. Electropolish the aluminum sheet in a 1:1 mixture of perchloric acid and ethanol for 5 min
3. Place the polished sheet inside the homemade electrochemical cell, tighten the top plates so the back surface of the aluminum is in direct contact with the copper electrode and the top surface exposed to the acid bath. The cell *must* contain a chemically neutral layer protecting the inside of the cell (especially the copper strip electrode) from exposure to the acid bath.
4. After a 30 min exposure to the acid bath, the sample is removed from the cell and the sacrificial oxide layer is removed in a mixture of phosphoric acid and chromic acid, leaving a texturized surface for the second anodization step.

5. The third step is repeated.
6. The fourth step is repeated for 24 hours to grow a thick AAO film.
7. The sample is placed in a bath of HgCl_2 to dissolve the remaining aluminum.
8. The sample is washed and rinsed repeatedly in DI water to obtain a free-standing AAO template film

3.4 Sol-Gel Processing

By definition [49] a *sol* is considered to be a colloidal suspension within a liquid, where a *colloid* represents a particle 1 - 100 nm in diameter. A *gel* is then defined as porous, connected network comprised of polymeric chains on the micron scale. The sol-gel process typically involves one of the following two methodologies

1. **Gelation** of a colloidal solution of dissolved powders
2. **Hydrolysis and polycondensation** of metallic alkoxide precursors followed by either hypercritical or ambient drying steps.

The method of choice in preparing sol-gel precursors for ferroelectric oxides is the route utilizing metallic alkoxides. Here the precursors are mixed and heated in multiple steps, first to assure a hydrolysis exchange between water and an alcohol end group. To produce the oxide, a condensation step must occur by which hydroxyl groups form water and leave a metal-oxide-metal bonded structure. This polycondensation step may occur between two hydroxyl end groups or alcohol end groups. *Note:* Most of the studies shown here used a premade commercial polymeric precursor (Chemmat 9103).

To reiterate, the combination of sol-gel chemistry and use of AAO template-assisted growth has resulted in fabrication of large arrays of one-dimensional like nanostructures of prototypical ferroelectric oxides lead titanate, barium titanate,

lead zirconate titanate, strontium bismuth titanate, and multiferroic barium ferrite [23, 40, 41, 42, 43, 44]. Here the surface energy of the alumina template dominates the growth process, where topologies are dictated by the immersion time; longer times results in nanowires, and shorter times in nanotubes [39, 50]. The formation of the nanostructures is based on the balance of interfacial energies; the surface-volume energy of the oxide surface (γ_{sv}), the surface-liquid energy of the alumina surface (γ_{sl}), and the liquid-volume (γ_{lv}) energy of the solvent (i.e. methoxyethanol). These factors form the *spreading coefficient* \mathbf{S} defined as total interfacial energy of the system [50]

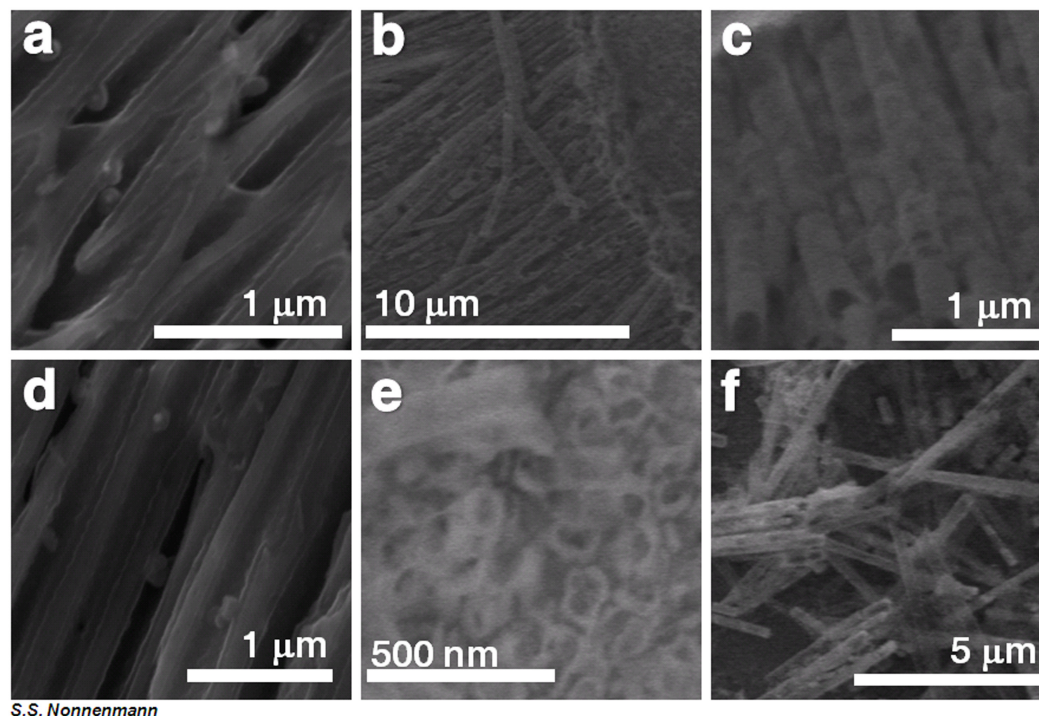
$$S = \gamma_{sv} - \gamma_{sl} - \gamma_{lv}. \quad (3.1)$$

For typical oxides (γ_{sv}) is on the order of 500-1000s mJ/cm²; the surface-liquid(alcohol) energy of alumina is 169 mJ/cm² and the liquid-volume of methoxyethanol 42 mJ/cm². This results in an \mathbf{S} value well above zero, meaning that the adhesive forces of the alumina dominate the total energy of the system. This means that as an AAO template is immersed in a sol-gel precursor, the energetically favorable path is along the bare alumina surface (due to adhesive forces) as opposed to filling the pore entirely (due to sol cohesive forces).

Figure 3.2 displays SEM images of various stages in the AAO-assisted sol-gel synthesis of ferroelectric PZT nanotube (PZTNT). The next step in the fabrication process is electrodeposition of metallic nanowires and/or metallic catalyst segments.

3.5 AAO-assisted Electrodeposition

In addition to sol-gel chemistry, AAO-assisted methods utilizing cathodic reduction of an electrochemical plating bath have also been widely deployed in developing arrays of one-dimensional like nanostructures [51]. This electrochemical method has been used to produce arrays of metallic nanostructures of dozens of noble and transition metals; the reader is referred to elsewhere for details [51, 52],



S.S. Nonnenmann

FIGURE 3.2: **a** - a cross section of the AAO template embedded with PZT nanotubes PZTNT, **b** - an array of exposed PZTNT after a partial etch of the templates in 6 M NaOH, **c** - higher mag SEM image of exposed PZTNT arrays, **d** - a cross section of an AAO template embedded with PZTNT, **e** - an array of PZTNT (top view) after a partial etch, and **f** - freestanding PZTNT dispersed on a silicon substrate after a full etch of the AAO template

as this thesis will cover the synthesis of noble metal gold nanowires and segments thereof.

Figure 3.3 represents the experimental setup for electroplating gold nanowire arrays within AAO templates. After completing the necessary synthesis steps found in sections 3.3 and 3.4 the PZTNT-embedded AAO is backcoated with a thermally-evaporated layer of Ag to serve as the sample electrode (cathode). The silver-coated area is covered in a passivation layer of nail polish (Sally Hansen Hard as NailsTM) to ensure the plating takes place within the pores and not directly on the metal surface. The sample is then placed in a beaker as the sample electrode (cathode) opposite a noble-metal Pt mesh (anode) and filled with a thiosulfate-sulfite based Au plating bath (Technic 25) and run under constant current conditions ($J = 1 \text{ mA/cm}^2$) for 1 hr. For sulfate based baths, the half reactions take the general form [53]

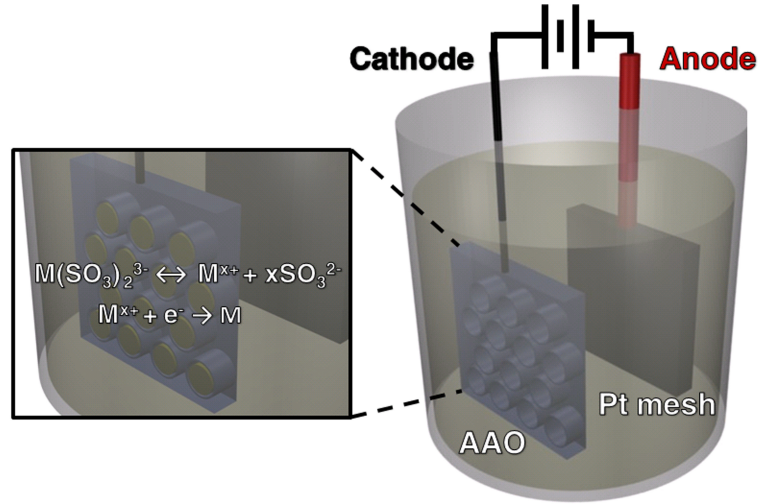
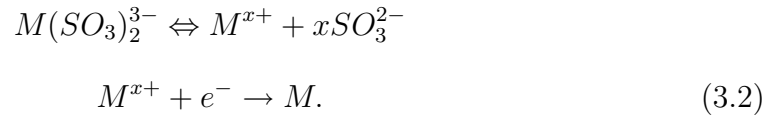


FIGURE 3.3: Illustration of the electrochemical setup for cathodic reduction within AAO. Shown are the backcoated AAO template serving as a cathode with a noble metal platinum mesh serving as the anode. The enlarged image shows the plating mechanism.



For this study $M = Au, Ag$. Cyanide based baths produce single-crystalline Au nanowires, however due to their high toxicity and extremely poor compatibility with photoresists and electron beam resists they are rarely used in fabrication [53, 54]. For these reasons the thiosulfate-sulfite based plating bath was used to produce the nanostructures found in Figure 3.4 below.

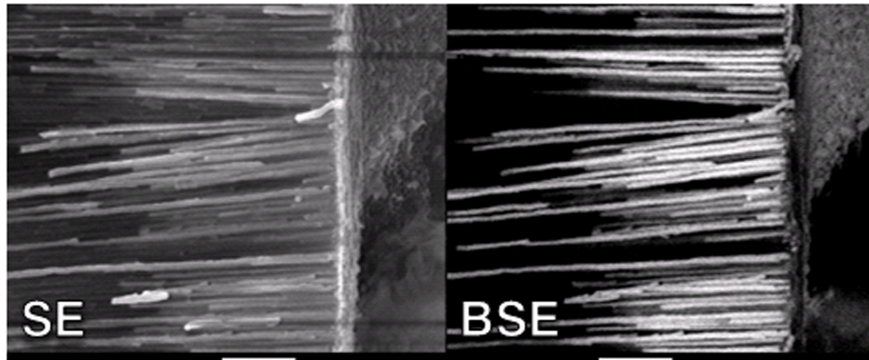


FIGURE 3.4: *left* secondary electron SEM image of AuNW-embedded AAO templates; *right* backscattered electron SEM image of the same area.

Maintaining the same plating conditions (i.e. J) and adjusting to a shorter timescale allowed for synthesis of controlled arrays of Au catalyst segments within the AAO to assist in the vapor-liquid-solid (VLS) growth of silicon nanowires (SiNW).

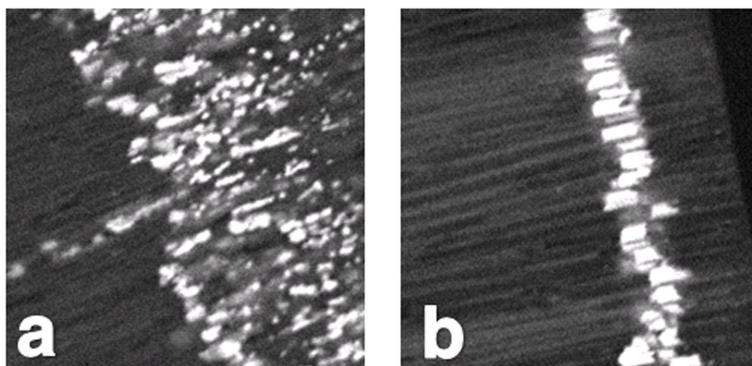


FIGURE 3.5: **a** Au catalyst segments grown with a high current density J , **b** Au catalyst segments grown with a proper current density, leading to higher uniformity

3.6 AAO-assisted Silicon Nanowire Growth

The past decade has seen many advancements in the field of nanoelectronics and one-dimensional and one-dimensional like transport, specifically in carbon nanotubes [55] and silicon nanowires (SiNW) [56]. Semiconductor nanowires are of fundamental interest due to their low dimensionality and relatively low production costs, both of which are significant challenges facing the planar semiconductor community [56]. Nanowires are formed by the vapor-liquid-solid mechanism (VLS) by which a liquid metal serves as an energetically favorable adsorption and nucleation site for a gaseous precursor, which in turn supersaturates the metal droplet and precipitates out in the form of a one-dimensional structure.

Similar to the approaches used in colloidal growth of SiNW, template-assisted growth of SiNW requires short Au segments to serve as catalyst for the VLS mechanism [57, 58]. The general principle involves suspending the Au segment within the template to ensure a pore-limited size (diameter) of the nanowire. This is accomplished by performing separate electroplating steps described in section

3.5; the first using a Ag plating bath ($J = 1 \text{ mA/cm}^2$ for 2 hrs), as a support layer, then a second electroplating step ($J = 1 \text{ mA/cm}^2$ for 15-30 min) to plate the Au catalyst segment. The thermally-evaporated silver electrode and nanowire support segment were selectively etched in diluted 8M HNO_3 acid, resulting in uniform Au catalyst segments as seen in Figs. 3.5 and 3.6a.

Silicon nanowires (SiNW) were grown via CVD within PZTNT-embedded AAO (Fig. 3.6) using the methods developed by Lew [57, 58] described earlier. The preparation and growth parameters are as follows:

1. Using tweezers, break a small piece of the Au catalyst-embedded, PZTNT-embedded AAO (as synthesized using parameters in sections 3.4 and 3.5) and place onto a quartz boat
2. Load the boat into the quartz reactor tube at the predetermined distance (this was a calibrated distance using an external thermocouple to ensure the temperature was reading correctly within the hot zone of the furnace)
3. Ramp the furnace reactor to desired operation temperature (500 - 530°C) under a base pressure of 13 Torr, as controlled by a homemade pressure controller/Barotron
4. Ensure that step 4 is completed under the direct flow of H_2 [25 - 100 standard cubic centimeters per minute (sccm)]
5. Once furnace stabilizes at a reaction temperature above the eutectic (363°C [59]) introduce the flow of the gaseous silane (*Voltaix* 10%- SiH_4 ; balance H_2) precursor at a flow rate commensurate with desired partial pressure of silane. *Note: a silane partial pressure of 0.65 Torr produced the best results, i.e. 50 sccm SiH_4 :50 sccm H_2*
6. Stop the furnace after the reaction time (typically 1 hour, to ensure penetration of gas into the pores) and cool the reaction tube under hydrogen flow at the base pressure (13 Torr)
7. Remove sample

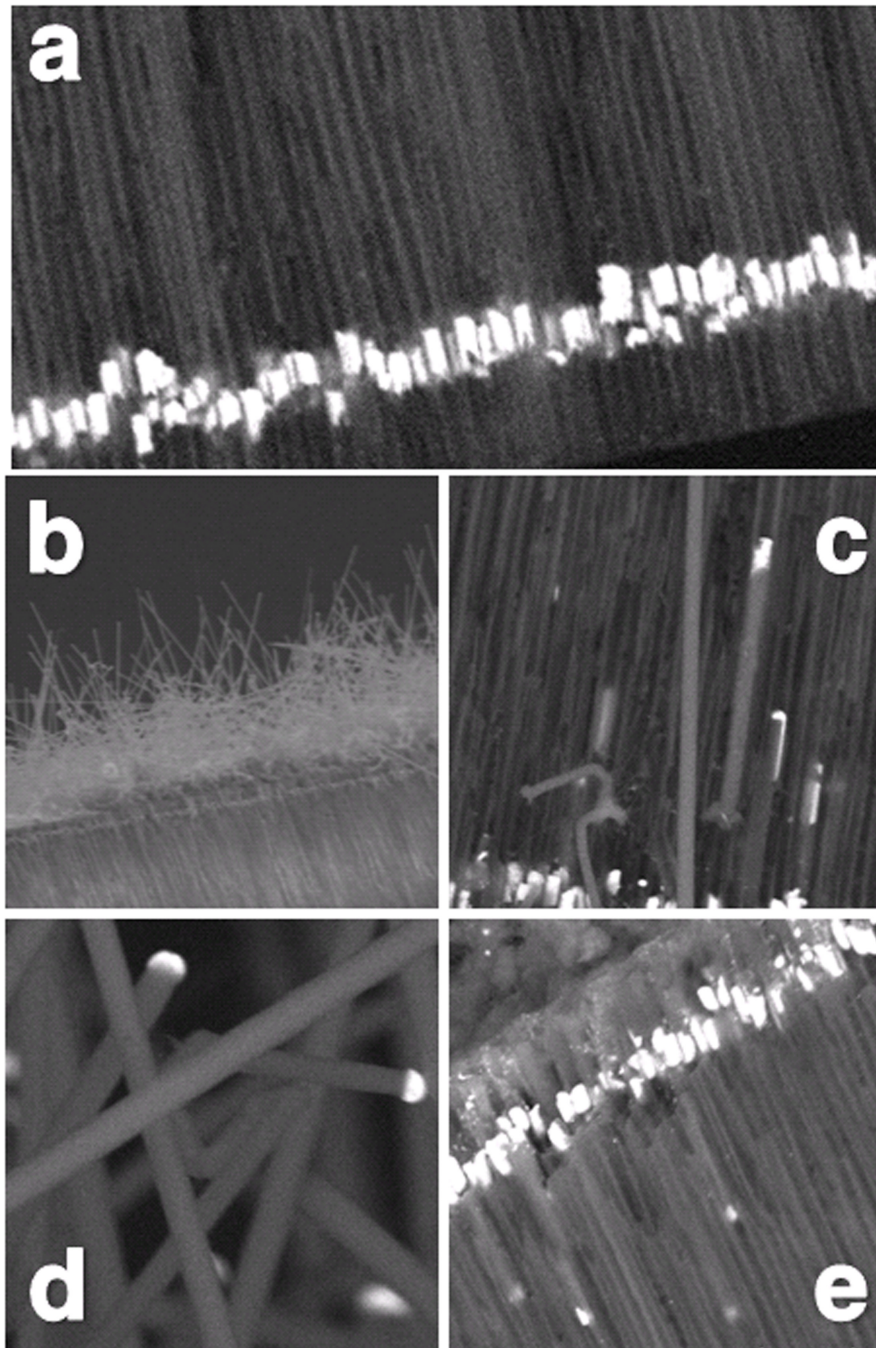


FIGURE 3.6: **a** Au catalyst segments within AAO, **b** SEM cross section image of AAO template after growth in CVD, showing wires extending from template surface, **c** cross section SEM image of SiNW grown in PZTNT-embedded AAO, **d** SEM image of SiNW grown out of the AAO surface, showing distinct Au-catalyst ends *bright contrast*, **e** cross section SEM image of SiNW grown in PZTNT-embedded AAO

Figure 3.7 shows energy dispersive spectroscopy (EDS) and SE/BSE images of SiNW-PZT core-shell nanowires within AAO. Present are the three elements comprising PZT (Pb, Zr, Ti), along with Si and the Al present from the AAO. The Si present is due to the presence of nanowires, as the EDS was collected directly from the template and not while dispersed on a substrate. Brighter areas of contrast within the BSE images represent the Au catalyst segments.

After the wires have been grown in CVD, they are prepared for test structure fabrication by being placed into a microcentrifuge tube and immersed in 6M NaOH to selectively etch the AAO from the Si-PZT nanowires. Briefly, a couple key suggestions:

1. Place only a small amount of grown template into the NaOH bath. Aluminum based salts can form during the selective etching and too much template will result in these salts not dissolving completely, leaving the entire nanowire solution very dirty.
2. Break the small AAO embedded pieces into many, many tiny pieces. Every surface of the AAO placed into the CVD reactor has been covered in amorphous silicon. Breaking the piece exposes bare alumina, which etches at a far faster rate than silicon surfaces. In fact, I probably still have unbroken pieces still trying to etch today.
3. The dissolving process should be completed in a 12 - 24 hour timeframe. This will require a 4x rinse and centrifuge cycle in DI water to reduce the pH of the etch solution. After the pH is lowered the samples are swapped from DI with either ethanol, isopropyl alcohol, or hexane, to be dispersed onto a substrate.

After completing the steps outline above, individual Si-PZT core-shell nanowires may be dispersed onto a substrate, as shown in Fig. 3.8. As demonstrated in Fig. 3.6, the process outline for the synthesis of SiNW-PZT, in its current form, is a low yield process. This is evident when closely observing the freestanding species in Figs. 3.8d and 3.8e where clearly defined hollow and filled sections of the nanotube are both visible (Figs. 3.8a-b). The problem most likely exists within the half reactions [56]:

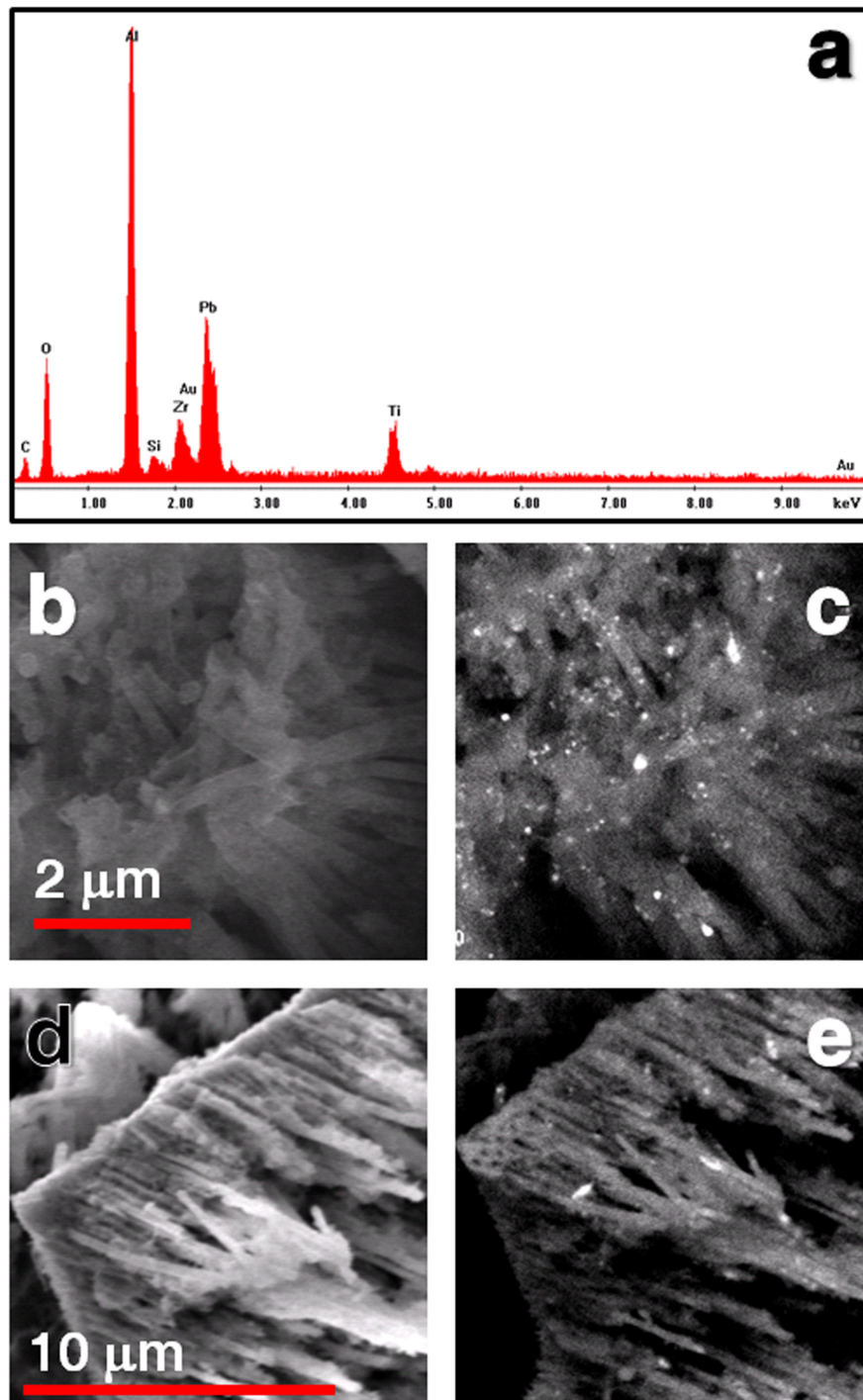


FIGURE 3.7: **a** EDS of Si-PZT nanowires embedded in AAO, **b-c** SE and BSE SEM images of partially etched Si-PZT nanowire arrays in AAO (*top view*), **d-e** SE and BSE SEM images of partially etched Si-PZT nanowire arrays in AAO (*side view*)

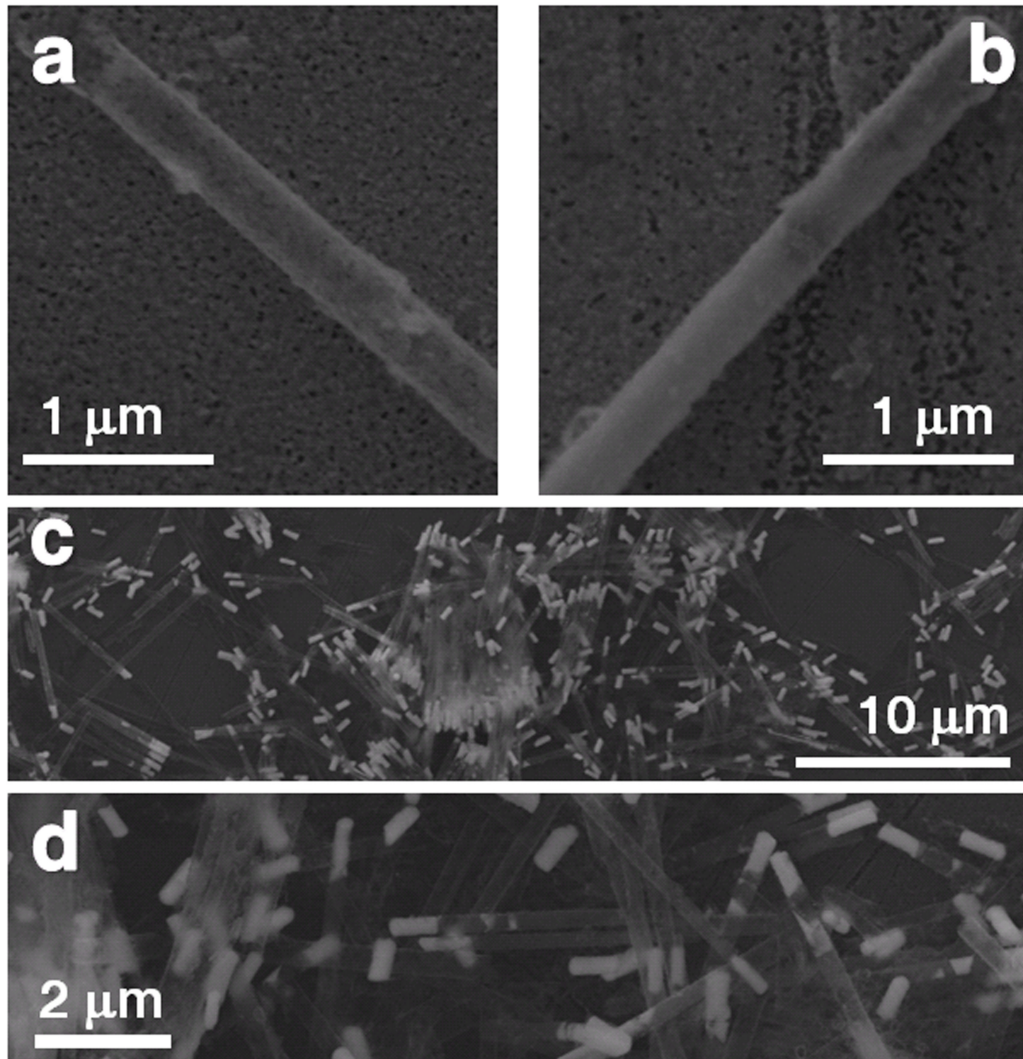
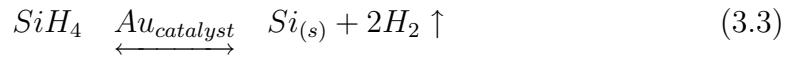


FIGURE 3.8: SEM image of freestanding **a** hollow PZTNT and **b** Si-PZT nanowires dispersed on a silicon-SiO₂ substrate, **d-e** SEM images dispersed Si-PZT nanowire species

Equations 3.3 and 3.4 represent the reactions for catalyzed (heterogeneous growth) and pyrolytic (homogenous decomposition) growth, respectively. Though outside the scope of this study, it is apparent that the gaseous SiH₄ requires the

proper kinetics (flow), partial pressure, and time to produce higher crystalline yield. Another factor in increasing the yield involves very careful control of the nanowire Au catalyst segment; a longer segment necessarily involves a greater volume which must be supersaturated in order to precipitate a silicon nanowire.

3.7 Structural Characterization

Structural characterizations of the coaxial nanowires were performed using X-ray diffraction (XRD) and Raman scattering spectroscopy, as shown in Fig. 3.9. Plotted in Fig. 3.9a is the XRD collected from PZT nanotubes embedded within the AAO, possessing reflections from tetragonal perovskite PZT grown via sol-gel [60]; the other observed peaks are from the AAO template [61]. It should be noted that the perovskite phase is present despite its small grain size (≈ 5 nm). This does not preclude the existence of a surface pyrochlore phase, previously shown as a 10% perovskite/pyrochlore phase ratio in identically prepared sol-gel PZT nanotubes with nanocrystalline grains [62]. A representative Raman spectrum (Fig. 3.9b) (Renishaw 1000, 514.5-nm excitation) collected from an individual PZT nanoshell contains peaks near 205, 275, 325, 594, and 737 cm^{-1} ; these energies correspond to the irreps (phonon modes) $E(2\text{TO})$, $E+B_1$, $A_1(2\text{TO})$, $A_1(3\text{TO})$, and $A_1(3\text{LO})$ of perovskite PZT of the specified composition [63], respectively.

Nanowire diameters and thicknesses were obtained by atomic force microscopy (Asylum Research MFP-3D) and transmission electron microscopy (TEM, JEOL 2100), respectively. TEM (Fig. 3.10a); selected area electron diffraction (SAED) (inset) and scanning electron microscopy (SEM) (Fig. fig:TEMSEMNB) images confirm structures are $\approx 5\mu\text{m}$ long, 50 nm in diameter and 7 nm in shell thickness, with an average grain size of ≈ 5 nm. The polycrystalline rings correspond with the 110, 111, 210, and 211 reflections of tetragonal PZT, respectively [64]. Shown in Fig. 3.10b is an SEM image (*false color*) of an electrically-contacted coaxial nanowire, prior to proximal probe characterization. Structures ranging from 50-240 nm in diameter, 3-10 μm long, and 7-30 nm in shell thickness (ζ) were prepared in this manner.

question:
what
does the
Scherer
formula
predict?

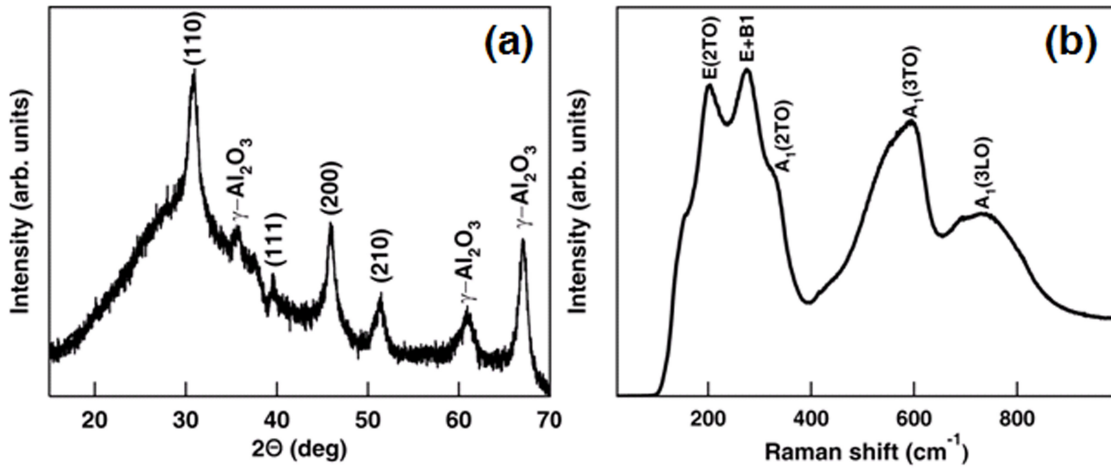


FIGURE 3.9: (a), X-ray diffraction of nanotubes within the AAO template. Indexed peaks are of tetragonal perovskite; all remaining indices are assigned to the AAO. (b), Raman spectrum of an individual 100 nm PZT nanotube in which the observed modes of tetragonal perovskite are denoted.

3.8 Electron beam lithography

The purpose of the synthesis methods described in sections 3.5 and 3.6 was to create an integrated nanostructure with a conductive inner electrode material. This section will outline the fabrication steps necessary to create an electrically-addressable test structure. Electron beam lithography (EBL) has been used since the sixties [65] to write submicron patterns within an electron sensitive resist. The shorter wavelengths of electrons inherently makes nanometer scale patterning easier than by optical lithographic methods. However, the semiconductor industry has universally used optical lithography due to its speed, as single electron patterning is (almost) prohibitively slow for industry purposes. As node dimensions have decreased, various techniques have been employed to enhance lithographic resolution down to sub-30 nm, including but not limited to phase shifting masks, extreme ultraviolet lithography, various fluoride-based excimer light sources, and liquid immersion [66]. The optical lithography vs. EBL debate is great for industry, however in an academic experimental laboratory setting involving registration patterning to nanowires, EBL is the clear choice.

The general approach to contacting nanowires was modified and adapted from

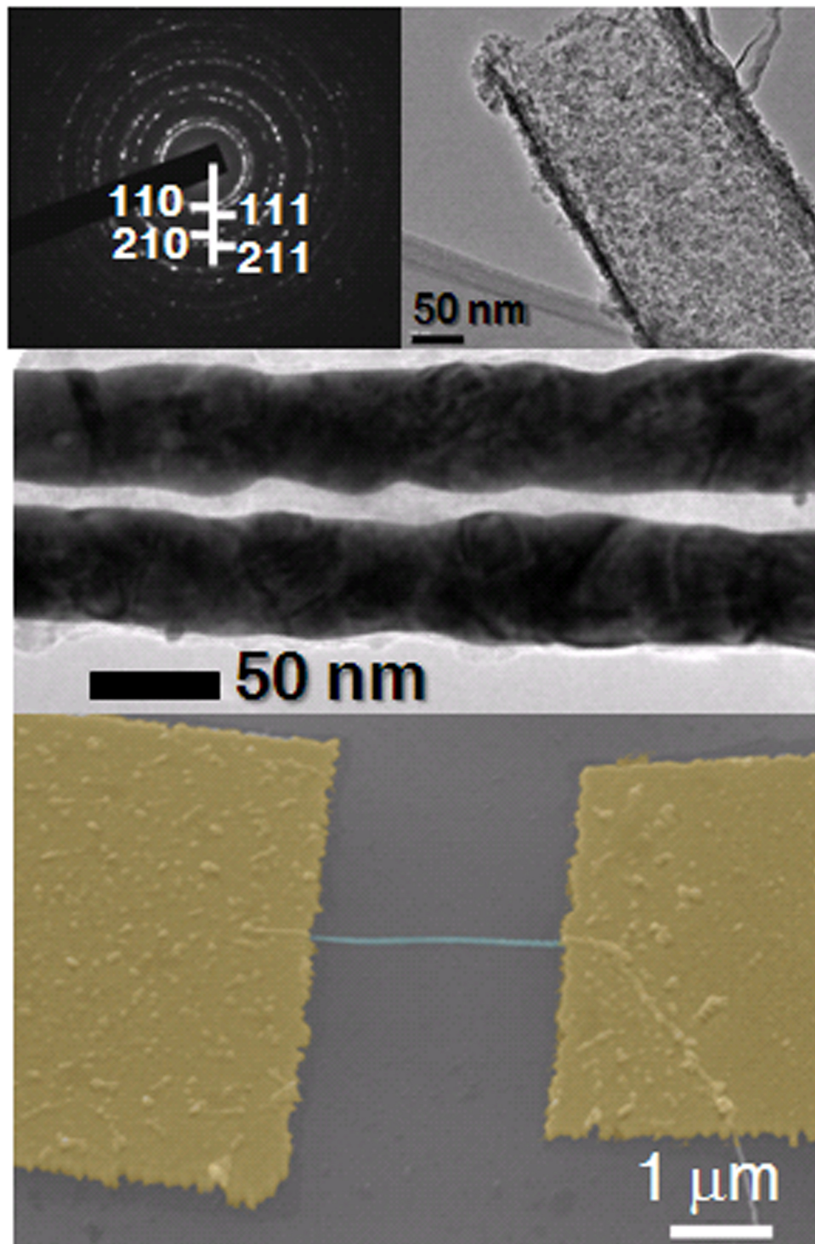


FIGURE 3.10: (a), TEM image of two 50 nm diameter Au-PZT core-shell nanowires, scalebar = 50 nm. Upper inset, electron diffraction of a bundle of Au-PZT nanowires. Lower inset, empty 200 nm PZT nanotube, scalebar = 50 nm. (b), (false color) SEM image of a single nanowire, scalebar = 1 μm .

similar approaches used in fabricating electrical contacts in other one-dimensional-like systems [55, 56, 67]. The entire contacting process follows these steps:

1. Take a blank SiO_2 -covered wafer and spincoat 100 K (Microchem) electron beam resist at 5000 rpm for 30 seconds, then bake for 5 minutes; repeat

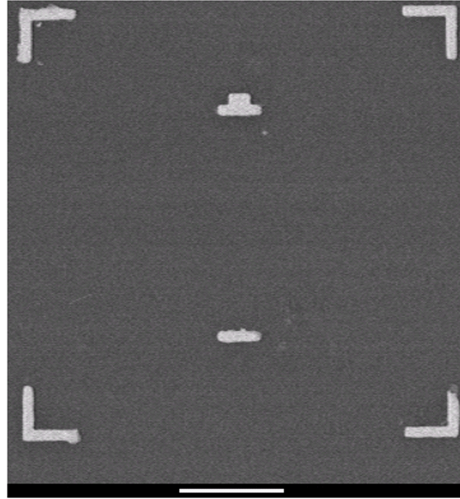


FIGURE 3.11: typical alignment pattern used in the EBL patterning of nanowires, prior to nanowire dispersion; scalebar = 10 μm .

- spincoating of 950 K (Microchem) resist for 30 seconds and bake for 30 minutes
2. Using the Nano Pattern Generation System (NPGS; Nabyty Inc), run array of alignment markers over the entire wafer with a high beam current (250 pA - 1 nA)
 3. Develop the patterns in a 3:1 mixture of 2-propanol:4-methyl-2-pentanone(MIBK) for 70 seconds.
 4. Evaporate metallic bilayer [10 nm Cr (adhesion) - 200 nm Au] onto patterned wafer
 5. Place wafer into acetone for at least 3 hours to remove residual resist, as shown in Fig. 3.11
 6. Take core-shell nanowire suspensions made as described in section 3.6 and disperse onto a prepatterned substrate (step 1; Fig. 3.11)
 7. Collect SEM images of the dispersed nanowire species in the areas found in 3.11
 8. Repeat step 1

9. Import SEM images from step 7 and create new CAD patterns registered to the nanowire ends, using the original CAD patterns from step 2 as the origin for alignment.
10. Repeat steps 2-3 ($I = 50$ pa; $dose = 250\mu\text{C}/\text{cm}^2$), then place sample into etchant [68] to selectively remove the FE shell from the core material, then repeat steps 4-5 to directly contact the inner nanowire core.
11. *For AFM measurements:* Place chip of contacted nanostructures into a chip carrier, then manually wirebond

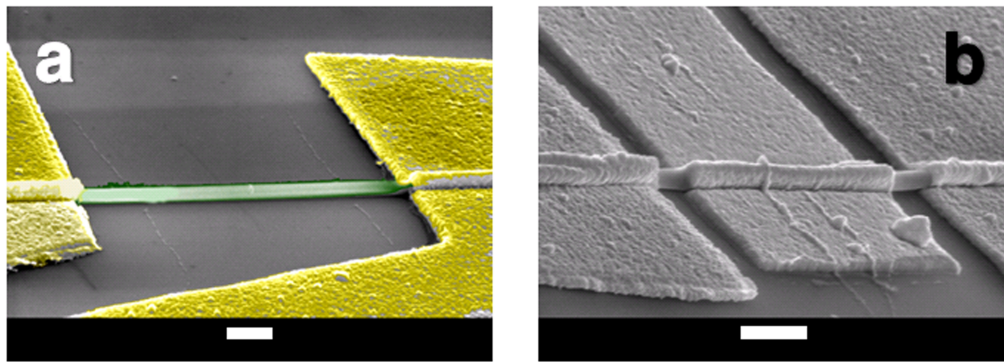


FIGURE 3.12: **a** a SiNW-PZT core-shell nanowire contacted using EBL, **b** a two-step EBL contact process resulting in a third (gate) electrode; both scalebars = $1\ \mu\text{m}$.

Figure 3.12 show SEM images of contacted SiNW-PZT core-shell nanowire test structure **a** and gated test structure **b** fabricated using the methods outlined above 3.8. These test structures shown in 3.12a form the basis for the studies covered in Chapters 4, 5, and 7. The gated test structures shown in 3.12b form the base for the studies covered in Chapters 6 and 7. Focused Ion Beam (FIB), electron-assisted deposition of Pt also served as a means to directly contact nanostructures with gate electrodes. The majority of the electrodes used during the following chapters were performed using EBL. A detailed review of the FIB process may be found here [69]. A description of the FIB contacting process will be found in Chapter 7.

Chapter 4

Piezoresponse through a Ferroelectric Nanotube Wall

Piezoresponse force microscopy (PFM) is a modified scan probe technique utilizing a lock-in amplifier to apply a bias to a conductive cantilever tip in contact with the material surface, inducing a piezoelectric deflection via the converse piezoelectric effect. This technique can be used to image FE domain states or manipulate the FE state in scanning mode, or collect localized FE piezoelectric hysteresis in a static probe setup. Chapter 4 concentrates on the experimental setup and discussion of PFM scan mode operation in identifying the FE state of an individual nanowire test structures [70].

4.1 Scanning Probe Microscopy - Basics

Scanning probe microscopy (SPM) is a local characterization technique based on a principle approximation to Hooke's law. Briefly, as an atomically-sharp tip mounted on a cantilever approaches the sample surface (Figure 4.1a) the forces normally associated with attractive and repulsive regimes (Figure 4.1b) are observed. As the cantilever begins to bend, an incident laser signal is deflected and then read by a photodiode, which in turn creates a feedback loop by adjusting

either the sample height or cantilever height to maintain a constant cantilever deflection setpoint. The voltages necessary to adjust the height within the feedback loop may then be used to obtain topographic information of the sample surface.

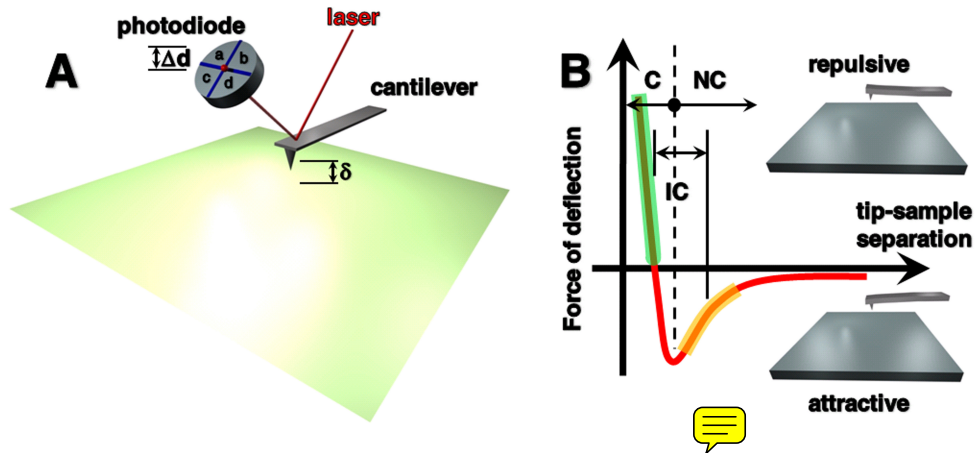


FIGURE 4.1: **a** Illustration of the operating principle of SPM; the deflection of the cantilever δ is read by a 4-quadrant photodiode Δd creating a feedback which yields topographic information, **b** The forces associated with the tip-sample interactions during use of SPM.

4.2 Piezoresponse Force Microscopy

Since its initial discovery by Binnig and Gerber in 1986 [71] atomic force microscopy has played a pivotal role in the growth and understanding of nanoscale systems and their rich physics. Since then, many modified techniques have been developed [72, 73] to study localized physical, chemical, and biological phenomena. This thesis focused on a single modified AFM or SPM technique called Piezoresponse Force Microscopy (PFM). This section will cover the basic operating principles of the technique as context for the remaining chapters; more detailed coverage of its operation and use can be found in a terrific review by Sergei Kalinin [74].

PFM is a contact-based, modified scan probe technique implementing a lock-in amplifier to collect an electrically-induced deflection of the sample surface. Here an alternating current (AC) voltage is applied directly from a conductive cantilever tip in direct contact with the sample surface, thus creating a piezoelectric deformation of the sample due to the converse piezoelectric effect. The deflection of

the cantilever is then read by the photodiode, similar to topographic operation described in the previous section. The difference here is that the lock-in is now part of the feedback loop, and can read the piezoelectric deflection amplitude and phase signals, each of which represents the magnitude and orientation of the collected signal, respectively.

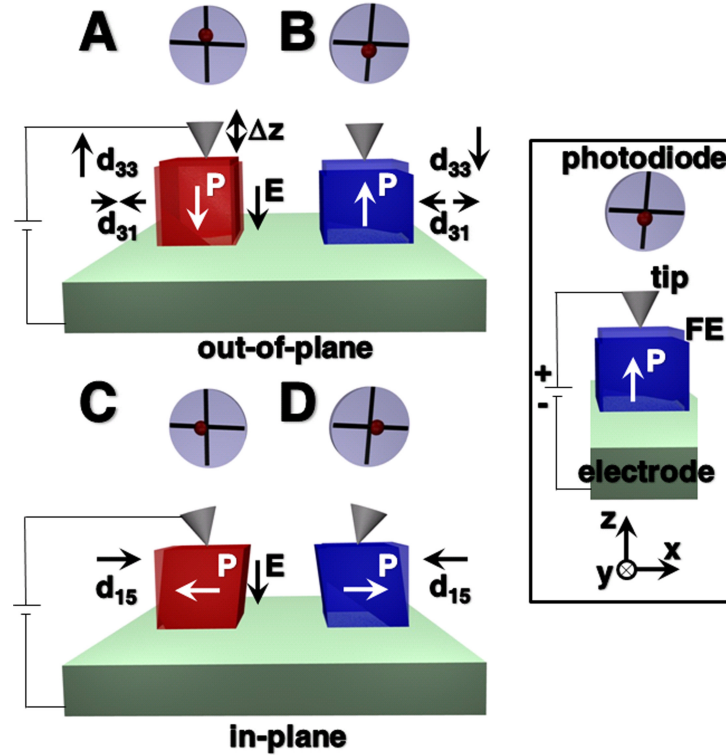


FIGURE 4.2: Schematics of the converse piezoelectric effect on FE particles on a surface, with **a** and **b** representing positively and negatively poled normal FE polarizations and **c** and **d** positively and negatively poled lateral polarizations, respectively. **Legend** shows a typical experimental configuration.

PFM has become the standard by which phenomena in nanoscale ferroelectrics are measured locally, with numerous published results of thin films [7, 8, 20, 27, 75, 76, 77, 78] and ferroelectric nanostructures [41, 42, 46, 47, 62, 63, 79, 80, 81, 82, 83, 84] alike. There are generally two modes of operating PFM to collect ferroelectric piezoelectric-based information:

1. **PFM scan mode:** As described in the paragraph above Fig. 4.2
2. **PFM static hysteresis mode:** A static, proximal probe technique applying a slowly-varying triangle wave to the substrate electrode (which during

scan mode is grounded) while a higher frequency AC signal is applied to the conductive cantilever tip. The resulting hysteresis is collected either a measure of ferroelectric piezoelectric d_{33} coefficient, in the loop shape shown in Fig. 2.2, or in the form of piezoelectric deflection amplitude as a butterfly shape loop

In the case of non-planar ferroelectric nanostructures, both PFM scanning and hysteresis has been performed of solid ferroelectric nanowires [83, 84] and nanoislands [46, 81], however of hollow ferroelectric nanotubes [41, 42, 62, 79, 80] only static ferroelectric have been collected to date. Due to the detail synthesis and fabrication approaches outline in Chapter 3 this study offers the first structure to allow for interrogation of ferroelectric piezoelectric properties in both scanning and static proximal hysteresis PFM modes.

Nanoscale ferroelectrics (FE) exhibit size-dependent phenomena [6, 21, 22, 77, 81, 84, 85, 86, 87, 88] not observed in bulk, generating interest in their physics and applications. Among recent studies are theoretical and proximal probe experimental investigations in which unusual dipole ordering [81, 85], size and/or shape-driven ferroelectric phase transitions and transition temperatures [22, 86], and enhanced axial polarizations [86, 87] were reported. The stabilizing effect of molecular adsorbates [22] and of surface-induced strains [84] in reinforcing out-of-plane polarizations against depolarizing fields have been observed in films and in high aspect ratio, large surface-to-volume nanostructures alike [21, 22, 77, 88].

Template-assisted fabrication techniques using materials such as anodic aluminum oxide (AAO) have expanded synthetic options for experimental realization of low-dimensional FE in arrays of nanotubes [40, 41], nanowires [22, 63], nanoislands [46] and nanodots [32], thereby permitting study of finite-size and shape effects, significant for application in higher-density non-volatile memories. Investigations of size effects in FE thin films have employed ~~piezoresponse force microscopy~~ (PFM) to observe the local FE response as induced via a conductive tip. Here, Au-Pb($Zr_{0.52}Ti_{0.48}$)O₃ (PZT) coaxial cylindrical nanowires (Fig.3.10) are used to investigate the stability and switching of ferroelectric domains oriented along the finite, shell-normal direction.

Proximal probe measurements were collected by scanning the topography of the nanowire (Fig. 4.3(a)), after which the tip was repositioned onto the nanowire surface and held in constant deflection feedback, where a slowly varying bias was applied to the nanowire core ($\pm 18 V_{pp}$, .05 Hz) while an ac bias was simultaneously applied ($3 V_{pp}$, 4 kHz) to the cantilever tip (Fig. 4.3(b)), thus enabling the collection of ferroelectric hysteresis loops (Fig. 4.3(c)). The observed positive vertical offsets, commonly attributed to the imprint behavior of a non-switchable dead layer [89], result from surface tension-induced strain gradients in the nanoshells, similar to graded ferroics [90, 91, 92]. Larger radius nanoshells hysteresis exhibited a negligible shift, while those of more extreme curvature displayed large offsets.

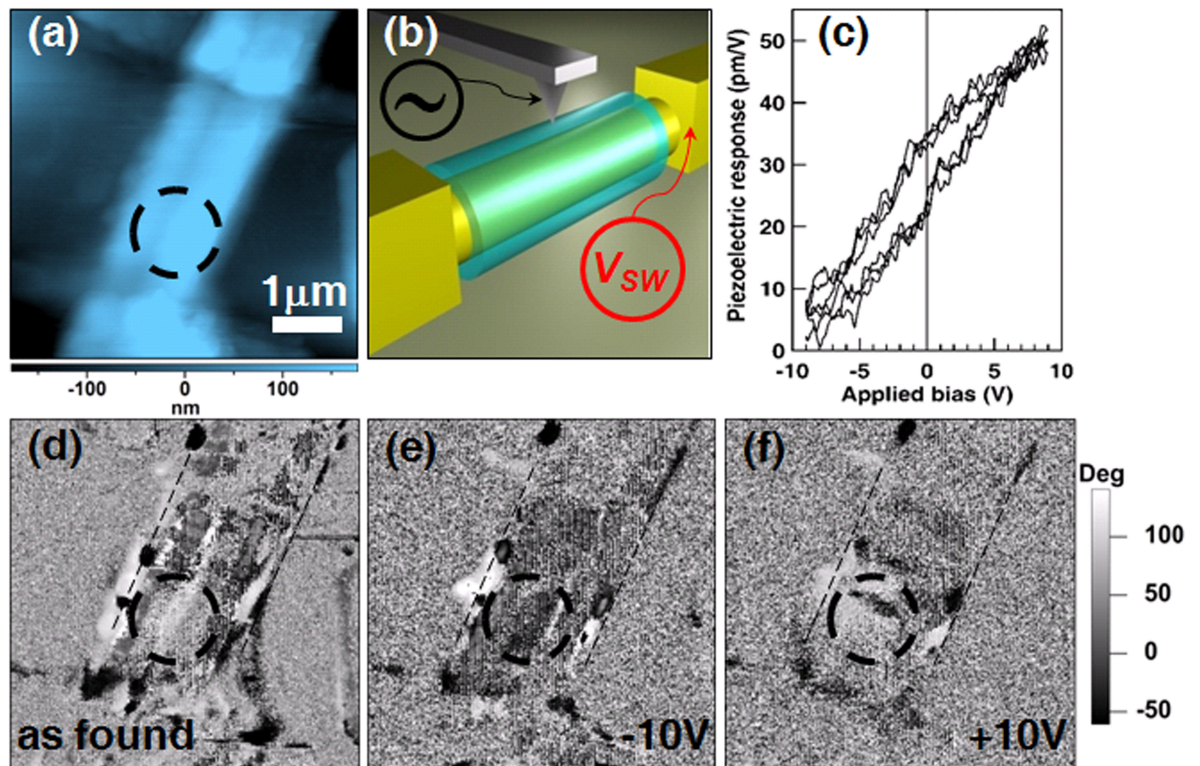


FIGURE 4.3: (a) (false color) height map of a 100 nm Au-PZT coaxial nanowire. (b) experimental scheme for collecting (c) ferroelectric piezoelectric hysteresis and (d-f) plane-normal piezoresponse phase contrast maps. (d) represents the “as found” state with (e) and (f) revealing written negative and positive ferroelectric domains, respectively (dashed circles).

The local FE response across the smallest (radial) dimension of PZT nanoshells was collected by PFM (Asylum Research MFP-3D). Images were obtained using

a Ti-Pt coated tip (Olympus Electrilever, $k \approx 2$ N/m, tip radius ≈ 15 nm) biased at 2 V while driven at 280 kHz, away from the cantilever resonance (77 kHz), as to minimize topographic contributions. During PFM imaging, the Au nanowire core was held at ground. The height map of a representative 100 nm diameter nanowire is shown in Fig. 4.3(a). The nanowire diameter appears larger due to tip-nanowire convolution effect, similar to other PFM studies of FE nanowires [83, 93]. Successive PFM phase contrast maps (range $+150^\circ - -50^\circ$) of the nanoshell polarization as-found (Fig. 4.3(d)), and following application of -10 V (Fig. 4.3(e)) and +10 V (Fig. 4.3(f)) while the tip was scanned over a region denoted by the dashed circles indicate a shell-outward normal polarization component in this region initially, with demonstrable reversible switching, respectively. Switching events were produced in deflection feedback point mode for a duration of 10-12 seconds. Following a writing event, the local phase signal associated with each written and switched domain was observed to be stable for the timescale investigated. No detectable change in contrast could be discerned among five successive scans following a writing event (70 min.). A study of the long-term stability of written and switched domains, however, merits further study.

The image data in Figs. 4.3(d)-(f) raise interesting questions regarding the origin and stability of polarizations oriented along the finite-thickness dimension in ultrathin films and nanostructures. Remarkably, an outward shell-normal (as opposed to in-plane) polarization is seen over some portions of the nanoshells in their as-found state, consistent with the orientation observed within ultrathin ferroelectrics possessing chemisorbed M (M = transition metal)-OH [21]. The effective screening length of such adsorbates can be even shorter than those for metallic electrodes [88], thus mitigating the effect of the depolarizing fields that typically suppress the response in ultrathin films situated between two electrodes [6]. Density function theory calculations have been previously reported [22] to preserve tetragonality in BTO lattice within nanowires downwards of 3 nm in diameter. Fourier transform infrared (FTIR) absorption spectra (Fig. 4.4) were collected (Varian Excalibur FTS-3000) using a diamond single reflection attenuated total reflectance prism. Nanowire suspensions were dried (150°C) and exchanged repeatedly in chloroform (BDH1109) to ensure the absence of free hydroxyl species. The suspension was evaporated onto the prism surface before

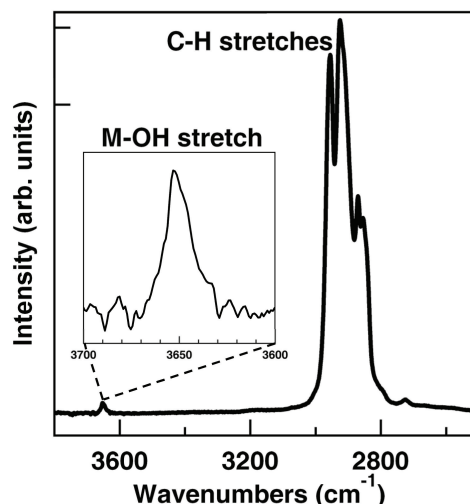



FIGURE 4.4: FTIR spectrum of 100 nm PZT nanotubes. Inset shows an enlarged view of the 3650 cm^{-1} peak, resulting from surface terminated hydroxyl species. The large peak at 2925 cm^{-1} corresponds to C-H stretching modes.

accumulating spectra (128 scans, 2 cm^{-1} resolution). The estimated peak at $\approx 3650\text{ cm}^{-1}$ is assigned to M-OH ($M = \text{Zr, Ti}$) stretching modes [94], indicative of surface-terminated chemisorbed hydroxyl species along the ferroelectric nanoshell, not surprising given the **alcohol**-based sol-gel preparation outlined in section 3.4. We note that no discernable stretching modes for either **Pb-O or surface O-H were observed, consistent with their reduced thermodynamic stability** [21]. The large feature estimated at $\approx 2925\text{ cm}^{-1}$ results from C-H stretching modes of residual organics from the dried nanowire suspension. These adsorbates have been previously predicted to produce upwards and downwards polarization states within ultrathin ferroelectric thin films, respectively. 

Note that the adsorbed species can play a role in the observed component of outward normal polarization and the vertical offset in the observed hysteresis in the as-found shell. The precise mechanism(s) influencing the domain stability after switching events (Figs. 4.3(e)-(f)), however, are not clear. The multitude of domain states observed throughout the length of the nanowire result from competing elastic and depolarizing effects within polycrystalline grains [95] (Fig.3.10(a) inset), creating mixed 90° (gray or no contrast) and 180° (white/black contrast) domains. The values of ΔG (the reaction energy per adsorbate) for species relevant to the present experiments are in the range of $-0.2 < \Delta G < 1.95\text{ eV}$ at 300 K [21].

While several possible adsorbate and adatom species, and/or oxygen vacancies may participate in screening, we propose that the locally intense electric field under the tip, produced by the application of the switching voltage ($\pm 3 V_{pp}$), is sufficiently large for these and other adsorbates to overcome the energetic barriers necessary for desorption and migration, and also for migration of vacancies toward or away from the surface of the written domain. Attempts to image the lateral piezoresponse (along the fast scan direction; minimal loading force) damaged the PZT nanoshell surface, making a full domain map of the nanoshell infeasible. The switching observed in Figs. 4.3(e)-(f), however, unambiguously show a shell-normal (or out-of-plane) component of polarization.

In conclusion, the ferroelectric response of template-fabricated Au-PZT cylindrical nanowires has been measured using PFM across the finite, radial dimension. Stable, switchable shell-normal oriented polar components are observed, as demonstrated by hysteresis and imaging of a switched domain state. The outward shell-normal components in the as-found nanoshell can be explained by the presence of M-OH adsorbates, consistent with previous work of domain stability in thin films [20, 21] and nanowires [22]. These principles and methods should stimulate interest and develop new applications in low-dimensional systems of ferroelectrics and multiferroics.

Chapter 5

Finite Curvature-Mediated Ferroelectricity

This section will review and discuss experimental evidence for finite-curvature, surface-tension based stabilization of FE properties along the finite-thickness direction of individual nanostructures. The findings presented in this section will be corroborated with numerical calculations incorporating a modified Landau stiffness into the free energy expansion, with comparisons given between nonlinearly coupled surface tension-induced stresses and planar, stress-free thin films [96].

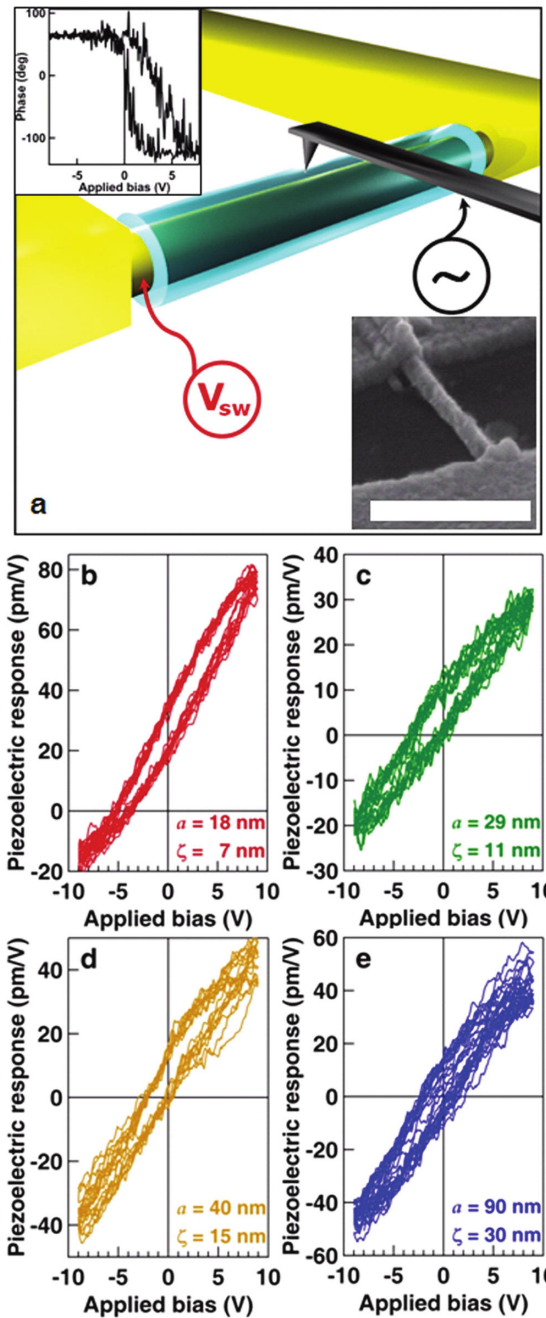
Ferroelectric (FE) thin films and nanostructures continue to attract intense interest [13, 16, 18, 21, 25] for their enormous potential as highly versatile nonvolatile memory elements [18, 22, 77, 78], for THz emission and thermocaloric cooling [97], and for their finite size-dependent physical phenomena [16, 21, 22, 25, 85, 98]. The stability of the FE phase in ultra-thin films and nanostructures is limited by the relative contribution of the depolarizing field to the free energy, arising from incomplete screening of surface polarization charge. Extreme reduction in film thicknesses is typically accompanied by a concomitant decrease in FE polarization P and phase transition temperature T_C , reflecting a critical size for ferroelectricity. In recent years efforts to develop strategies to stabilize switchable FE states in few-monolayer films via heteroepitaxial strain [13, 18, 77], surface chemical environment [21, 22] and selection of FE-metal interfaces [99] hold great promise

for addressing finite-size limitations, further demonstrating the significance of the surface and interfacial boundary conditions.

The deleterious effect of the depolarizing field is equally severe for FE nanoparticles, but FE nanoparticles can exhibit unexpected and new physical phenomena not found in bulk. For example, toroidal FE ordering [81, 85] and enhancements in axially-oriented polarization P_z and in T_C in FE nanotubes and nanowires owing to electrostrictive coupling of azimuthal stresses [87, 98] have been reported, suggesting new possibilities for high-density encoding of information. Experimental evidence indicates that polarizations oriented either parallel [83] or perpendicular [22, 23, 83] to the FE oxide nanowire axes are stable and switchable.

Here, evidence for suppression of the finite-size reduction of FE polarizations in ultra-thin and extremely curved nano-shells with polarizations oriented along shell inward and outward normals is presented. Significantly it is demonstrated that such curvature can alter the evolution of T_C , providing a new means of circumventing finite-size limitations. Local FE switching and piezoelectric responses within individual, coaxial cylindrical oxide perovskite ($\text{PbZr}_{0.52}\text{Ti}_{0.48}\text{O}_3$, PZT) nano-shells each encasing a noble-metal (Au) core [70] were probed using piezoelectric force microscopy (PFM) [75] collected in atmosphere at room temperature (Fig. 5.1(a)). Measurements collected from a range of thicknesses and radii indicate remarkably large responses compared to their planar counterparts of identical composition. Significantly, no systematic decrease in the FE response is seen for decreasing shell thickness.

Shown in Figs. 5.1(b)-(e) are traces of the real part of the radial component of the displacement, i.e. local FE piezoelectric hysteresis loops for PZT nano-shells possessing selected values of inner radius a and shell thickness ζ . Figure 5.1(b) (inset) shows the collected variation of cantilever phase during collection of ferroelectric piezoelectric hysteresis loops of an $a = 18$ nm, $\zeta = 7$ nm nano-shell. Fig. 5.2(a) summarizes the d_{33} responses in each nano-shell, comparing to measured responses in planar thin films (dotted grey) and calculated radially-oriented polarizations (dotted blue). Locally-measured effective d_{33} values in the switching in thin film and nanostructured FEs are related to the local FE polarization through the product of the electrostriction coefficient and dielectric susceptibility [2, 75],



Question:
 how do you measure
 a ...

FIGURE 5.1: **a** Illustration of the electrically interfaced nanoshell and measurement, along with an the electron micrograph of a representative nanowire (inset scale bar = 1 μm). **b-e** Measured FE piezoelectric hysteresis loops collected from the oxide perovskite nanoshells, for shell thicknesses ζ and corresponding inner radii a as denoted in the legend. The inset in the upper left of **a** is a plot of the measured phase response of a shell as a function of voltage bias applied across its wall, indicating ferroelectric switching of the shell polarization.

i.e. $d_{33} \approx 2Q_{11}\chi_{33}P$. Calibrated d_{33} values were referenced to measured cantilever stiffnesses obtained from force-distance responses. Significantly, the remanent polarizations observed here do not exhibit a systematic decrease for decreasing values of ζ or outer radius b , in stark contrast to previous reports of a linear reduction for logarithmically decreasing values of film thicknesses [7]. Although our estimate of d_{33} can be expected to be influenced by the non-uniform local electric field in the proximity of the cantilever tip, the measured response for the $\zeta = 7$ nm, $a = 18$ nm shell is nevertheless $\sim 300\%$ that of an epitaxially-grown planar thin film of identical composition that is $\sim 60\%$ thicker (Fig. 5.2(a)) as reported in Ref. [7] and measured using the same method.

The present results are noteworthy in light of the expected linear decrease in piezoelectric response in planar thin films with increasing electric field intensity [100]. Based on estimates of FE domain sizes induced and switched in films by a proximal probe, and noting the geometric confinement of the domain provided by the shell diameter and thickness, we estimate that the smallest volume for which we observe switchable FE domains in these nanoshells to be ~ 6000 nm³. An extrapolation of these experimental results to thinner shells possessing comparable values of ζ/b suggests that switchable and stable radial FE polarizations may be retained in thinner shells, and significantly, those situated within real metal electrodes with finite screening lengths. Reduction in film thickness is typically accompanied by an increase in the coercive field E_C ; this effect in films as thin as ~ 100 nm has been attributed to charge injection through a non-FE layer at the film/electrode interface [101]. Absent *a priori* knowledge of the extent of coverage and the character of molecular adsorbates between the probe tip and the shell surface, we estimate $E_C \approx 3800$ kV/cm for $\zeta = 7$ nm and $b = 25$ nm. While this value is much larger than that for a planar film of identical composition and comparable thickness, ($E_{C,film} \approx 1200$ kV/cm for 8-nm thick film) and the value of the intrinsic thermodynamic limit ($E_{C,thermo} \approx 1200$ kV/cm) [100], both the experimental data and the results of our model calculations exhibit a $E_C \sim \zeta^{-1}$ scaling (Fig. 5.2(b)). The data also show curvature- and shell thickness-dependence of the horizontal and vertical offsets of the hysteresis loops. Plotted in Fig. 5.2(c) and (d) are the center-of-switching (COS) offsets along the piezoresponse and voltage axes, respectively, for selected values of b .

question:
why
normalized?

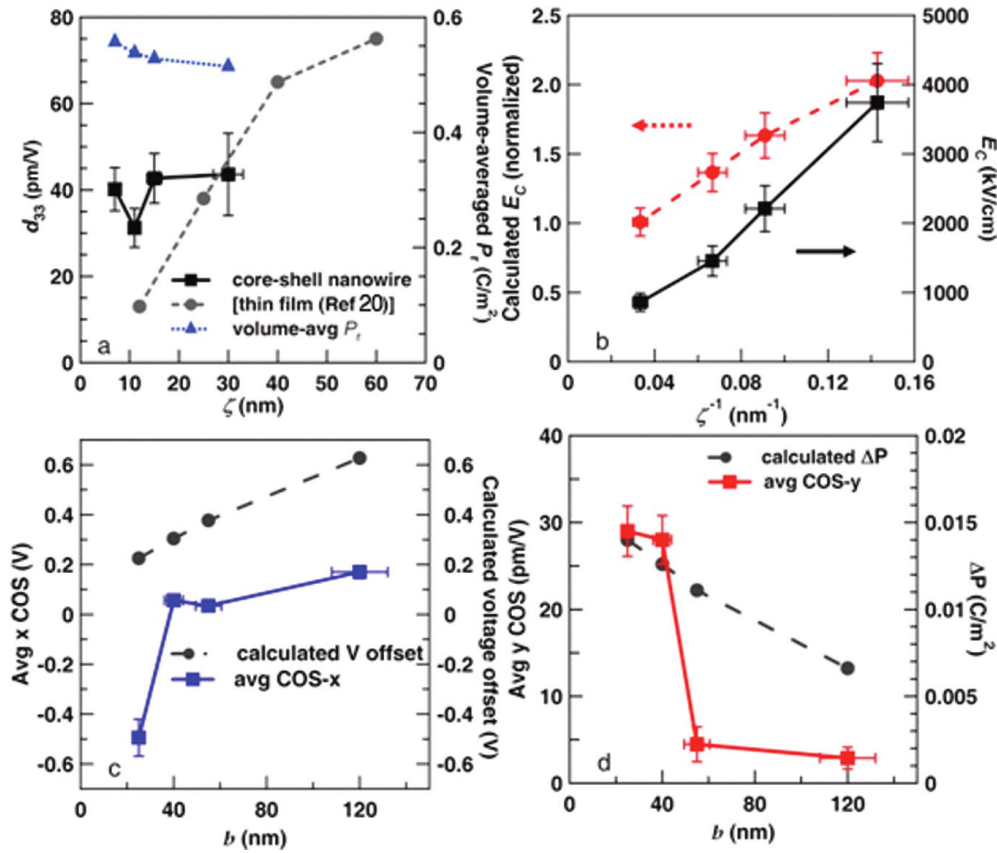


FIGURE 5.2: **a** Measured variation of the FE piezoelectric response with curvature, compared with those for planar thin films of identical composition (NagyAPLcompare), and a scatter plot of the calculated volume-averaged polarization (right axis). **b** Coercive electric field E_C plotted as a function of shell thickness $\zeta = b - a$. **c** Measured vertical center-of-switching (COS) offset values of the FE hysteresis for each nanoshell. **d** Horizontal (voltage) COS offsets (solid squares connected by solid lines), plotted as a function of nanoshell outer radius b . Also shown in **c** and **d**, respectively, are the corresponding calculated polarization and voltage offsets.

What is the origin of the unexpectedly large FE response in these ultra-thin nano-shells along their smallest dimension, and of the offsets of the FE hysteresis loops? Our theoretical analyses of their radially-oriented polarization profiles P_r indicate thermodynamic stability with finite diameter- and shell thickness-dependent enhancements in P_r and T_C . In thin film FE capacitors, an in-plane compressive strain near one or both interfaces, or a strain gradient normal to the plane of the film (e.g. from composition, thermal stresses or bending curvature) couple to P , altering its magnitude, T_C , dielectric tunability, and pyroelectric response [90]. Our model description (Fig. 5.3(b), inset) is that of a coaxial

cylindrical FE capacitor that is comprised of a noble-metal (Au core surrounded by a FE oxide perovskite (PZT) shell of inner and outer radii a and b , respectively, where ρ is defined as the radial position within the shell. With surface tension of $\mu = 5$ N/m [98], the calculation of the radial dependence of the radial and azimuthal stresses and within the shell subject to these surface tensions is of the form of a Lamé problem. Specifically, application of surface boundary conditions $\sigma_{rr}(b) = p_{b\rho}$, $-\sigma_{rr}(a) = p_{a\rho}$, and application of mechanical equilibrium $\partial\sigma_{ij}/\partial x_j = 0$ leads to

$$\sigma_{rr, \varphi\varphi}(r) = \frac{a^2}{b^2 - a^2} \left(1 \mp \frac{b^2}{r^2}\right) p_{a\rho} - \frac{b^2}{b^2 - a^2} \left(1 \mp \frac{a^2}{r^2}\right) p_{b\rho} \quad (5.1)$$

To calculate the radial polarization $P_r(r, a, b)$ and evolution of $T_C(a, b)$ we modify the Landau-Ginzburg formalism, writing the volumetric and surface portions of the Gibbs free energy per unit length, assuming axisymmetric radial polarization $P_r(r)$:

$$G = \int_a^b \left[\frac{A}{2} P_r(r)^2 + \frac{B}{4} P_r(r)^4 + \frac{C}{6} P_r(r)^6 + \frac{1}{2} g (\nabla P_r)^2 - E_d(r) P_r(r) \right] r dr + \frac{D}{2\delta} \int_S P_r^2 dS. \quad (5.2)$$

where $\hat{A}(r) = A - 2Q_{11}\sigma_{rr}(r) - 2Q_{12}\sigma_{\varphi\varphi}(r)$ is the renormalized Landau stiffness, $A = A_0(T - T_C)$, A_0 , B , and C are defined for $\text{PbZr}_{0.52}\text{Ti}_{0.48}\text{O}_3$ [102], g is the energetic cost associated with variation of P_r near the surface (1 nm) [98], and $E_d(r) P_r(r)$ is the depolarizing field contribution. Q_{11} and Q_{12} are the electrostrictive coefficients for this composition of PZT [102, 103], and $\sigma_{rr}(r)$ and $\sigma_{\varphi\varphi}(r)$ denote radial and azimuthal stresses, respectively, within the shell. We approximate the depolarizing field, self-consistently, using the form [10] $E_d(r) = 4\pi [P_r(r) - \bar{P}_r]$ i.e. where \bar{P}_r represents the volume averaged polarization across the nano-shell thickness. Sets of $P_r(\rho)$ were obtained by numerical integration of the resulting Euler-Lagrange equation $g\nabla^2 P_r(r) = \hat{A}P_r(r) + BP_r^3(r) + CP_r^5(r) - E_d(r)$ via a nonlinear finite-difference method, subject to the electrostatic boundary conditions $(dP_r/dr - g^{-1}P_r)|_{r=a} = (dP_r/dr + g^{-1}P_r)|_{r=b} = 0$. (See Appendix A for additional details pertaining to the model calculations).

question
how do
you get
<5nm

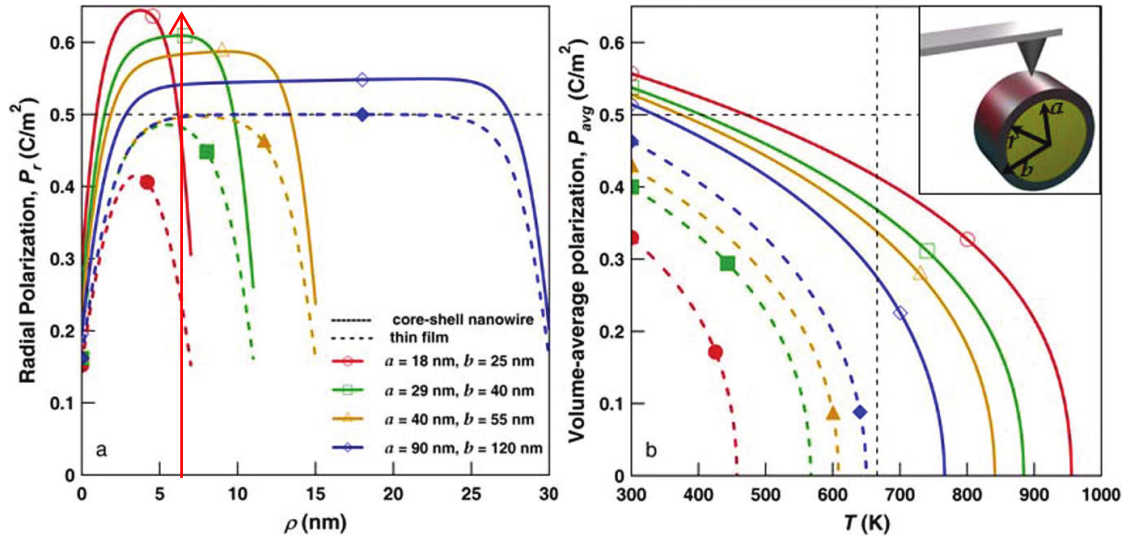


FIGURE 5.3: **a** Calculated (300 K) radial polarization profile for selected values of shell inner and outer radii a and b , respectively (solid lines), and for planar, stress-free thin films of corresponding thicknesses (dashed lines). **b** Calculated volume-averaged P_r as a function of temperature for the nanoshells of selected diameters and thicknesses (solid lines), and for planar, stress-free thin films of corresponding thicknesses (dashed lines) plotted in **a**; the inset illustrates the model geometry. In **a** and **b** the bulk polarization value is denoted by horizontal dashed black lines, and in **b** the bulk T_C value is denoted by a vertical dashed line.

Plots of calculated $P_r(\rho)$ at 300 K for selected pairs of values of a and b are shown in Fig. 5.3(a) along with the calculated P_r versus position for planar, stress-free films of corresponding thicknesses. The polarization profiles for the shells possess distinct curvature- and shell thickness-dependent asymmetric variation, with higher peak polarizations than their planar counterparts. Plotted in Fig. 5.3(b) is a series of calculated results showing the variation of volume-averaged P_r with temperature for these radius and thickness combinations, including those for planar stress-free films of corresponding thicknesses. Remarkably, the expected finite thickness-dependent reduction in P_r , and evolution in T_C are completely suppressed; compared with the planar films of identical thickness, a calculated ~ 500 K increase for the highest-curvature and thinnest shell nanowire is observed. The observed differences in T_C between shell and planar cases increased with decreasing thickness ζ . The results of these model calculations are consistent with our experimental observations of an enhanced FE piezoelectric response shown in Fig. 5.1 and Fig. 5.2(a).

The observed shifts in the hysteresis loops (Fig. 5.2(c) and (d)) results may be compared with those in which engineered strain, composition or temperature gradients in planar single- and multi-layer FE thin films result in polarization gradients, variations in polarization charge offset and T_C , and temperature-dependence of the dielectric permittivity [90]. Electrostatic potential profiles $V(\rho)$ associated with polarization gradients resulting in a bound charge density were obtained using the calculated polarization profiles by numerically solving Poisson's equation assuming open-circuit boundary conditions. The measured vertical shift in the FE piezoelectric hysteresis loops and the results of model calculation of offsets in polarization exhibit an increase for progressively smaller diameter and thinner shell (Fig. 5.3(c)). The variation in the values of the measured voltage and model-calculated potential offsets are in reasonable agreement (Fig. 5.2(d)). A small, fixed portion of the observed offset can be attributed to the Au core and Pt probe tip metal work-function difference, offset by possible contributions from molecular adsorbates between the Pt tip and nano-shell [22], from nano-shell curvature-dependent variation in the effective contact area of the proximal probe tip with the nano-shell surface [104], and from asymmetric leakage currents [105].

An additional finite diameter-dependent source of offset in polarization (and voltage) owing to the finite-size scaling of radial stress and resulting orthogonal strain gradient may contribute to the observed polarization. In piezoelectric materials, in addition to the coupling of a mechanical stress, an additional, but normally small contribution to dielectric or ferroelectric polarization results from a strain gradient [106], i.e. $P_i = d_{ijk}\sigma_{jk} + \mu_{ijkl}(\partial\epsilon_{jk}/\partial x_l)$ where μ_{ijkl} is the flexoelectric tensor. Considering the values of μ_{ijkl} for PZT ($\approx 0.5 \mu\text{ C/m} - 2.0 \mu\text{ C/m}$) [106] an estimate of the magnitude of this effect based on our model calculations results in much larger offsets than those observed experimentally; we propose that defects partially relieve the high radial stress (and strain gradient), thereby providing offset values that are in better agreement with our experimental results. Finally, a surface chemical mechanism [21, 22, 25] relevant to both the FE stability and offsets in the FE hysteresis response that are observed should be noted; molecular adsorbates can be expected to be present on the outer surface of the nanoshells. Adsorbates have been shown to both stabilize ferroelectricity and to introduce asymmetry to the polarization-energy landscape [22]. These effects are

not included in the model calculations.

To conclude, these findings suggest significantly enhanced FE piezoelectric responses and the absence of a systematic decrease for decreasing shell thickness for polarizations oriented along the finite dimension in extremely curved ultra-thin shells are explained by stress-renormalized and polarization gradient contributions to the free energy. These gradients, manifested in the form of geometrically-driven preferred polarization direction and electrostatic potential offsets, produce significant finite curvature-dependent increases in T_C .

Question: translate into English.

Chapter 6

Integrated Nanowire Ferroelectric Field Effect Transistor (FeFET)

Here the experimental design and execution for measuring individual semiconducting silicon-core, FE oxide-shell nanostructures will be discussed. Experimental evidence for transconductance in nanowire channels is presented, with comparison to recent literature of thin film FeFET and non-integrated semiconductor nanowire, FE thin film transistor test structures.

In order to best understand the potential impact of a ferroelectric field effect transistor (FeFET), its foundation, the metal-oxide-semiconductor field effect transistor (MOSFET), must be considered. A typical MOSFET consists of an oxide layer and deposited metal gate on a doped semiconductor (e.g. silicon) substrate. In common platforms, the substrate body is one dopant type while two oppositely doped regions form the source and drain. Depicted in Fig. 6.1 is the NMOS type platform, where the blue regions show the oxide layer, the red the metallic electrodes, the green the n+ source and drain regions, and the gold the gate electrode.

The principle of operation of the MOSFET involves the application of positive voltage between the gate electrode and the source, V_{GS} . This depletes the region directly under the gate oxide layer of holes, thus forming a channel by which current can pass. Current, however, will not traverse the channel until a positive

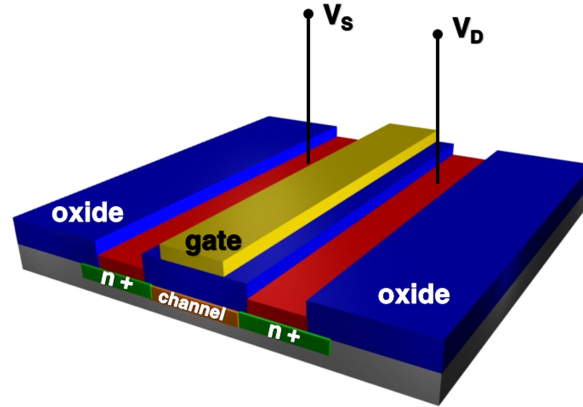
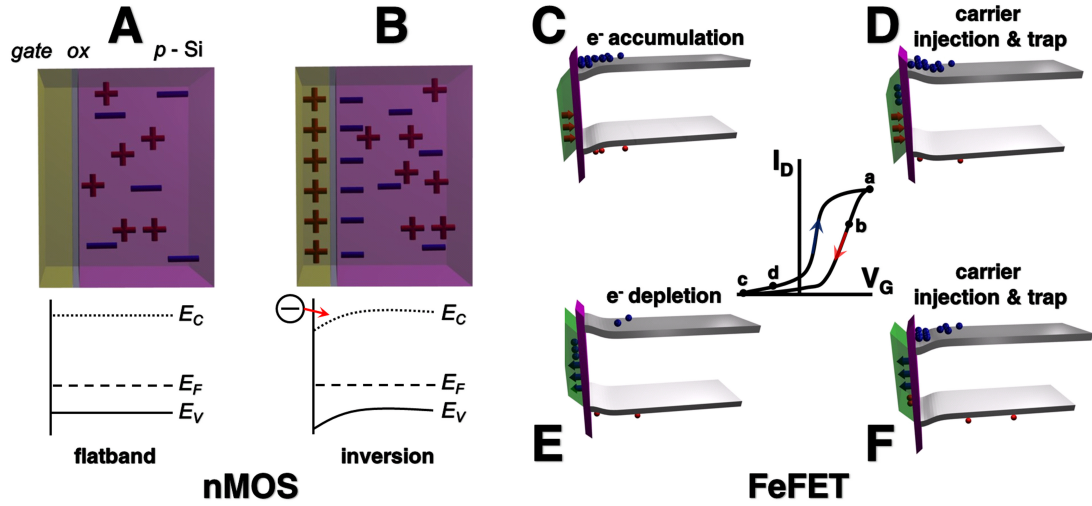


FIGURE 6.1: Schematic of the nMOS architecture

voltage is applied between the source and drain, V_{SD} . Current flow will cease if the V_{SD} applied is either negative or zero.

FeFETs possess identical structure to MOSFETs, with the exception being that a ferroelectric oxide replaces the conventional gate oxide. The feature of ferroelectric oxides that their polarization state (direction) can be switched with an applied electric **field** makes them an important alternative gate material, as their remnant fields can be used to gate the channel after removal of the applied field V_{GS} . Mathews, et al. [107] reported on the effects of the FE within a planar FeFET on channel resistance, while the prospects of a planar ferroelectric gate enhanced nanowire transistor using In_2O_3 [108] and ZnO [109] as the semiconducting channel have also been demonstrated more recently. Stolichnov et al. [110] demonstrated the nonvolatile gate effect within 15-nm CdTe ferroelectric-semiconductor quantum wells. The authors reported that the gate effect results from a conductivity change within the two-dimensional electron gas (2DEG). By using polarization domain engineering, nanometer resolution may be achieved without integrating the ferroelectric layer with the semiconductor base.

Figure 6.2 show the energy band diagrams of nMOS (*left*) and FeFET (*right* [111]) memory platforms. As described earlier if zero gate voltage is applied there exists no channel (i.e. flatband) and hence no possible current is available within the channel. As a gate voltage is applied, the conduction band bends toward the fermi energy level, resulting from charge inversion at the gate-substrate interface. At this point a channel is formed and upon application of a source-drain voltage


 FIGURE 6.2: Band diagrams of **a-b** nMOS and **c-f** FeFET memory platforms

(V_{sd}) a current will be observed. The operation of a FeFET is quite similar in that electrons may either be depleted or accumulated at the surface due to the polarization orientation. The significant difference is that the V_G is not constantly applied, but rather the FET in this case relies on the remnant field formed by the FE polarization to effectively gate the channel at the interface [111].

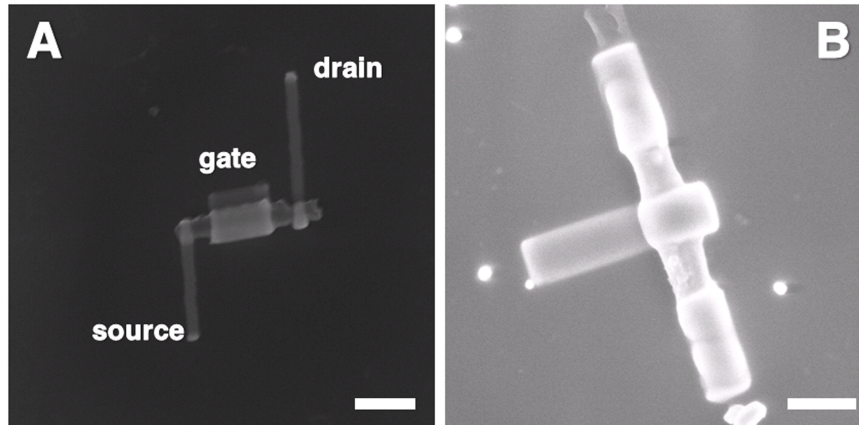


FIGURE 6.3: Electrically contacted SiNW core, PZT-shell nanowires using combined FIB ion milling and EBAD Pt deposition

Silicon nanowire-core, PZT-shell nanowires were fabricated using the methods outlined in Chapter 3. Figures 6.3a and b show examples of contacted Si-PZT core-shell nanowires. The source and drain contacts were fabricated with a combination of ion beam assisted milling [low beam current (10 - 30 pA) conditions] and electron

beam assisted deposition (EBAD) of platinum. A secondary step was necessary to fabricate the third gate electrode within the middle section of the nanostructure, consisting solely of EBAD deposition directly on the oxide shell surface. The oxide surface provided the largest obstacle in this process, as its milling rate far exceeds that of the standard parameters for silicon. Scalebar in 6.3a is 1 μm ; in 6.3b it is 500 nm. Other Si-PZT core-shell nanowires were fabricated using EBL using the methods described in section 3.8; Figure 3.12.



FIGURE 6.4: Illustration of the experimental setup used for gated measurements of I-V through the nanowire core. A sourcemeter is attached to the gate while a picoammeter is attached to the source-drain of the nanowire channel. A gate voltage (V_G) is applied directly to the wrap gate electrode, then removed to collect current, as shown in Figure 6.6

The experimental configuration used to collect current-voltage (I-V) traces of the semiconducting nanowire channel are shown in Figure 6.4. Here, contacted and gated core-shell nanowires are placed into a probe station (Lake Shore Cryotronics TTP4) and interrogated using a sourcemeter (Keithley 2400; gate) and picoammeter (Keithley 6487; source-drain). The following list will outline the process in measuring the nanowire cores and subsequent gating effects:

1. Contacted nanowires 6.3 are first interrogated using the picoammeter to test conductance and assure the nanowire core is electrically addressable 6.5
2. Wires exhibiting a stable I-V trace undergo FIB 6.3 or EBL 3.12 gate fabrication steps
3. Gated core-shell nanowires are placed back into the probe station, with the sourcemeter connected to the gate and the picoammeter to the source-drain
4. Step 1 is repeated to assure the nanowire survived step 2
5. The gate probe is placed in contact with the gate electrode and held at ground, without bias, and step 4 is repeated to see any stray effects of the gate
6. The gate is removed to check if step 4 is reproduced, with no residual effects
7. Step 5 is repeated, only applying a gate voltage (V_G) while an I_{SD} -V is collected instead; the time the gate voltage is applied is ≈ 2 min
8. The gate probe is then lifted off the electrode, and the I_{SD} -V is collected again, to observe any remnant effects
9. Steps 7 and 8 are repeated for varying gate voltages

The steps outline above are the base experimental procedure for the results presented in this chapter. Figure 6.5 represents an I-V collected of a SiNW-PZT core-shell nanowire prior to FIB gate fabrication. The relatively low currents observed (≈ 150 pA) are typical for intrinsic silicon, as expected here considering there was no doping incorporated into the process shown in section 3.6.

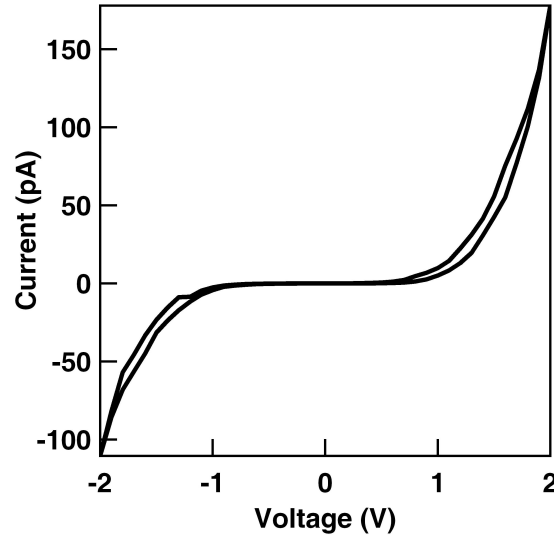


FIGURE 6.5: Collected I_{sd} - V traces of an individual Si-PZT NW FeFET

The so-called continuity check shown in Figure 6.5 allowed the necessary gate fabrication steps to proceed. The gated core-shell nanostructures (Fig. 6.3) were then interrogated with a combination of a sourcemeter on the gate electrode and picoammeter on the source-drain electrodes, as outlined above (Fig. 6.4). Figure 6.6a and b show representative I_{sd} - V traces collected *after* a gate voltage had been applied and subsequently removed to the PZT shell from the wrap gate electrode. Further, the probe tip was removed from the surface of the gate electrode as to avoid any stray electrostatic interactions.

The traces shown in Figures 6.6a and b show a very distinct nonvolatile gating effect with increasing gate (poling) voltage. These effects are similar to the effects of gate voltage on the ferroelectric poling and subsequent change in channel resistance in planar FeFET [107]. The maximum observed current in the original nanowire channel was (≈ 150 pA), while after $5V_G$ the maximum current jumped to (> 20 nA), resulting in a current ratio of ≈ 1000 (see 6.6b).

Further nonvolatile gating effects were explored on gated Si-PZT integrated nanostructures using a HfO_2 dielectric buffer layer between the gate metal and PZT shell, as to reduce possible leakage at the metal/FE interface. The source drain contacts were fabricated using the same methods outlined in section 3.8. Then the sample containing source-drain contacted nanowires were again covered in electron-sensitive 950 K PMMA resist, where lithography was then used

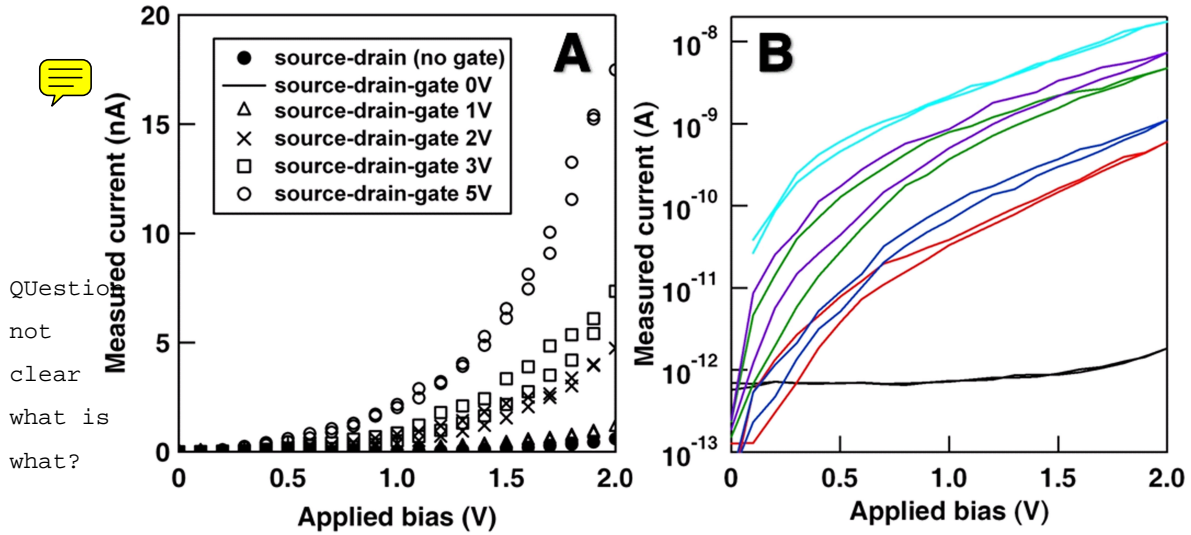


FIGURE 6.6: **a** Collected I_{sd} -V traces of an individual Si-PZT NW FeFET, measured after gate voltages V_G were applied and withdrawn. **b** Log-scale plot of the traces shown in **a**.

to pattern a large square pad over the area between the contacted nanowire ends. Next, a thin layer (< 20 nm) of HfO_2 was deposited via atomic layer deposition (Cambridge Nanotech; Savannah 100) using a precursor consisting of tetrakis(dimethylamido)hafnium and DI water. The precursors were injected into the reactor and held at 200°C separately, with each injection followed by a 10 sec pulse of UHP nitrogen purge gas flowing at 20sccm. The process consisted of 200 precursor/oxidant cycles at a film growth rate of $1\text{\AA}/\text{cycle}$, leading to the final film thickness of $\approx 20\text{nm}$.

Figure 6.7a shows an SEM image of a gated Si-PZT integrated nanowire test structure with a HfO_2 dielectric buffer layer. Figure 6.7b shows a trace of source-drain current ($@ 2V_{SD}$) versus sweeping gate voltage (± 10 V) for an individual test structure. The hysteretic nature of the gate voltage sweep is shown in Figure 6.7 where it can be seen that the I_{SD} saturates with increasing gate voltage and returns to cross the zero axis for applied field with an increased current, as compared to the original current. Upon application of a negative gate bias saturation is again observed, after which the loop is complete to zero. This behavior is identical to those seen in planar FETs [107], as of nanowire channel/planar gated FETs [108, 109]. The ultrathin nanoshell thickness (≈ 10 nm) and integrated nature of

the test structures account for the orders of magnitude difference in the observed gating effects on currents, as compared to previous studies.

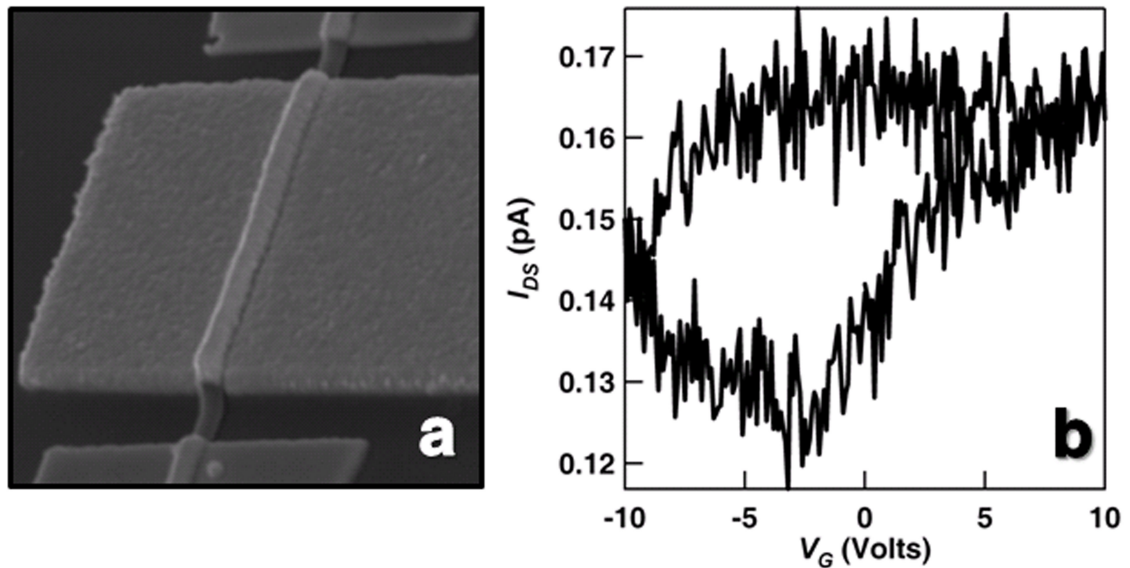


FIGURE 6.7: **a** SEM image of a gated Si-PZT integrated FeFET nanowire with HfO_2 buffer layer. **b** Drain-source current ($@ 2V_{SD}$) versus gate voltage taken of the contacted nanostructure shown in **a**.

These results are noteworthy in light of the latest report issued by the International Technology Roadmap for Semiconductors (ITRS), the silicon memory industry authority that mandates all necessary fabrication processes needed to reduce node width for semiconductor based memory platforms. In its latest update [112], a new paradigm for FE-based memory architectures was presented, shifting from the 2D stack geometry most commonly associated with memory devices to a 3D hemispherical geometry. Three dimensional hemispherical FE capacitors have been studied for over a decade [113], with more recent studies showing enhancements in the saturation polarization as compared to 2D stacks of the same composition due to increased contributions of the electrode sidewalls [114].

The ITRS update calls for the “integration of scaling of FeRAM ferroelectric materials”. Due to high leakage currents and subsequent loss of polarization with decreasing thickness, integration of ferroelectrics into memory architectures has proven rather difficult. The Si-PZT core-shell nanowires presented in Fig. 3.12

and 6.3 represent nanoscale integration of silicon in direct contact with the ferroelectric oxide PZT. Moreover, these individual elements may be manipulated into arrays on arbitrary substrates, create ~~more~~ a more flexible design platform for next generation elements.

Additionally, the ITRS calls for industry processes to continue the application of strain engineering techniques (shown in section 2.5) in order to circumvent the inherent problems associated with leakage and polarization loss in nanoscale ferroelectrics. Again, the Si-PZT core-shell nanowires shown here exhibit enhanced ferroelectric stability (see Fig. 5.2; Chapter 5) due to nonlinear coupled surface-tension induced stress to charge via electrostriction. The integration of a semiconductor nanowire channel with a ferroelectric oxide sheath, combined with the stability provided by nonlinear electromechanical coupling suggest the Si-PZT nanowires presented here provide strong evidence for a nascent design platform for 3D, non-planar memory elements. (*Note: an additional study of the resistance switching character of the leakage properties between the Si-PZT interface are found in Appendix X*)

question

Chapter 7

Redox-Based Resistive Switching of Ferroelectric Nanotubes

Here, the resistive switching character of the leakage response of fabricated test structures are shown. The experimental scan probe technique enabling simultaneous collection of FE hysteresis and resistive current response is presented. Additional test structures consisting of lithography-based electrodes further clarify the resistive switching character, with a focus on the effects of oxygen environment in mediating transport. These studies provide evidence for an oxygen-vacancy transport mechanism, which will be discussed in terms of nonstoichiometric perovskite lattice chemistry.

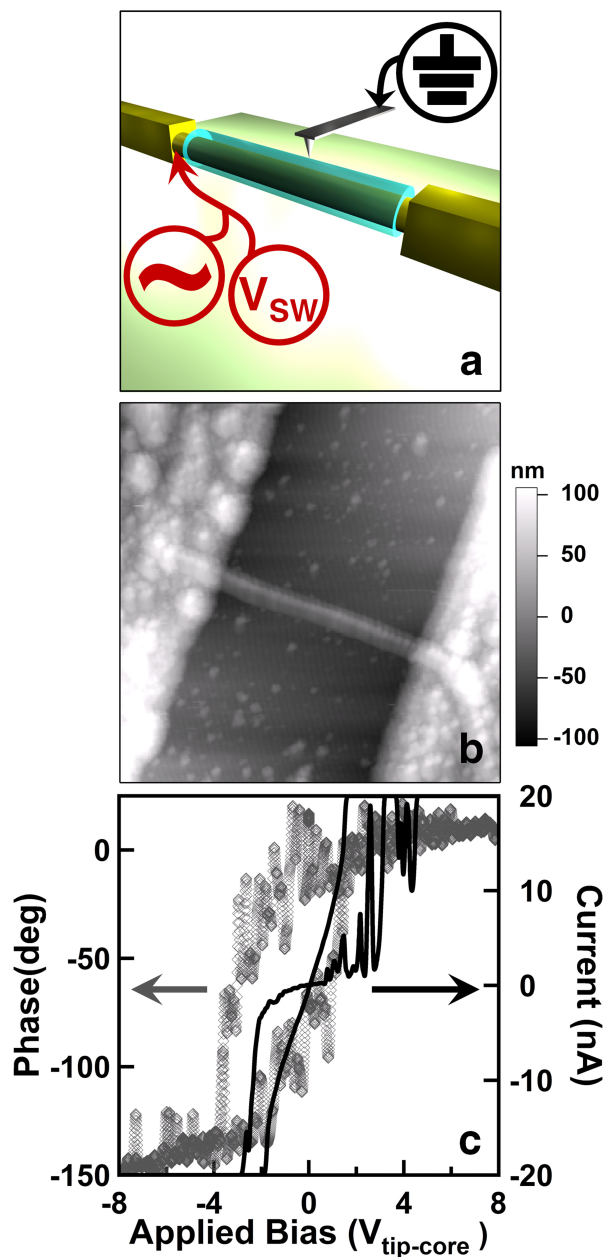
Developments in the synthesis of low-dimensional ferroelectric (FE) nanostructures such as nanoparticles [32], nanowires [22, 63] and nanotubes [40, 41, 70] have renewed interest in the miniaturization of ferroic systems for use as next generation memory elements. Recently remarkable experimental and theoretical findings have shown unique topologically-driven features such as finite curvature-mediated FE stability [86, 96] and toroidal domain ordering [81, 85] effectively conserve polar properties, which is critical to typical non-volatile FE applications involving careful manipulation of spontaneous polarization to produce an “on” or “off” memory state. Nanoscale FE systems have also garnered interest as current-based switching elements due to their large resistance ratios and non-destructive readout states [77, 78]. Resistive switching has been observed in a number of oxide

materials, including thin-film binary oxides TiO_2 [115, 116], ZrO_2 [117], and MnO_2 [118], and thin-film ABO_3 oxide perovskites [119, 120, 121, 122], adding greater functionality to known ferroic properties in developing memory applications.

Observed resistive behavior in FE materials has been explained thus far by either tunneling or defect-mediated mechanisms. In recent work a charge trap conduction model has been proposed, whereby charges are injected via Fowler-Nordheim tunneling [78] and trapped within defects, a mechanism strongly dependent upon polarization orientation, particularly at the metal/FE interface [76, 123, 124, 125]. Others have proposed a filamentary conduction mechanism [126] via electroformation and electromigration of extended defects such as oxygen vacancies [127] and dislocations [122, 128] within materials possessing mixed valence character, thus attributing conduction to anion transport. To date, studies of resistive switching in FE and non-FE oxides have involved exclusively thin films. Here the resistive switching in selected areas within individual ferroelectric oxide perovskite nanotubes possessing conductive Au-nanowire cores is reported. Simultaneous occurrence of the resistive and ferroelectric switching in these nanostructures is observed, and experimental evidence for an oxygen vacancy concentration-mediated electroresistance is provided.

Details of the synthesis method, test structure, and structural characterizations of Au-filled PZT nanotubes employed for this study have been presented elsewhere [70] (see Ch. 3).

The local probe setup allowing simultaneous collection of FE piezoelectric phase hysteresis and resistive current-voltage response of an individual Au-PZT core-shell nanowire (50 nm diameter, 7 nm shell thickness) is depicted in Fig. 7.1a. Here a cantilever holder containing a built-in transimpedance amplifier (ORCATM, Asylum Research) enables the required current sensitivity to measure the FE and resistive switching simultaneously [76, 121]. An electrically-grounded cantilever tip (Olympus AC240TM) was placed in contact with the bare PZT nanotube surface (Fig. 7.1b), employing constant-deflection feedback. In a typical experiment a waveform consisting of a low-frequency zero-offset triangular component (3 Hz, $\pm 16 \text{ V}_{pp}$) and a higher frequency component (10 kHz, 2 V_{AC}) was applied to the nanowire core (inner electrode) during a deflection-triggered force-pull sequence in



Question;
what are
two lines
seen ??

FIGURE 7.1: **a** - schematic of simultaneous IV-hysteresis collection where an arbitrary waveform consisting of two frequency components is applied directly to the Au-core inner electrode, as described in the main text. **b** Topographic AFM height image of a contacted 50 nm core-shell nanostructure (scan size $5 \times 5 \mu\text{m}$). **c** - ferroelectric piezoelectric hysteresis (*grey markers*, left axis) and resistive current-voltage (*black line*, right axis) simultaneously collected by a grounded conductive cantilever connected to a transimpedance amplifier. The bias $V_{\text{core-tip}}$ is applied from the nanowire core through the FE nanotube wall and collected at the tip, hence the reverse x-axis.

which the cantilever was in continuous contact and constant deflection feedback, thus allowing collection of the ferroelectric piezoelectric deflection phase signal (Fig. 7.1c; left axis) and resistive current (Fig. 7.1c; right axis) through the nanotube wall.

The ferroelectric phase signal exhibits a distinct offset along the voltage axis (Fig. 7.1c). This offset can be attributed to an electrostatic potential gradient arising from the finite curvature of the shell [96], from different surface chemical environments of the inner and outer surfaces of the nanotube [70], and differences in metal work function between the inner electrode (Au) and the cantilever tip coating (Pt). Observed vertical shifts indicate a preferred polarization orientation [76], previously shown for FE nanoshells as a result of curvature-driven polarization gradients [96]. The observed electroresistance in the nanotube wall (Fig. 7.1c, right axis) can be described by an equivalent circuit consisting of a diode set in parallel with a single resistor that is split by a switch [116]. In a voltage sweep cycle (from 0 V) the resulting resistive switching character is highly blocking (diode-like) in the first quarter, then **substantially less blocking (nearly Ohmic) during the second and third quarters, then it returns to highly blocking in the final quarter, as seen in the collected I-V trace** (Fig. 7.1c).

Notably, the observed critical voltage V_{cr} is nearly identical to the FE coercive voltage $V_C \approx 2$ V. The on/off current ratios approach 10^3 , with a measured on-current value of 20 nA. This current value, however, is orders of magnitude lower than those for typical resistive memory elements (μA -mA) [127]. The observed reduction in the scale of currents reported implies a current limit exists due to Fowler-Nordheim tunneling between the probe tip and nanotube surface, similar to current response shown in FE thin films [78]. This is not surprising given the scale of the AFM probe tip (~ 30 nm diameter) in relation to the size of electrical contacts used in other electroresistance switching experiments involving thin films [121].

From the data observed in Fig. 7.2 it is proposed these nanostructures could potentially be used as novel electroresistive and FE memory elements in which each nanowire contains one or more distinct switching elements within the shell portion of these core-shell nanowires using fixed electrodes. Electrical contacts to

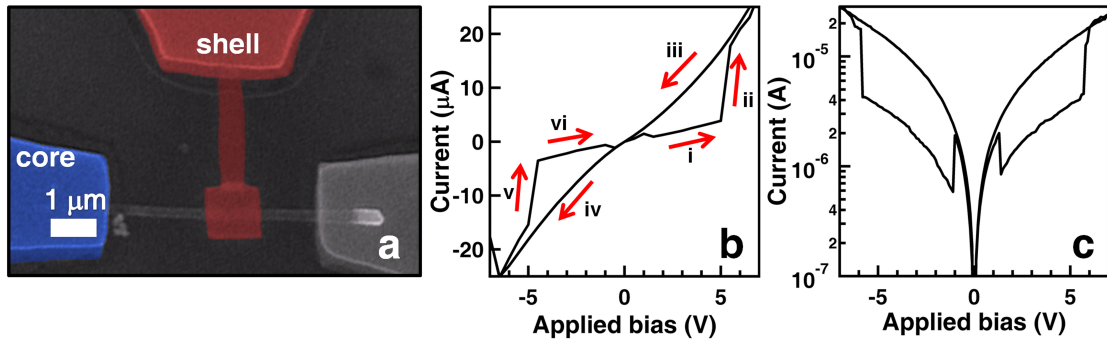


FIGURE 7.2: **a** - (*false color*) SEM image of top-electroded core-shell nanostructure, showing measurement path between Pt-top electrode (**shell**; *red*) and left nanowire-core electrode (**core**; *blue*) (scalebar = 1 μm). **b** - representative resistive current-voltage character of a shell-electroded Au-core, PZT-shell nanostructure. **c** - log-based plot of current-voltage showing an order of magnitude difference in current across the finite-thickness direction of the core-shell nanostructure.

the Au nanowire cores (Fig. 7.2a; *false color*: **blue**) were made using electron beam lithography, wet etching, resistive thermal evaporation (10 nm Cr and 150 nm Au). Electron beam-induced deposition of Pt using a dual-beam FIB-SEM (FEI DB235) was carried out, producing a 500 x 100 nm electrode of 250 nm in height on the outer surface of the nanowire (Fig. 7.2a; *false color*: **red**).

The structures were then mounted in a probe station (Lake Shore Cryotronics TTP4) and interrogated using a source meter (Keithley 2400) and picoammeter (Keithley 6487). Measurements were collected through the nanotube wall between the top electrode (**shell**) and left nanowire-core electrode (**core**). Shown in Fig. 7.2b is the collected resistive current-voltage response of a segment of the core-shell test structure; the measured current values are denoted by the sequence **i** - **vi**. The observed on-current value greatly increased (30 μA) with respect to the proximal probe measurements (20 nA). The average on/off current ratios in the shell-electrode nanostructures were approximately one order of magnitude (Fig. 7.2c).

To understand the underlying mechanism driving the observed electroresistances, the fixed-electroded test structures were subjected to an annealing cycle consisting of O_2 -rich/ O_2 -deficient/ O_2 -rich steps, with collection of the I-V response

following each step. Following collection of the initial I-V response of the as-prepared shell-electroded test structures (Fig. 7.2b), the structures were annealed for 1 hour at 450°C under a constant flow of 100 sccm O₂ (Airgas UHP) at a base pressure of 2 Torr (“O₂-rich”). After the first O₂-rich step the I-V character of the shell-electroded test structures was seen to exhibit a ~10³- fold decrease in current (Fig. 7.3a). The nanostructures were then subjected to a forming gas anneal (FGA) for 1 hour 450°C under a constant flow of 100 sccm 95%N₂-5%H₂ (Airgas HINY200) at a base pressure of 2 Torr (“O₂-deficient”). The collected O₂-deficient I-V response (Fig. 7.3b) possessed a ~10⁵ increase in current (I > 150 μA) manifested by the onset of resistive switching, with a on/off ratio of ~10⁴. A final O₂-rich anneal step (450°C, 5 hours, 2 Torr) was performed to confirm the reversibility of the oxygen mechanism for conduction within the PZT nanoshell (Fig. 7.3c). The increased anneal time was selected to promote the filling of the O₂ vacancies created during the O₂-deficient anneal with oxygen atoms.

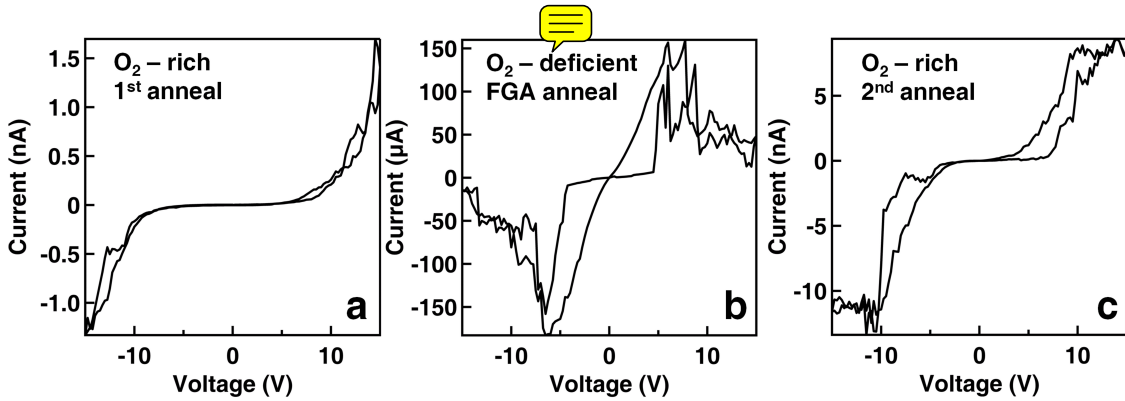
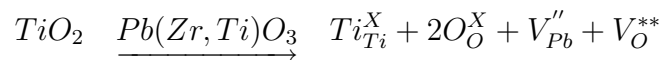
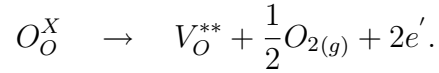


FIGURE 7.3: Current - voltage sweeps of a Au-PZT core-shell nanowires after a **a** - O₂-rich/**b** - O₂-deficient/**c** - O₂-rich annealing cycle.

These results indicate an oxygen defect-mediated conduction process. The higher conduction state observed in Fig. 7.3b is attributed to formation of oxygen vacancies in an O₂-deficient or low p_{O_2} environment. From the general form for a nonstoichiometric perovskite, the defect reaction for a B-site rich titanate, such as PZT, becomes [129]



where oxygen vacancies assist the conduction process by yielding electrons:



question

Considering the strong dependence of oxygen vacancy concentration on oxygen partial pressure, we propose that the large differences observed in current between the O₂-rich and O₂-deficient anneal steps are explained through vacancy formation, as previously shown in TiO₂-based nanotubes via resonance spectroscopy [130]. The results shown in Fig. 3b also support a filamentary conduction mechanism, by which oxygen vacancies migrate from the anode toward the cathode. The onset of resistive switching after an O₂-deficient anneal suggests that a critical oxygen vacancy concentration is necessary for a switching event. Additional mechanisms may also be present, including the proposed formation of transition metal anion nanofilaments along grain boundaries of polycrystalline grains [126, 131] due to oxygen migration.

In conclusion simultaneous collection of FE switching and electroresistance in an individual PZT nanoshell across the finite, shell-normal direction, and the electroresistance switching within a segment of the nanoshell possessing a fixed electrode has been demonstrated. **The large on/off current ratios (10¹ - 10⁴) are**

question

consistent with an oxygen vacancy-mediated transport mechanism which allows for anion transport along grain boundaries of polycrystalline films. Nanostructures subjected to controlled oxygen environments consisting of a O₂-rich/O₂-deficient/O₂-rich anneal cycle exhibited O₂-deficient/O₂-rich current ratios of ~ 10⁵. We believe demonstration of simultaneous electroresistive and FE switching along the finite dimension within ABO₃ oxide perovskite nanowires as shown here will encourage further interest in investigating these features within high functional density oxide nanostructures and their potential application.

Bibliography

- [1] W. G. Cady. *Piezoelectricity*. Dover Publications, New York, 1964.
- [2] A. Devonshire. Theory of ferroelectrics. *Advances in Physics*, 3(10):85–130, 1954.
- [3] L. E. Cross. *Thermodynamic phenomenology of ferroelectricity in single crystal and ceramic systems*. Dekker, New York, 1972.
- [4] M. E. Lines and A. M. Glass. *Principles and Applications of Ferroelectrics and Related Materials*. Clarendon Press, Oxford, 1977.
- [5] D. Damjanovic. Ferroelectric, dielectric and piezoelectric properties of ferroelectric thin films and ceramics. *Rep. Prog. Phys.*, 61:12671324, —1998—.
- [6] J. Junquera and P. Ghosez. Critical thickness for ferroelectricity in perovskite ultrathin films. *Nature*, 422(6931):506–509, —2003—.
- [7] V. Nagarajan, C. L. Jia, H. Kohlstedt, R. Waser, I. B. Misirlioglu, S. P. Alpay, and R. Ramesh. Misfit dislocations in nanoscale ferroelectric heterostructures. *Applied Physics Letters*, 86(19):192910–3, —2005—.
- [8] M.-W. Chu, I. Szafraniak, R. Scholz, C. Harnagea, D. Hesse, M. Alexe, and U. Gosele. Impact of misfit dislocations on the polarization instability of epitaxial nanostructured ferroelectric perovskites. *Nature Materials*, 3(2):87–90, —2004—.
- [9] V.L. Ginzburg and L.D. Landau. *Zh. Eksp. Teor. Fiz.*, 20:1064, 1950).
- [10] A. M. Bratkovsky and A. P. Levanyuk. Smearing of phase transition due to a surface effect or a bulk inhomogeneity in ferroelectric nanostructures. *Physical Review Letters*, 94(10):107601, —2005—.

- [11] R. Kretschmer and K. Binder. Surface effects on phase transitions in ferroelectrics and dipolar magnets. *Physical Review B*, 20(3):1065, —1979—.
- [12] C. L. Wang and S. R. P. Smith. Landau theory of the size-driven phase transition in ferroelectrics. *J. Phys. Cond. Matt.*, 7:7163, —1995—.
- [13] K. J. Choi, M. Biegalski, Y. L. Li, A. Sharan, J. Schubert, R. Uecker, P. Reiche, Y. B. Chen, X. Q. Pan, V. Gopalan, L.-Q. Chen, D. G. Schlom, and C. B. Eom. Enhancement of ferroelectricity in strained batio₃ thin films. *Science*, 306(5698):1005–1009, —2004—.
- [14] J. H. Haeni, P. Irvin, W. Chang, R. Uecker, P. Reiche, Y. L. Li, S. Choudhury, W. Tian, M. E. Hawley, B. Craigo, A. K. Tagantsev, X. Q. Pan, S. K. Streiffer, L. Q. Chen, S. W. Kirchoefer, J. Levy, and D. G. Schlom. Room-temperature ferroelectricity in strained sr₂ti₃. *Nature*, 430(7001):758–761, —2004—.
- [15] A. Q. Jiang, J. F. Scott, M. Dawber, and C. Wang. Fatigue in artificially layered pb(zr,ti)o₃ ferroelectric films. *Journal of Applied Physics*, 92(11):6756–6761, —2002—.
- [16] N. Sai, C. J. Fennie, and A. A. Demkov. Absence of critical thickness in an ultrathin improper ferroelectric film. *Physical Review Letters*, 102(10):107601, —2009—.
- [17] E. Bousquet, M. Dawber, N. Stucki, C. Lichtensteiger, P. Hermet, S. o Gariglio, J.-M. Triscone, and P. Ghosez. Improper ferroelectricity in perovskite oxide artificial superlattices. *Nature*, 452(7188):732–736, —2008—.
- [18] M. P. Warusawithana, C. R. Cen, C. and Sleasman, J. C. Woicik, Y. Li, L. F. Kourkoutis, J. A. Klug, H. Li, P. Ryan, L.-P. Wang, M. Bedzyk, D. A. Muller, L.-Q. Chen, J. Levy, and D. G. Schlom. A ferroelectric oxide made directly on silicon. *Science*, 324(5925):367–370, —2009—.
- [19] D. D. Fong, G. B. Stephenson, S. K. Streiffer, J. A. Eastman, O. Auciello, P. H. Fuoss, and C. Thompson. Ferroelectricity in ultrathin perovskite films. *Science*, 304(5677):1650–1653, —2004—.

- [20] C. Lichtensteiger, J.-M. Triscone, J. Junquera, and P. Ghosez. Ferroelectricity and tetragonality in ultrathin pbtio₃ films. *Physical Review Letters*, 94(4):047603–4, —2005—.
- [21] D. D. Fong, A. M. Kolpak, J. A. Eastman, S. K. Streiffer, P. H. Fuoss, G. B. Stephenson, Carol Thompson, D. M. Kim, K. J. Choi, C. B. Eom, I. Grinberg, and A. M. Rappe. Stabilization of monodomain polarization in ultrathin pbtio₃ films. *Physical Review Letters*, 96(12):127601, —2006—.
- [22] J.E. Spanier, A.M. Kolpak, J.J. Urban, I. Grinberg, L. Ouyang, W.S. Yun, A.M. Rappe, and H. Park. Ferroelectric phase transition in individual single-crystalline batio₃ nanowires. *Nano Lett.*, 6(4):735–739, —2006—.
- [23] J.J. Urban, J.E. Spanier, L. Ouyang, W.S. Yun, and H. Park. Single-crystalline barium titanate nanowires. *Advanced Materials*, 15(5):423–426, —2003—.
- [24] Z. Weishauptov, V. Machovic, M. Novotn, and J. Medek. Ftir spectroscopy and sorption of water vapour as methods of identification of hydrated zirconium dioxide on a corrosion layer of zirconium alloy. *Materials Chemistry and Physics*, 102(2-3):219–224, —2007—.
- [25] R. V. Wang, D. D. Fong, F. Jiang, M. J. Highland, P. H. Fuoss, Carol Thompson, A. M. Kolpak, J. A. Eastman, S. K. Streiffer, A. M. Rappe, and G. B. Stephenson. Reversible chemical switching of a ferroelectric film. *Physical Review Letters*, 102(4):047601–4, —2009—.
- [26] D. Li, M. H. Zhao, Garra J., A. M. Kolpak, A. M. Rappe, D. A. Bonnell, and J. M. Vohs. Direct in situ determination of the polarization dependence of physisorption on ferroelectric surfaces. *Nature Materials*, 7:473, 2008.
- [27] V. Nagarajan, S. Prasertchoung, T. Zhao, H. Zheng, J. Ouyang, R. Ramesh, W. Tian, X. Q. Pan, D. M. Kim, C. B. Eom, H. Kohlstedt, and R. Waser. Size effects in ultrathin epitaxial ferroelectric heterostructures. *Applied Physics Letters*, 84(25):5225–5227, —2004—.
- [28] L. M. Eng. Nanoscale domain engineering and characterization of ferroelectric domains. *Nanotechnology*, 10:405, 1999.

- [29] A. Rdiger and R. Waser. Size effects in nanoscale ferroelectrics. *Journal of Alloys and Compounds*, 449(1-2):2–6, —2008—.
- [30] M. Alexe and D. Hesse. Self-assembled nanoscale ferroelectrics. *Journal of Materials Science*, 41:1–11, 2006.
- [31] Y. Xia, P. Yang, Y. Sun, Y. Wu, B. Mayers, B. Gates, Y. Yin, F. Kim, and H. Yan. One-dimensional nanostructures: Synthesis, characterization, and applications. *Advanced Materials*, 15(5):353–389, —2003—.
- [32] S. O’Brien, L. Brus, and C. B. Murray. Synthesis of monodisperse nanoparticles of barium titanate: Toward a generalized strategy of oxide nanoparticle synthesis. *Journal of the American Chemical Society*, 123(48):12085–12086, —2001—.
- [33] Songhak Yoon, Sunggi Baik, Min Gyu Kim, and Namsoo Shin. Formation mechanisms of tetragonal barium titanate nanoparticles in alkoxide/hydroxide sol-precipitation synthesis. *Journal of the American Ceramic Society*, 89(6):1816–1821, —2006—.
- [34] Takuya Hoshina, Hirofumi Kakemoto, Takaaki Tsurumi, Satoshi Wada, and Masatomo Yashima. Size and temperature induced phase transition behaviors of barium titanate nanoparticles. *Journal of Applied Physics*, 99(5):054311–8, —2006—.
- [35] Jianling Zhao, Xiaohui Wang, Longtu Li, Xixin Wang, and Yangxian Li. Stoichiometry control and structure evolution in hydrothermally derived (ba,sr)tio₃ films. *Ceramics International*, 34(5):1223–1227, —2008—.
- [36] Dongmok Whang, Song Jin, Yue Wu, and Charles M. Lieber. Large-scale hierarchical organization of nanowire arrays for integrated nanosystems. *Nano Letters*, 3(9):1255–1259, —2003—.
- [37] Hideki Masuda and Kenji Fukuda. Ordered metal nanohole arrays made by a two-step replication of honeycomb structures of anodic alumina. *Science*, 268(5216):1466–1468, —1995—.

- [38] V. Sadasivan, C. P. Richter, L. Menon, and P. F. Williams. Electrochemical self-assembly of porous alumina templates. *AIChE Journal*, 51(2):649–655, —2005—.
- [39] M. Steinhart, J. H. Wendorff, A. Greiner, R. B. Wehrspohn, K. Nielsch, J. Schilling, J. Choi, and U. Gosele. Polymer nanotubes by wetting of ordered porous templates. *Science*, 296(5575):1997–, —2002—.
- [40] B. A. Hernandez, K.-S. Chang, E. R. Fisher, and P. K. Dorhout. Sol-gel template synthesis and characterization of batio/sub3 and pbtio/sub 3 nanotubes. *Chem. Mater.*, 14:480–482, —2002—.
- [41] Y. Luo, I. Szafraniak, N. D. Zakharov, V. Nagarajan, M. Steinhart, R. B. Wehrspohn, J. H. Wendorff, R. Ramesh, and M. Alexe. Nanoshell tubes of ferroelectric lead zirconate titanate and barium titanate. *Applied Physics Letters*, 83(3):440–442, —2003—.
- [42] F. D. Morrison, L. Ramsay, and J. F. Scott. High aspect ratio piezoelectric strontiumndash;bismuthndash;tantalate nanotubes. *Journal of Physics: Condensed Matter*, 15(33):L527–L532, —2003—.
- [43] Tae-Jin Park, Yuanbing Mao, and Stanislaus S. Wong. Synthesis and characterization of multiferroic bifeo3 nanotubes. *Chemical Communications*, (23):2708–2709, —2004—.
- [44] L. Zhao, M. Steinhart, J. Yu, and U. Gosele. Lead titanate nano- and microtubes. *Journal of Materials Research*, 21:685, 2006.
- [45] J.Y. Cheng, C.A. Ross, H.I. Smith, and E.L. Thomas. Templated self-assembly of block copolymers: Top-down helps bottom-up. *Advanced Materials*, 18(19):2505–2521, —2006—.
- [46] W. Lee, H. Han, A. Lotnyk, M. A. Schubert, S. Senz, M. Alexe, D. Hesse, S. Baik, and U. Gosele. Individually addressable epitaxial ferroelectric nanocapacitor arrays with near 10^{12} density. *Nature Materials*, 3(7):402–407, —2008—.
- [47] P.R. Evans, X. Zhu, P. Baxter, M. McMillen, J. McPhillips, F.D. Morrison, J.F. Scott, R.J. Pollard, R.M. Bowman, and J.M. Gregg. Toward

- self-assembled ferroelectric random access memories: Hard-wired switching capacitor arrays with almost $\text{tb}/\text{in.}^2$ densities. *Nano Lett.*, 7(5):1134–1137, —2007—.
- [48] Woo Lee, Ran Ji, Ulrich Gosele, and Kornelius Nielsch. Fast fabrication of long-range ordered porous alumina membranes by hard anodization. *Nat Mater*, 5(9):741–747, —2006—.
- [49] Larry L. Hench and Jon K. West. The sol-gel process. *Chemical Reviews*, 90(1):33–72, —1990—.
- [50] Martin Steinhart, Joachim H. Wendorff, and Ralf B. Wehrspohn. Nanotubes la carte: Wetting of porous templates. *ChemPhysChem*, 4(11):1171–1176, —2003—.
- [51] Charles R. Martin. Nanomaterials: A membrane-based synthetic approach. *Science*, 266(5193):1961–1966, —1994—.
- [52] Charles R. Martin. Membrane-based synthesis of nanomaterials. *Chemistry of Materials*, 8(8):1739–1746, —1996—.
- [53] T. A. Green, M. J. Liew, and S. Roy. Electrodeposition of gold from a thiosulfate-sulfite bath for microelectronic applications. *Journal of The Electrochemical Society*, 150(3):C104–C110, —2003—.
- [54] J. Liu, J. L. Duan, M. E. Toimil-Morales, S. Karim, T. W. Cornelius, D. Dobrev, H. J. Yao, Y. M. Sun, M. D. Hou, D. Mo, Z. G. Wang, and R. Neumann. Electrochemical fabrication of single-crystalline and polycrystalline Au nanowires: the influence of deposition parameters. *Nanotechnology*, 17(8):1922, —2006—.
- [55] Marc Bockrath, David H. Cobden, Paul L. McEuen, Nasreen G. Chopra, A. Zettl, Andreas Thess, and R. E. Smalley. Single-electron transport in ropes of carbon nanotubes. *Science*, 275(5308):1922–1925, —1997—.
- [56] Yi Cui and Charles M. Lieber. Functional nanoscale electronic devices assembled using silicon nanowire building blocks. *Science*, 291(5505):851–853, —2001—.

- [57] Kok-Keong Lew and Joan M. Redwing. Growth characteristics of silicon nanowires synthesized by vapor-liquid-solid growth in nanoporous alumina templates. *Journal of Crystal Growth*, 254(1-2):14–22, —2003—.
- [58] Kok-Keong Lew, Cordula Reuther, Altaf H. Carim, Joan M. Redwing, and Benjamin R. Martin. Template-directed vapor-liquid-solid growth of silicon nanowires. *Journal of Vacuum Science Technology B: Microelectronics and Nanometer Structures*, 20(1):389–392, —2002—.
- [59] H. Okamoto and T. B. Massalski. The au-si (gold-silicon) system. *Journal of Phase Equilibria*, 4:190, 1983.
- [60] Z. Chen, C.o Yang, B. Li, M. Sun, and B. Yang. Preferred orientation controlling of pzt (52-48) thin films prepared by sol-gel process. *Journal of Crystal Growth*, 285(4):627–632, —2005—.
- [61] S. G. Yang, T. Li, L. S. Huang, T. Tang, J. R. Zhang, B. X. Gu, Y. W. Du, S. Z. Shi, and Y. N. Lu. Stability of anodic aluminum oxide membranes with nanopores. *Physics Letters A*, 318(4-5):440–444, —2003—.
- [62] J. Kim, S. A. Yang, Y. C. Choi, J. K. Han, K. O. Jeong, Y. J. Yun, D. J. Kim, S. M. Yang, D. Yoon, H. Cheong, K.-S. Chang, T. W. Noh, and S. D. Bu. Ferroelectricity in highly ordered arrays of ultra-thin-walled pb(zr,ti)o₃ nanotubes composed of nanometer-sized perovskite crystallites. *Nano Letters*, 8(7):1813–1818, —2008—.
- [63] X. Y. Zhang, X. Zhao, C. W. Lai, J. Wang, X. G. Tang, and J. Y. Dai. Synthesis and piezoresponse of highly ordered pb(zr_{0.53}ti_{0.47})o₃ nanowire arrays. *Applied Physics Letters*, 85(18):4190–4192, —2004—.
- [64] X. H. Zhu, P. R. Evans, D. Byrne, A. Schilling, C. Douglas, R. J. Pollard, R. M. Bowman, J. M. Gregg, F. D. Morrison, and J. F. Scott. Perovskite lead zirconium titanate nanorings: Towards nanoscale ferroelectric “solenoids”? *Applied Physics Letters*, 89(12):122913–3, —2006—.
- [65] M. Hatzakis. Electron beam processing systems (a state of the art review). *Polymer Engineering Science*, 14(7):516–517, —1974—.

- [66] Takashi Ito and Shinji Okazaki. Pushing the limits of lithography. *Nature*, 406(6799):1027–1031, —2000—.
- [67] Alfredo M. Morales and Charles M. Lieber. A laser ablation method for the synthesis of crystalline semiconductor nanowires. *Science*, 279(5348):208–211, —1998—.
- [68] S. Ezhilvalavan and Victor D. Samper. Ferroelectric properties of wet-chemical patterned pbzr[sub 0.52]ti[sub 0.48]o[sub 3] films. *Applied Physics Letters*, 86(7):072901–3, —2005—.
- [69] F. Watt, A. A. Bettiol, J. A. Van Kan, E. J. Teo, and M. B. H. Breese. Ion beam lithography and nanofabrication: A review. *International Journal of Nanoscience*, 4:269–286, 2005.
- [70] S. S. Nonnenmann, E. M. Gallo, M. T. Coster, G. R. Soja, C. L. Johnson, R. S. Joseph, and J. E. Spanier. Piezoresponse through a ferroelectric nanotube wall. *Applied Physics Letters*, 95(23):232903–3, —2009—.
- [71] G. Binnig, C. F. Quate, and Ch Gerber. Atomic force microscope. *Physical Review Letters*, 56(9):930, —1986—.
- [72] G. Friedbacher and H. Fuchs. Classification of scanning probe microscopy techniques. *Pure Appl. Chem*, 71:1337, 1999.
- [73] Lawrence A. Bottomley. Scanning probe microscopy. *Analytical Chemistry*, 70(12):425–476, —1998—. doi: 10.1021/a1980011o.
- [74] S.V. Kalinin, A. Rar, and S. Jesse. A decade of piezoresponse force microscopy: Progress, challenges, and opportunities. *IEEE Trans. Ultrason. Ferro. Freq.*, 53:2226, 2006.
- [75] A. Gruverman, H. Tokumoto, A. S. Prakash, S. Aggarwal, B. Yang, M. Wuttig, R. Ramesh, O. Auciello, and T. Venkatesan. Nanoscale imaging of domain dynamics and retention in ferroelectric thin films. *Applied Physics Letters*, 71(24):3492–3494, —1997—.

- [76] A. Gruverman, D. Wu, H. Lu, Y. Wang, H. W. Jang, C. M. Folkman, M. Ye Zhuravlev, D. Felker, M. Rzchowski, C. B. Eom, and E. Y. Tsymlal. Tunneling electroresistance effect in ferroelectric tunnel junctions at the nanoscale. *Nano Letters*, 9(10):3539–3543, —2009—.
- [77] V. Garcia, S. Fusil, K. Bouzehouane, S. Enouz-Vedrenne, N. D. Mathur, A. Barthelemy, and M. Bibes. Giant tunnel electroresistance for non-destructive readout of ferroelectric states. *Nature*, 460(7251):81–84, —2009—.
- [78] P. Maksymovych, S. Jesse, P. Yu, R. Ramesh, A. P. Baddorf, and S. V. Kalinin. Polarization control of electron tunneling into ferroelectric surfaces. *Science*, 324(5933):1421–1425, —2009—.
- [79] M. Alexe, D. Hesse, V. Schmidt, S. Senz, H. J. Fan, M. Zacharias, and U. Gosele. Ferroelectric nanotubes fabricated using nanowires as positive templates. *Applied Physics Letters*, 89(17):172907–3, —2006—.
- [80] Ming Liu, Xin Li, Hassan Imrane, Yajie Chen, Trevor Goodrich, Zhuhua Cai, Katherine S. Ziemer, Jian Y. Huang, and Nian X. Sun. Synthesis of ordered arrays of multiferroic $\text{NiFe}_2\text{O}_4\text{-Pb}(\text{Zr}_{0.52}\text{Ti}_{0.48})\text{O}_3$ core-shell nanowires. *Applied Physics Letters*, 90(15):152501–3, —2007—.
- [81] B. J. Rodriguez, X. S. Gao, L. F. Liu, W. Lee, I. I. Naumov, A. M. Bratkovsky, D. Hesse, and M. Alexe. Vortex polarization states in nanoscale ferroelectric arrays. *Nano Letters*, 9(3):1127–1131, —2009—.
- [82] S. Tiedke, T. Schmitz, K. Prume, A. Roelofs, T. Schneller, U. Kall, R. Waser, C. S. Ganpule, V. Nagarajan, A. Stanishevsky, and R. Ramesh. Direct hysteresis measurements of single nanosized ferroelectric capacitors contacted with an atomic force microscope. *Applied Physics Letters*, 79(22):3678–3680, —2001—.
- [83] Z. Wang and M.-F. Hu, J. and Yu. One-dimensional ferroelectric monodomain formation in single crystalline BaTiO_3 nanowire. *Applied Physics Letters*, 89(26):263119–3, —2006—.

- [84] Z. H. Zhou, X. S. Gao, John Wang, K. Fujihara, S. Ramakrishna, and V. Nagarajan. Giant strain in $\text{pbzr}_{0.2}\text{ti}_{0.8}\text{o}_3$ nanowires. *Applied Physics Letters*, 90(5):052902–3, —2007—.
- [85] I. Naumov, L. Bellaiche, and H. Fu. Unusual phase transitions in ferroelectric nanodisks and nanorods. *Nature*, 432(7018):737–740, —2004—.
- [86] A. N. Morozovska, M. D. Glinchuk, and E. A. Eliseev. Phase transitions induced by confinement of ferroic nanoparticles. *Physical Review B*, 76(1):014102, —2007—.
- [87] D. Yadlovker and S. Berger. Uniform orientation and size of ferroelectric domains. *Physical Review B (Condensed Matter and Materials Physics)*, 71(18):184112–6, —2005—.
- [88] N. Sai, A. M. Kolpak, and A. M. Rappe. Ferroelectricity in ultrathin perovskite films. *Physical Review B*, 72(2):020101, —2005—.
- [89] M. Alexe, C. Harnagea, D. Hesse, and U. Gosele. Polarization imprint and size effects in mesoscopic ferroelectric structures. *Applied Physics Letters*, 79(2):242–244, —2001—.
- [90] Z.-G. Ban, S. P. Alpay, and J. V. Mantese. Fundamentals of graded ferroic materials and devices. *Physical Review B*, 67(18):184104, —2003—.
- [91] Z. G. Ban, S. P. Alpay, and J. V. Mantese. Hysteresis offset and dielectric response of compositionally graded ferroelectric materials. *Integrated Ferroelectrics*, 58(1):1281 – 1291, —2003—.
- [92] S. Zhong, Z.-G. Ban, S. P. Alpay, and J. V. Mantese. Large piezoelectric strains from polarization graded ferroelectrics. *Applied Physics Letters*, 89(14):142913–3, —2006—.
- [93] J. Wang, C. S. Sandu, E. Colla, Y. Wang, W. Ma, R. Gysel, H. J. Trodahl, N. Setter, and M. Kuball. Ferroelectric domains and piezoelectricity in monocrystalline $\text{pb}(\text{zr},\text{ti})\text{o}_3$ nanowires. *Applied Physics Letters*, 90(13):133107–3, —2007—.

- [94] A. A. Tsyganenko and V. N. Filimonov. Infrared spectra of surface hydroxyl groups and crystalline structure of oxides. *Journal of Molecular Structure*, 19(2):579–589, —1973—.
- [95] Jie Wang and Marc Kamlah. Domain structures of ferroelectric nanotubes controlled by surface charge compensation. *Applied Physics Letters*, 93(4):042906–3, —2008—.
- [96] S. S. Nonnenmann, O. D. Leaffer, E. M. Gallo, M. T. Coster, and J. E. Spanier. Finite curvature-mediated ferroelectricity. *Nano Letters*, 10(2):542–546, —2010—.
- [97] J. F. Scott. Applications of modern ferroelectrics. *Science*, 315(5814):954–959, —2007—.
- [98] A. N. Morozovska, E. A. Eliseev, and M. D. Glinchuk. Size effects and depolarization field influence on the phase diagrams of cylindrical ferroelectric nanoparticles. *Physica B: Condensed Matter*, 387(1-2):358–366, —2007—.
- [99] M. Stengel, D. Vanderbilt, and N. A. Spaldin. Enhancement of ferroelectricity at metal-oxide interfaces. *Nat Mater*, 8(5):392–397, —2009—.
- [100] N. A. Pertsev, J. Rodriguez Contreras, V. G. Kukhar, B. Hermanns, H. Kohlstedt, and R. Waser. Coercive field of ultrathin $\text{pb}(\text{zr}_{0.52}\text{ti}_{0.48})\text{o}_3$ epitaxial films. *Applied Physics Letters*, 83(16):3356–3358, —2003—.
- [101] A. K. Tagantsev and I. A. Stolichnov. Injection-controlled size effect on switching of ferroelectric thin films. *Applied Physics Letters*, 74(9):1326–1328, —1999—.
- [102] M. J. Haun, E. Furman, S. J. Jang, H. A. McKinstry, and L. E. Cross. Thermodynamic theory of $\text{pb}(\text{tio}_3)$. *Journal of Applied Physics*, 62(8):3331–3338, —1987—.
- [103] D.-J. Kim, J.-P. Maria, A. I. Kingon, and S. K. Streiffer. Evaluation of intrinsic and extrinsic contributions to the piezoelectric properties of $\text{pb}(\text{zr}_{1-x}\text{t}_x)\text{o}_3$ thin films as a function of composition. *Journal of Applied Physics*, 93(9):5568–5575, —2003—.

- [104] S. Hong, H. Shin, J. Woo, and K. No. Effect of cantilever–sample interaction on piezoelectric force microscopy. *Applied Physics Letters*, 80(8):1453–1455, —2002—.
- [105] R. Bouregba, G. Poullain, B. Vilquin, and G. Le Rhun. Asymmetrical leakage currents as a possible origin of the polarization offsets observed in compositionally graded ferroelectric films. *Journal of Applied Physics*, 93(9):5583–5591, —2003—.
- [106] Wenhui Ma and L. Eric Cross. Strain-gradient-induced electric polarization in lead zirconate titanate ceramics. *Applied Physics Letters*, 82(19):3293–3295, —2003—.
- [107] S. Mathews, R. Ramesh, T. Venkatesan, and J. Benedetto. Ferroelectric field effect transistor based on epitaxial perovskite heterostructures. *Science*, 276(5310):238–240, —1997—.
- [108] S. Han, C. Li, Z. Liu, B. Lei, D. Zhang, W. Jin, X. Liu, T. Tang, and C. Zhou. Transition metal oxide core-shell nanowires: Generic synthesis and transport studies. *Nano Lett.*, 4(7):1241–1246, —2004—.
- [109] L. Liao, H. J. Fan, B. Yan, Z. Zhang, L. L. Chen, B. S. Li, G. Z. Xing, Z. X. Shen, T. Wu, X. W. Sun, J. Wang, and T. Yu. Ferroelectric transistors with nanowire channel: Toward nonvolatile memory applications. *ACS Nano*, 3(3):700–706, —2009—.
- [110] Igor Stolichnov, Enrico Colla, Nava Setter, Tomasz Wojciechowski, El żbieta Janik, and Grzegorz Karczewski. Nonvolatile gate effect in a ferroelectric-semiconductor quantum well. *Phys. Rev. Lett.*, 97(24):247601, 2006.
- [111] Sang-Mo Koo, Sergey Khartsev, Carl-Mikael Zetterling, Alex Grishin, and Mikael Ostling. Ferroelectric pb(zr[sub 0.52]ti[sub 0.48])/sic field-effect transistor. *Applied Physics Letters*, 83(19):3975–3977, —2003—.
- [112] ITRS. International technology roadmap for semiconductors: 2008 update, June 2009.
- [113] D. E. Kotecki, J. D. Baniecki, H. Shen, R. B. Laibowitz, K. L. Saenger, J. J. Lian, T. M. Shaw, S. D. Athavale, C. Cabral, Jr., P. R. Duncombe,

- M. Gutsche, G. Kunkel, Y.-J. Park, Y.-Y. Wang, and R. Wise. (ba,sr)tio₃ dielectrics for future stacked- capacitor dram. *IBM Journal of Res. and Develop.*, 43:367, 1999.
- [114] N. Menou, Ch Turquat, V. Madigou, Ch Muller, L. Goux, J. Lisoni, M. Schwitters, and D. J. Wouters. Sidewalls contribution in integrated three-dimensional sr_{0.8}bi_{2.2}ta₂o₉-based ferroelectric capacitors. *Applied Physics Letters*, 87(7):073502–3, —2005—.
- [115] Y. Watanabe and M. Okano. Photoresponse of zener tunneling junctions of pb(ti,zr)o₃/sr₂tio₃ at low temperature. *Journal of Applied Physics*, 94(11):7187–7192, —2003—.
- [116] J. J. Yang, M. D. Pickett, X. Li, A. A. OhlbergDouglas, D. R. Stewart, and R. S. Williams. Memristive switching mechanism for metal//oxide//metal nanodevices. *Nature Nano*, 3(7):429–433, —2008—.
- [117] A. Beck, J. G. Bednorz, Ch Gerber, C. Rossel, and D. Widmer. Reproducible switching effect in thin oxide films for memory applications. *Applied Physics Letters*, 77(1):139–141, —2000—.
- [118] A. Sawa, T. Fujii, M. Kawasaki, and Y. Tokura. Hysteretic current–voltage characteristics and resistance switching at a rectifying ti/pr_{0.7}ca_{0.3}mno₃ interface. *Applied Physics Letters*, 85(18):4073–4075, —2004—.
- [119] J. Rodriguez Contreras, H. Kohlstedt, U. Poppe, R. Waser, C. Buchal, and N. A. Pertsev. Resistive switching in metal–ferroelectric–metal junctions. *Applied Physics Letters*, 83(22):4595–4597, —2003—.
- [120] R. Oligschlaeger, R. Waser, R. Meyer, S. Karthaus, and R. Dittmann. Resistive switching and data reliability of epitaxial (ba,sr)tio₃ thin films. *Applied Physics Letters*, 88(4):042901–3, —2006—.
- [121] H. Kohlstedt, A. Petraru, K. Szot, A. Rudiger, P. Meuffels, H. Haselier, R. Waser, and V. Nagarajan. Method to distinguish ferroelectric from non-ferroelectric origin in case of resistive switching in ferroelectric capacitors. *Applied Physics Letters*, 92(6):062907–3, —2008—.

- [122] K. Szot, W. Speier, G. Bihlmayer, and R. Waser. Switching the electrical resistance of individual dislocations in single-crystalline struo3. *Nat Mater*, 5(4):312–320, —2006—.
- [123] H. Kohlstedt, N. A. Pertsev, J. Rodriguez Contreras, and R. Waser. Theoretical current-voltage characteristics of ferroelectric tunnel junctions. *Physical Review B*, 72(12):125341, —2005—.
- [124] M. Ye Zhuravlev, R. F. Sabirianov, S. S. Jaswal, and E. Y. Tsymbal. Giant electroresistance in ferroelectric tunnel junctions. *Physical Review Letters*, 94(24):246802, —2005—.
- [125] P. W. M. Blom, R. M. Wolf, J. F. M. Cillessen, and M. P. C. M. Krijn. Ferroelectric schottky diode. *Physical Review Letters*, 73(15):2107, —1994—.
- [126] M.-J. Lee, S. Han, S. H. Jeon, B. H. Park, B. S. Kang, S.-E. Ahn, K. H. Kim, C. B. Lee, C. J. Kim, I.-K. Yoo, D. H. Seo, X.-S. Li, J.-B. Park, J.-H. Lee, and Y. Park. Electrical manipulation of nanofilaments in transition-metal oxides for resistance-based memory. *Nano Letters*, 9(4):1476–1481, —2009—.
- [127] R. Waser, R. Dittmann, G. Staikov, and K. Szot. Redox-based resistive switching memories - nanoionic mechanisms, prospects, and challenges. *Advanced Materials*, 21(25-26):2632–2663, —2009—.
- [128] R. Waser and M. Aono. Nanoionics-based resistive switching memories. *Nat Mater*, 6(11):833–840, —2007—.
- [129] S. Lee, G. A. Rossetti, Z.-K. Liu, and C. A. Randall. Intrinsic ferroelectric properties of the nonstoichiometric perovskite oxide $\text{Ba}_{1-x}\text{Ti}_{1-y}\text{O}_{3-x-2y}$. *Journal of Applied Physics*, 105(9):093519–6, —2009—.
- [130] J. M. Cho, J. M. Seo, J. K. Lee, H. Zhang, and R. Lamb. Electronic properties of oxygen vacancies in titania nanotubes. *Physica B: Condensed Matter*, 404(1):127–130, —2009—.
- [131] K. Tsunoda, Y. Fukuzumi, J. R. Jameson, Z. Wang, P. B. Griffin, and Y. Nishi. Bipolar resistive switching in polycrystalline TiO_2 films. *Applied Physics Letters*, 90(11):113501–3, —2007—.

Appendix A

Matlab Coding for Numerical Calculations

A.1 ODE Solver

```
function sol = AlpayODE(solver, a, b, pts, scalefactor)

if nargin < 1 solver = 'bvp4c'; end bvp_solver = fcnchk(solver);

if nargin < 4 a = 20; b = 30; pts = 10; scalefactor = 1e-8; end alpha = -4.887e-7;
beta = 4.764e7; gamma = 9.66e7; D = 1e-19; D = 1;

Q11 = 9.66e-2; Q12 = -4.6e-2;

C33 = 115e9;

%%% following alpay %%alpha = -118 *

%%% following spanman's code % D =1.8e-9; % alpha = 6.66e5*(-1.); % beta =
3.56e9; % gamma = 2.7e11;

solinit = bvpinit(linspace(a, b, pts), @ssnSolInit);

sol = bvp_solver(@ssnODE, @ssnBC, solinit);

xint = linspace(a,b); Sxint = deval(sol, xint);
```

```

figure; plot(xint,Sxint(1,:)); title( ['solved with ' solver ', pts = ' num2str(pts) ',
sf = ' num2str(scalefactor)']);

% exes = linspace(a, b, pts); % figure; % foobar = 1; scalefactor = 1; % for aa=1:pts
% yint(aa,1:2)=ssnSolInit(exes(aa)); % end % % plot(exes, yint); % yint % foo =
ssnSolInit((b - a)/3 + a) * 1/scalefactor; % foo(1)

%% nested functions % function delP = ssnODE(r, P) [sigmac, dersig] = Sig2(r,a,b);
AAA = alpha; delP = [P(2) (1/D)*(AAA*P(1) + beta*(P(1)^3)+gamma*(P(1)^5))-
P(2)/r]; end

function res = ssnBC(ya, yb) res = [ya(2) + 1/D * ya(1) yb(2) + 1/D * yb(1)];
end

function yinit = ssnSolInit(x) % yinit = [-cos( (x-a)/(b - a) * pi) * scalefactor %
sin( (x-a)/(b - a) * pi) * scalefactor]; yinit = [((b - x)/(b - a)) * scalefactor ((b -
x)/(b - a)) * scalefactor]; %% (-1/(b - a)) * scalefactor ]; end

end

%F(R,P,PP)=(-1./R)*PP+(1/1.8e-9)*(6.66e5*(-1.)*P-3.56e9*P**3+2.7e11*P**5)
%F(R,P,PP)=(-1./R)*y2+(1/1.8e-9)*(6.66e5*(-1.)*P-3.56e9*P**3+2.7e11*P**5)

```

A.2 SSNODE Solver

```

function sol = ssnPDE(solver, a, b, pts, scalefactor,lambda)

written by OL, following mat4bvp tutorial July 9, 2008

if nargin < 1 solver = 'bvp4c'; end bvp_solver = fcnchk(solver);

if nargin < 4 a = 20; b = 30; pts = 10; scalefactor = 1e-8; end alpha = -4.887e7;
beta = 4.764e7; gamma = 9.66e7; D = 1e-19; D = 1; alpha = -6.36e7; beta =
1.28e9; gamma = 1.356e8; D = 1e-19; screen = .1 * (b - a);

alpha = -4.887e7*2; beta = 4.764e7*4; gamma = 1.336e8*6; D = sqrt(1e-19);
SSNScreen = 1e9; screen = 1*lambda;

```

```

Q11 = 9.66e-2; Q12 = -4.6e-2;

C33 = 115e9;

D =1.8e-9; alpha = 6.66e5*(-1.); beta = 3.56e9; gamma = 2.7e11;

solinit = bvpinit(linspace(a, b, pts), @ssnSolInit);

sol = bvp solver(@ssnODE, @ssnBC, solinit);

xint = linspace(a,b); Sxint = deval(sol, xint);

figure; plot(xint,Sxint(1,:)); title( ['solved with ' solver ', pts = ' num2str(pts) ',
sf = ' num2str(scalefactor)']);

exes = linspace(a, b, pts); figure; foobar = 1;scalefactor = 1; for aa=1:pts yint(aa,1:2)=ssnSolInit(
end

plot(exes, yint); yint foo = ssnSolInit((b - a)/3 + a) * 1/scalefactor; foo(1)

nested functions

function delP = ssnODE(r, P) [sigmac, dersig] = Sig2(r,a,b); AAA = alpha; delP
= [P(2) (1/D)*(AAA*P(1) + beta*(P(1)3) + gamma * (P(1)5)) - P(2)/r]; end

function res = ssnBC(ya, yb) res = yb(1) + yb(2)*screen];

res = [ya(1) yb(1)]; end

function yinit = ssnSolInit(x) yinit = [scalefactor scalefactor]; [-cos( (x-a)/(b - a)
* pi) * scalefactor sin( (x-a)/(b - a) * pi) * scalefactor]; yinit = [((b - x)/(b - a))
* scalefactor ((b - x)/(b - a)) * scalefactor]; end

end

F(R,P,PP)=(-1./R)*PP+(1/1.8e-9)*(6.66e5*(-1.)*P-3.56e9*P**3+2.7e11*P**5) F(R,P,PP)=(-
1./R)*y2+(1/1.8e-9)*(6.66e5*(-1.)*P-3.56e9*P**3+2.7e11*P**5)

```

A.3 SSN Script

```
t1 = rem(now,1);
```

```
ts=linspace(0,800,500);
```

```
tscrvflat = ts; mns = zeros(length(ts),1); bigssn = zeros(5000,length(ts));
```

```
pts = 5000; init = 1; maxtry = 200; tol = 1e-7; lambda1 = 1e-9; lambda2 =  
.05e-9; mnstol = 1e-5; curved a = 18e-9; b = 25e-9; curved = 1; stressed = 1;
```

```
[bigssn1825crv2,mns1825crv2] = NALGwrapper(a,b,pts,init,maxtry,tol,... lambda1,lambda2,ts,...  
mnstol,curved,stressed);
```

```
a = 29e-9; b = 40e-9; curved = 1; stressed = 1;
```

```
[bigssn2940crv,mns2940crv] = NALGwrapper(a,b,pts,init,maxtry,tol,... lambda1,lambda2,ts,...  
mnstol,curved,stressed);
```

```
a = 40e-9; b = 55e-9; curved = 1; stressed = 1;
```

```
[bigssn4055crv,mns4055crv] = NALGwrapper(a,b,pts,init,maxtry,tol,... lambda1,lambda2,ts,...  
mnstol,curved,stressed);
```

```
a = 90e-9; b = 120e-9; curved = 1; stressed = 1;
```

```
[bigssn90120crv,mns90120crv] = NALGwrapper(a,b,pts,init,maxtry,tol,... lambda1,lambda2,ts,...  
mnstol,curved,stressed);
```

```
flat a = 18e-9; b = 25e-9; curved = 0; stressed = 0;
```

```
[bigssn1825flat,mns1825flat] = NALGwrapper(a,b,pts,init,maxtry,tol,... lambda1,lambda2,ts,...  
mnstol,curved,stressed);
```

```
a = 29e-9; b = 40e-9; curved = 0; stressed = 0;
```

```
[bigssn2940flat,mns2940flat] = NALGwrapper(a,b,pts,init,maxtry,tol,... lambda1,lambda2,ts,...  
mnstol,curved,stressed);
```

```
a = 40e-9; b = 55e-9; curved = 0; stressed = 0;
```

```

[bigssn4055flat,mns4055flat] = NALGwrapper(a,b,pts,init,maxtry,tol,... lambda1,lambda2,ts,...
mnstol,curved,stressed);

a = 90e-9; b = 120e-9; curved = 0; stressed = 0;

[bigssn90120flat,mns90120flat] = NALGwrapper(a,b,pts,init,maxtry,tol,... lambda1,lambda2,ts,...
mnstol,curved,stressed);

t2 = rem(now,1);

fprintf('took

for x = 1:length(ts) if x==1 bigssn(:,x)=NEWALG114(a,b,5000,1,100,1e-7,1e-9,.05e-
9,ts(x)); else bigssn(:,x)=NEWALG114(a,b,5000,bigssn(:,x-1),100,1e-7,1e-9,.05e-9,ts(x));
end mns(x)= dot(r,bigssn(1:5000,x))/sum(r);fprintf('if(abs(mns(x)) > 1e-5) break;
end end tic lambda = 1e-9; betterssn2518lmb1 = ALG114bb(18e-9,25e-9,2000,.5,0,1e-
6,3000,lambda);toc; betterssn4029lmb1 = ALG114bb(29e-9,40e-9,2000,.5,0,1e-6,3000,lambda);
betterssn5540lmb1 = ALG114bb(40e-9,55e-9,2000,.5,0,1e-6,3000,lambda); betterssn12090lmb1
= ALG114bb(90e-9,120e-9,2000,.5,0,1e-6,3000,lambda); toc;tic; lambda = 3e-9;
betterssn2518lmb3 = ALG114bb(18e-9,25e-9,2000,.5,0,1e-6,3000,lambda); betterssn4029lmb3
= ALG114bb(29e-9,40e-9,2000,.5,0,1e-6,3000,lambda); betterssn5540lmb3 = ALG114bb(40e-
9,55e-9,2000,.5,0,1e-6,3000,lambda); betterssn12090lmb3 = ALG114bb(90e-9,120e-
9,2000,.5,0,1e-6,3000,lambda); toc;tic

lambda = 5e-9; betterssn2518lmb5 = ALG114bb(18e-9,25e-9,2000,.5,0,1e-6,3000,lambda);
betterssn4029lmb5 = ALG114bb(29e-9,40e-9,2000,.5,0,1e-6,3000,lambda); betterssn5540lmb5
= ALG114bb(40e-9,55e-9,2000,.5,0,1e-6,3000,lambda); betterssn12090lmb5 = ALG114bb(90e-
9,120e-9,2000,.5,0,1e-6,3000,lambda); toc;tic; lambda = 5e-10; betterssn2518lmb50=
ALG114bb(18e-9,25e-9,2000,.5,0,1e-6,3000,lambda); betterssn4029lmb50 = ALG114bb(29e-
9,40e-9,2000,.5,0,1e-6,3000,lambda); betterssn5540lmb50 = ALG114bb(40e-9,55e-
9,2000,.5,0,1e-6,3000,lambda); betterssn12090lmb50 = ALG114bb(90e-9,120e-9,2000,.5,0,1e-
6,3000,lambda); toc;tic;

betterssn7nmGiant50 = ALG114bb(10 + 18e-9,10 + 25e-9,2000,.5,0,1e-6,3000,lambda);

betterssn7nmGiant1 = ALG114bb(10 + 18e-9,10 + 25e-9,2000,.5,0,1e-6,3000,1e-
9); toc; betterssn2518b = ALG114bb(18e-9,25e-9,3000,.5,0,1e-6,3000); betterssn4029b

```

```
= ALG114bb(29e-9,40e-9,3000,.5,0,1e-6,3000); betterssn5540b = ALG114bb(40e-
9,55e-9,3000,.5,0,1e-6,3000); betterssn12090b = ALG114bb(90e-9,120e-9,3000,.5,0,1e-
6,3000);
```

A.4 LK solver

```
function pm = LKsolve(a, b, N, init,maxIter, TOL,lambda,... lambdaScreen,T,curved,stressed,Eterm)
pl = NEWALG114(a, b, N, init,maxIter, TOL,lambda,... lambdaScreen,T,curved,stressed,Eterm)
mn = NEWALG114(a, b, N, -init,maxIter, TOL,lambda,... lambdaScreen,T,curved,stressed,Eterm)
pm = [pl mn]; end
```

A.5 Simple Solver

```
function W = simpsolve(AA,BB,N,ALPHA,BETA,TOL,NN)
```

```
SSNalpha = -6.36e7; SSNbeta = 1.28e9; SSNgamma = 1.356e8; SSND = 1e-19;
SSNscreen = 1e-9;SSNscreen = SSND; Q12 = -4.6e-2;
```

```
C33 = 115e9;
```

```
H = (BB - AA) / (N + 1); N1 = N-1; W = zeros(N,1); A = zeros(N,1); B =
zeros(N,1); C = zeros(N,1);
```

```
W = 1:N;
```

```
K = 0; while K < NN X = AA; T = -(W(1)-2*H*W(2)/SSNscreen - W(1))/(2*H);
T = -(W(1) * SSNscreen);
```

```
A(1) = 2+H*H*FY(X,W(1),T); B(1) = -1+H*FYP(X,W(1),T)/2; D(1) = -(2*W(1)-
W(2)-ALPHA+H*H*F(X,W(1),T)); D(1) = -(2*W(1)-W(2)-W(2)+H*H*F(X,W(1),T));
STEP 6 for I = 2 : N1 X = AA+I*H; T = (W(I+1)-W(I-1))/(2*H); A(I) =
2+H*H*FY(X,W(I),T); B(I) = -1+H*FYP(X,W(I),T)/2; C(I) = -1-H*FYP(X,W(I),T)/2;
```

```
D(I) = -(2*W(I)-W(I+1)-W(I-1)+H*H*F(X,W(I),T)); D(I) = -(2*W(I)-W(I+1)-
W(I-1)+H*H*F(X,W(I),T));
```

```
end; STEP 7 X = BB - H;
```

```
T = (BETA-W(N-1))/(2*H); T = (W(N-1)-2*H*W(N)/SSND - W(N-1))/(2*H);
T = (W(N-1)-2*H*W(N)/SSNscreen - W(N-1))/(2*H); T = -(W(N) * SSNscreen);
```

```
A(N) = 2+H*H*FY(X,W(N),T); C(N) = -1-H*FYP(X,W(N),T)/2; D(N) = -
(2*W(N)-W(N-1)-BETA+H*H*F(X,W(N),T)); D(N)= -(2*W(N)-W(N-1)-(W(N-
1)-2*H*W(N)/SSND)+H*H*F(X,W(N),T)); this (above) was spanman's version
D(N)= -(2*W(N)-W(N-1)-(W(N-1)-2*H*W(N)/SSNscreen)+H*H*F(X,W(N),T));
Jac = sparse(1:N,1:N,A(1:N),N,N) + sparse(2:N,1:N-1,B(1:N-1),N,N) + sparse(1:N-
1,2:N,C(2:N),N,N); Jinv = inv(Jac); end
```

```
function F1 = F(r,p,pp) F1 = 1/SSND * (SSNA(r) * p + SSNbeta * p3 +
SSNgamma * p5) - pp/r; end
```

```
function F2 = FY(r,p,pp) F2 = 1/SSND*(SSNA(r) + 3 * SSNbeta * p2 + 5 *
SSNgamma * p4); end
```

```
function F3 = FYP(r,p,pp) F3 = -1/r; end
```

```
function Aval = SSNA(r) [sigmac, dersig] = Sig2(r,AA,BB); Aval = SSNalpha
- 2 * Q12 * C33 * sigmac * BETA;Aval = (SSNalpha * 2) - 2 * Q12 * C33 *
sigmac*(AA * (1 + (BB-AA)/AA) * 1e5) ; * BETA;Aval = SSNalpha; end
```

```
end
```

A.6 SigmaC

```
function Rsigmac = Sigmac(are) a = (20:1.4:90); b = (25:1.9:120); rho = are./a; al-
pha = 1.21; beta=-.34; delta=.65; iota=2.83; eta=b/a; omega1 = sqrt((((beta2)+
(alpha * iota))/(1 + iota)); omega2 = -omega1; m1 = [(((beta * (omega1)2) +
(delta * beta * omega1) - (delta * (omega1)2) - (alpha * omega1))/(((omega1)2) -
alpha)); (eta*(omega1 - 1)) * (((beta*(omega1)2) + (delta*beta*omega1) - (delta*
(omega1)2) - (alpha * omega1))/(((omega1)2) - alpha)); 1; (eta*(omega1))]; m2 =
```

```

[(((beta * (omega2)^2) + (delta * beta * omega2) - (delta * (omega2)^2) - (alpha *
omega2))/(((omega2)^2) - alpha)); (eta^(omega2 - 1)) * (((beta * (omega2)^2) + (delta *
beta * omega2) - (delta * (omega2)^2) - (alpha * omega2))/(((omega2)^2) - alpha)); 1; (eta^(omega2))];
[1 - ((delta * beta) / alpha); (eta^( - 1)) * (1 - ((delta * beta) / alpha)); 0; log(eta)]; m4 =
[0; 0; 1; 1]; M = [m1 m2 m3 m4]; b3 = [-1; 0; 1; 0]; M13 = [b3 m2 m3 m4]; M23 =
[m1 b3 m3 m4]; M33 = [m1 m2 b3 m4]; M43 = [m1 m2 m3 b3]; A3 = det(M13) / det(M); B3 =
det(M23) / det(M); C3 = det(M33) / det(M); D3 = det(M43) / det(M); sigmac =
(A3 * ((a * are)^(omega1 - 1)) * (((beta * (omega1)^2) + (delta * beta * omega1) -
(delta * (omega1)^2) - (alpha * omega1)) / (((omega1)^2) - alpha)) * (1./a)) + (B3 *
((a * are)^(omega2 - 1)) * (((beta * (omega2)^2) + (delta * beta * omega2) - (delta *
(omega2)^2) - (alpha * omega2)) / (((omega2)^2) - alpha)) * (1./a)) + (C3 * ((a *
are)^( - 1)) * (1 - ((delta * beta) / alpha)) * (1./a))); plot(rho, sigmac); [A, ARE] =
meshgrid(a, are); [A, B] = meshgrid(a, b); SIGMAC = (A3 * ((A * ARE)^(omega1 -
1)) * (((beta * (omega1)^2) + (delta * beta * omega1) - (delta * (omega1)^2) - (alpha *
omega1)) / (((omega1)^2) - alpha)) * (1./A)) + (B3 * ((A * ARE)^(omega2 - 1)) *
(((beta * (omega2)^2) + (delta * beta * omega2) - (delta * (omega2)^2) - (alpha *
omega2)) / (((omega2)^2) - alpha)) * (1./A)) + (C3 * ((A * ARE)^( - 1)) * (1 -
((delta * beta) / alpha)) * (1./A))); x = 50; y = 50; for x = 1 : 50, for y = 1 :
50, dersigmac(x, y) = (SIGMAC(x, y) - SIGMAC(x + 1, y + 1)) / (RHO(x, y) -
RHO(x + 1, y + 1)); end, end; B(51, :) = []; A(51, :) = []; A(:, 51) = []; B(:, 51) =
[]; mesh(B, A, dersigmac)

```

A.7 Solve for V

```

function W = SolveForV(P,R,lambda,init,maxIter,TOL) tic;
if(length(P) == length(R)) fprintf('Oh noes!'); W = -1; return; end
N = length(P); W = linspace(0,1,N)';
N1 = N - 1;
A = zeros(N,1); B = zeros(N,1); C = zeros(N,1); FF = zeros(N,1);

```

```

PP = zeros(N,1); PPP = zeros(N,1); for I = 2:N1 PP(I) = (P(I+1) - P(I-1))/(R(I+1)
- R(I-1)); PPP(I) = (P(I+1) - 2*P(I) + P(I-1))/((R(I+1) - R(I-1))/2)^2; end

PP(1) = P(2) - (R(2)-R(1))* (PP(3)-PP(2))/(R(3)-R(2)); PPP(1) = P(2) - (R(2)-
R(1))* (PPP(3)-PPP(2))/(R(3)-R(2));

PP(N) = P(N1) + (R(N)-R(N1))* (PP(N1)-PP(N1-1))/(R(N1)-R(N1-1)); PPP(N)
= P(N) + (R(N)-R(N1))* (PPP(N1)-PPP(N1-1))/(R(N1)-R(N1-1));

K = 1; while (K <= maxIter)

H = R(2) - R(1); % A(1) = -1;% C(1) = 1;% FF(1) = -(W(2) - W(1));% % A(1)
= 1 + lambda/H; % C(1) = -lambda/H; % FF(1) = -(W(1) - lambda * (W(2) -
W(1))/H); %

A(1) = 1 - R(1)/H; C(1) = +R(1)/H; FF(1) = -(W(1) + R(1) * (W(2) - W(1))/H);
% A(1) = -1000000;% C(1) = 0;% FF(1) = -(W(2) - W(1));

% % A(1) = 1 - lambda/H; % C(1) = +lambda/H; % FF(1) = -(W(1) + lambda
* (W(2) - W(1))/H);

for I = 2:N1 H = (R(I+1)-R(I-1))/2;

X = R(I);

A(I) = 2 ;fyp = Fvp(X);B(I) = -1 + .5 * H * fyp; C(I) = -1 - .5 * H * fyp;

FF(I) = -(-(W(I-1) - 2*W(I) + W(I+1)))... + H*H*Vrr(X,(W(I+1)-W(I-1))/(2*H),P(I),PP(I));

end

H = R(N) - R(N1); % A(N) = 1;% B(N) = -1;% FF(N) = -(W(N) - W(N-1));

% A(N) = 1 + lambda/H; % B(N) = -lambda/H; % FF(N) = -(W(N) + lambda
* (W(N) - W(N-1))/H); A(N) = 1 + R(N)/H; B(N) = -R(N)/H; FF(N) = -(W(N)
+ R(N) * (W(N) - W(N-1))/H);

J = sparse(1:N,1:N,A(1:N),N,N) + sparse(1:N-1,2:N,C(1:N-1),N,N) + sparse(2:N,1:N-
1,B(2:N),N,N);

v = J;

```

```
W = W + v;
```

```
fprintf('K=if(max(abs(v)) > TOL)fprintf('completed after if max(abs(v)) > TOL
fprintf('Exited on "condition 2"'); end toc; return; end
```

```
K = K + 1; end
```

```
fprintf('algorithm failed to converge'); toc;
```

```
function vrr = Vrr(r, Vp, p, Pp) vrr = -(p/r + Pp + Vp/r); end
```

```
function fr = Fr(r, Vp, p, Pp, Ppp) fr = -(-p/r2 + Ppp - Vp/r + -(p/r + Pp +
Vp/r)); end
```

```
function fv = Fv() fv = 0; end
```

```
function fvp = Fvp(r) fvp = -1/r; end end
```

A.8 cylinder stress

```
function s = CylStress(r,a,b,mu) b = -b; pb = +mu / b; pa = -mu / a; pave =
(p1 + p2)/2; ab = a/b; ab2 = ab2; ar = a/r; ar2 = ar2; br = b/r; br2 = br2;
```

```
left = pb*(1-ar2); right = ab2*(1-br2)*pa; s = (1 / (1 - ab2)) * (left + right); s
= (-1 / (1 - (a/b)2)) * (pb * (1 - (a/r)2) + (a/b)2 * (1 - (b/r)2) * pa); end
```

A.9 Temperature profile P

```
function [ps,ms,mnsp,mnsm,rv] = ThermalPofE(a,b,N,ef,T)
```

```
% T = 300; % N = 1000; % a = 90e-9; % b = 120e-9;
```

```
ps = zeros(1000,N); ms = zeros(1000,N); mnsp = zeros(N,1); mnsm = zeros(N,1);
```

```
rv = linspace(a,b,1000);
```

```
%ef = 1e14; t1 = rem(now,1);
```



```

ees = zeros(N,1); for x = 1:N ees(x) = -(x-1)*ef;end

last = -ones(1000,1);

for x = 1:N ms(:,x) = NEWALG114(a,b, 1000,last,500,1e-9,1e-9,.05e-9,T,0,0,ees(x));

last = ms(:,x); fprintf('end

last = ones(1000,1); for x = 1:N

ps(:,x) = NEWALG114(a,b,1000,last,500,1e-9,1e-9,.05e-9,T,0,0,ees(x));

last = ps(:,x);

fprintf('end

t2 = rem(now,1);

sm = sum(rv); for x = 1:N mnsp(x) = dot(ps(:,x),rv)/sm; mnsms(x) = dot(ms(:,x),rv)/sm;
end

fprintf('took:

% % eesbig90a = ees; % msbig90a = ms; % psbig90a = ps; % r90a = rv; %
mnsp90a = mnsp; % mnsms90a = mnsms; end

```

A.10 plots

```

% [ps18b,ms18b,mnsp18b,mnsms18b,rv18b] = ThermalPofE(18e-9,25e-9,1000,1e14,300);
% [ps29b,ms29b,mnsp29b,mnsms29b,rv29b] = ThermalPofE(29e-9,40e-9,1000,1e14,300);
% [ps40b,ms40b,mnsp40b,mnsms40b,rv40b] = ThermalPofE(40e-9,55e-9,1000,1e14,300);
% [ps90b,ms90b,mnsp90b,mnsms90b,rv90b] = ThermalPofE(90e-9,120e-9,1000,1e14,300);
[psbiga,msbiga,mnspbiga,mnsmsbiga,rvbiga] = ThermalPofE(119,120,1000,1e14,300);
% %plots % % figure; % plot(r185 - 18e - 9, p18, r295 - 29e - 9, p29, r405 - 40e -
9, p40, r905 - 90e - 9, p90)%%figure;%plot(tsng2, abs(mns1825ng2), tsng2, abs(mns2940ng2), ts
% T = 300; % p18 = NEWALG114(18e-9,25e-9, 5000,1,200,1e-9,1e-9,.05e-9,T,1,1);
% p29 = NEWALG114(29e-9,40e-9, 5000,1,200,1e-9,1e-9,.05e-9,T,1,1); % p40 =

```

```

NEWALG114(40e-9,55e-9, 5000,1,200,1e-9,1e-9,.05e-9,T,1,1); % p90 = NEWALG114(90e-
9,120e-9,5000,1,200,1e-9,1e-9,.05e-9,T,1,1); % % % r18=linspace(18,25,5000)*1e-9;
% r29=linspace(29,40,5000)*1e-9; % r40=linspace(40,55,5000)*1e-9; % r90=linspace(90,120,5000
9); % % v18 = SolveForV(p18,r18,0e0,1e10,1000,1e-12); % v29 = SolveForV(p29,r29,0e0,1e10,1000
12); % v40 = SolveForV(p40,r40,0e0,1e10,1000,1e-12); % v90 = SolveForV(p90,r90,0e0,1e10,1000
12);

```

```

% v18big = zeros(5000, length(tscrvflat)/10); % % for x=1:length(tscrvflat)/10 %
v18big(:,x)=SolveForV(bigssn1825crv(1:5000,x*10),r18,0,1e-5,1000,1e-12); % end
% % v29big = zeros(5000, length(tscrvflat)/10); % % for x=1:length(tscrvflat)/10
% v29big(:,x)=SolveForV(bigssn2940crv(1:5000,x*10),r18,0,1e-5,1000,1e-12); % end
% % v40big = zeros(5000, length(tscrvflat)/10); % % for x=1:length(tscrvflat)/10
% v40big(:,x)=SolveForV(bigssn4055crv(1:5000,x*10),r18,0,1e-5,1000,1e-12); % end
% % v90big = zeros(5000, length(tscrvflat)/10); % % for x=1:length(tscrvflat)/10
% v90big(:,x)=SolveForV(bigssn90120crv(1:5000,x*10),r18,0,1e-5,1000,1e-12); %
end

```

```

% T=712; % Tc = 714; % dt = T - Tc; % % at0 = -4.887e7*2/-366; % beta
= 4.764e7*4; % gamma = 1.336e8*6; % alpha = dt*at0; % % N = 3001; % rts
= zeros(5,N); % Eps = zeros(N,1); % % for x = 1:N % E = (x-(N-1)/2)*5e1; %
dp = (2*.05/(7*8.854e-12)); % Ep = E; % rt = roots([gamma 0 beta 0 (alpha)
-Ep]); % rts(:,x) = rt; % Eps(x) = Ep; % end % % maxr = zeros(N,1); % minr
= zeros(N,1); % for x = 1:N % maxr(x) = -inf; % minr(x) = +inf; % for y =
1:5 % if(isreal(rts(y,x))) % if(rts(y,x) > maxr(x)) % maxr(x) = rts(y,x); % end %
if(rts(y,x) < minr(x)) % minr(x) = rts(y,x); % end % end % end % end %

```

```

% % ind = 0; % exes = linspace(-1,1,5001)*.5; % vals = zeros(length(exes),1);
% for x=exes % ind = ind + 1; % pp = x; % pv = [pp5pp4pp3pp2pp1pp0]; %cv =
[gamma0beta0alpha-E*0]; %vals(ind) = dot(cv,pv); % %end% % %T = 300; %N =
1000; %a = 90e-9; %b = 120e-9; % %ps = zeros(1000, N); %ms = zeros(1000, N); %mnsp =
zeros(N, 1); %mnsm = zeros(N, 1); % %rv = linspace(a, b, 1000); % %ef = 1e14; %t1 =
rem(now, 1); % %ees = zeros(N, 1); %for x = 1 : N %ees(x) = -(x - 1) *
ef; %end% % %last = ones(1000, 1); %for x = 1 : N %ps(:, x) = NEWALG114(a, b, 1000, last,
9, 1e-9, .05e-9, T, 1, 1, ees(x)); % %last = ps(:, x); % %fprintf('%end% % %last =
-ones(1000, 1); % %for x = 1 : N %ms(:, x) = NEWALG114(a, b, 1000, last, 500, 1e-

```

```

9, 1e-9, .05e-9, T, 1, 1, ees(x)); %%last = ms(:, x); %fprintf('%end%t2 = rem(now, 1); %%sm
sum(rv); %for x = 1 : N %mns(x) = dot(ps(:, x), rv)/sm; %mns(x) = dot(ms(:,
, x), rv)/sm; %end%%fprintf('took : %%%eeesbig90a = ees; %msbig90a =
ms; %psbig90a = ps; %r90a = rv; %mns90a = mns; %mns90a = mns;

```

A.11 P oft

```

function [pmat, Eoft, tlist, mnslist] = Poft(p0, AVALS, beta, gamma, D, E0, dt,
omega, GAMMA, H, maxsteps, a, b) % [dpdt, left, right] = Poft(p0, AVALS, beta,
gamma, D, E0, dt, omega, GAMMA, H) tic;

```

```

N = length(p0); N1 = N-1;

```

```

dpdt = zeros(N, 1); pmat = zeros(N, maxsteps); tlist = ((1:maxsteps)-1)*dt; Eoft
= zeros(maxsteps, 1); mnslist = zeros(maxsteps, 1); % left = zeros(N, 1); % right =
zeros(N, 1); %t = 0; p = p0;

```

```

%% Find ad-hoc coeffs k1, kN

```

```

k1 = abs( (AVALS(1)*p(1) + beta*p(1)^3 + gamma * p(1)^5)/((p(2) - p(1))/(H *
H)*D)); kN = abs((AVALS(N)*p(N) + beta*p(N)^3 + gamma*p(N)^5)/((p(N) -
p(N1))/(H * H) * D));

```

```

for ts = 1:maxsteps t = tlist(ts); Eterm = - E0*sin(omega*t); Eoft(ts) = Eterm;
k1=1; s1 = 2*pi*p(1)*a/1e-9; dpdt(1) = AVALS(1)*p(1) + beta*p(1)^3 + gamma *
p(1)^5 + (p(2) - p(1))/(H * H) * D * k1 - Eterm;

```

```

% left(1) = AVALS(1)*p(1) + beta*p(1)^3 + gamma * p(1)^5; %right(1) = +(p(2) -
p(1))/(H * H) * D;

```

```

for n=2:N1 % left(n) = AVALS(n)*p(n) + beta*p(n)^3 + gamma*p(n)^5; %right(n) =
-(p(n+1) - 2 * p(n) + p(n-1))/(H * H) * D; dpdt(n) = AVALS(n) * p(n) +
beta * p(n)^3 + gamma * p(n)^5 - (p(n+1) - 2 * p(n) + p(n-1))/(H * H) * D -
Eterm; enddpdt(N) = AVALS(N) * p(N) + beta * p(N)^3 + gamma * p(N)^5 +
(p(N) - p(N1))/(H * H) * D * kN - Eterm; %left(N) = AVALS(N) * p(N) +
beta * p(N)^3 + gamma * p(N)^5; %right(N) = +(p(N) - p(N1))/(H * H) * D; %

```

```

p = p + dpdt*dt/GAMMA; pmat(:,ts) = p; if(any(isnan(p))) fprintf('nans away!
break; end mnslist(ts) = mean(p); end toc; end % tic; % tmax = 1/(omega/(2*pi));
% % N = ceil(tmax/dt); % % len = 1000; % pt = zeros(len,1); % ts = ze-
ros(len,1);% % p = p0; % k = 0; % period = ceil(N/len); % for n=1:N % dpdt = al-
pha*p + beta*p^3+gamma*p^5+depol+E0*sin(omega*dt*n);%if(isnan(dpdt))%fprintf('ohnoe
p + dt * dpdt/GAMMA;%%%if(mod(n,period) == 0)%k = k + 1;%if(k >
len)%break;%end%pt(k) = p;%ts(k) = n*dt;%ifmod(k,10) == 0%fprintf('%end%end%%en

```

A.12 P int

```

function s = Pollnt(P,r) s = 0;

if length(P) != length(r) fprintf('size mismatch'); return; end

N = length(P);

dr = r(2) - r(1);

for n = 2:N-1 left = (P(n+1) - P(n-1))/(2*dr) * r(n); right = (P(n) + P(n+1))/2;

s = s + (left + right)*dr; end

end

```

Vita

A.13 Publications and Patents

1. **S.S. Nonnenmann**, E.M. Gallo, and J.E. Spanier, "Oxygen Vacancy-Based Resistive Switching in Ferroelectric Perovskite Nanotubes" *submitted* (2010).
2. **S.S. Nonnenmann**, O.D. Leaffer, E.M. Gallo, M.T. Coster, and J.E. Spanier, "Finite Curvature-Mediated Ferroelectricity", *Nano Lett.*, **10** 542 (2010).
3. **S.S. Nonnenmann**, E.M. Gallo, G.R. Soja, M.T. Coster, R.S. Joseph, and J.E. Spanier, "Piezoresponse Across a Ferroelectric Nanotube Wall", *Appl. Phys. Lett.* **95** 232903 (2009)[Also selected for the Virtual Journal of Nanoscale Science and Technology, 20 (25)].
4. **S.S. Nonnenmann** and J.E. Spanier, "Ferroelectricity in chemical nanostructures: proximal probe characterization and the surface chemical environment", *J. Mater. Sci.* 44, 5205 (2009)
5. B. Garipcan, J. Winters, J. S. Atchison, M. Cathell, J. Schiffman, O. D. Leaf-fer, **S. S. Nonnenmann**, C. Schauer, E. Piskin, B. Nabet, and J. E. Spanier, "Controllable Formation of Nano-scale Patterns on TiO₂ by Conductive-AFM Nanolithography", *Langmuir* 24(16) 8944 (2008).
6. L. Cao, B. Garipcan, E.M. Gallo, **S.S. Nonnenmann**, E. Piskin, B. Nabet and J.E. Spanier, "Excitation of Local Field Enhancement on Silicon Nanowires", *Nano. Lett.* 8(2) 601 (2008).
7. "Ferroelectric Nanoshell Devices", J.E. Spanier, **S.S. Nonnenmann** and O.D. Leaffer, U.S. Provisional Patent 61/119306
8. "Integrated Semiconductor/Transition Metal Oxide Nanostructures and Methods for Preparing Same", J.E. Spanier, **S.S. Nonnenmann** and R.S. Joseph, U.S. Provisional Patent 60/820886